D-33192
Version 4.0

Earth Observing System (EOS)
Tropospheric Emission Spectrometer (TES)

Data Validation Report
(Version F05_05, F05_06, F05_07 data)

Editors:

Robert Herman and Gregory Osterman

Contributors:

Christopher Boxe, Kevin Bowman, Karen Cady-Pereira, Tony Clough, Annmarie Eldering, Brendan Fisher, Dejian Fu, Robert Herman, Daniel Jacob, Line Jourdain, Susan Kulawik, Michael Lampel, Qinbin Li, Jennifer Logan, Ming Luo, Inna Megretskaia, Ray Nassar, Gregory Osterman, Susan Paradise, Vivienne Payne, Hank Revercomb, Nigel Richards, Mark Shephard, Dave Tobin, Solene Turquety, Felicia Vilnrotter, Helen Worden, John Worden, Lin Zhang

November 23, 2011

JPL
Jet Propulsion Laboratory
California Institute of Technology
Pasadena, California

© 2011. All rights reserved.

Earth Observing System (EOS)
Tropospheric Emission Spectrometer (TES)

Data Validation Report
(Version F05_05, F05_06, F05_07 data)

Approved by:

John Worden
TES Principal Investigator
Jet Propulsion Laboratory

Douglas Shepard
TES Ground Data Systems Manager
Jet Propulsion Laboratory

Revision History:

Version	Date	Description/Comments
1.0	8/15/2005	Initial Version of Validation Report for time frame "launch + 1 year"
2.0	1/4/2007	Validation Report for F03_03 data
3.0	11/5/2007	Validation Report for F04_04 data
4.0	11/23/2011	Validation Report for F05_05, F05_06, F05_07 data

TABLE OF CONTENTS

1. OVERVIEW OR TES PRODUCT VALIDATION 1

1.1 APPLICABLE DOCUMENTS 2

2. AN OVERVIEW OF THE TES INSTRUMENT AND DATA PRODUCTS 4

2.1 INSTRUMENT DESCRIPTION 4
2.2 TES OBSERVATION MODES 4
2.2.1 Global Surveys 4
2.2.2 Special Observations 6
2.3 TES SCAN IDENTIFICATION NOMENCLATURE 7
2.4 WHERE TO OBTAIN TES DATA 7
2.5 FILE FORMATS AND DATA VERSIONS 8
2.6 TES STANDARD L2 PRODUCTS 10
2.7 REFERENCES 11
2.7.1 TES References 11

3. EXECUTIVE SUMMARY 13

3.1 REFERENCES 17
3.1.1 TES References 17
3.1.2 General References 17

4. L1B RADIANCE 18

4.1 REFERENCES 18
4.1.1 TES L1B Radiance Validation Reference 18
4.1.2 TES References 18
4.1.3 General References 18

5. VALIDATION OF TES V004 NADIR OZONE PROFILES USING OZONESONDE MEASUREMENTS 20

5.1 OVERVIEW 20
5.2 TES OZONESONDE COMPARISONS 21
5.3 REFERENCES 34
5.3.1 Primary TES Nadir Ozone References 34
5.3.2 TES References 35
5.3.3 General References 36

6. VALIDATION OF TES RETRIEVALS OF CARBON MONOXIDE 39

6.1 OVERVIEW 39
6.2 INSTRUMENT PERFORMANCE BEFORE AND AFTER OPTICAL BENCH WARM-UP 39
6.3 GLOBAL DISTRIBUTIONS OF CO FROM TES MEASUREMENTS 40
6.4 CO VALIDATION: COMPARISONS TO IN SITU AIRCRAFT MEASUREMENT 41
6.5 CO VALIDATION: COMPARISONS TO MOZAIC, ACE, MLS, AND AIRS DATA SETS 45
6.6 CO VALIDATION: COMPARISONS TO MOPITT DATA 45
6.7 CO VALIDATION: SUMMARY 47
6.8 REFERENCES 47
6.8.1 TES Carbon Monoxide References 47

6.8.2 TES References *48*

7. VALIDATION OF TES NADIR TEMPERATURE RETRIEVALS WITH RADIOSONDES 49

7.1 EXECUTIVE SUMMARY 49
7.2 IMPROVEMENTS IN TES TEMPERATURE RETRIEVAL IN V004 49
7.3 A PRIORI CONSTRAINT VECTOR 50
7.4 CURRENT VALIDATION STATUS OF V004 NADIR TEMPERATURE 50
7.4.1 NCEP sonde database compared with TES V004 TATM *51*
7.4.2 NOAA ESRL sonde database compared with TES V004 TATM *54*
7.5 COMPARISON OF V004 VALIDATION WITH V003/V002 RETRIEVALS 55
7.6 SUMMARY 56
7.7 REFERENCES 56
7.7.1 TES Temperature References *56*
7.7.2 TES References *56*
7.7.3 General References *57*

8. SEA SURFACE TEMPERATURE 59

8.1 REFERENCES 59
8.1.1 TES References *59*
8.1.2 General References *59*

9. WATER VAPOR 61

9.1 PREVIOUS VERSIONS OF TES WATER VAPOR 62
9.2 A PRIORI CONSTRAINT VECTOR 62
9.3 COMPARISON OF TES WATER VAPOR WITH RADIOSONDES 63
9.4 EXECUTIVE SUMMARY 71
9.5 REFERENCES 71
9.5.1 TES References *71*
9.5.2 General References *72*

10. HDO/H_2O 75

10.1 EXECUTIVE SUMMARY FOR HDO/H_2O RATIO VALIDATION 75
10.2 IN SITU DATA SETS 75
10.3 DIRECT COMPARISON OF TES SATELLITE PROFILE DATA TO IN SITU DATA 76
10.4 INDIRECT COMPARISON OF TES DATA TO IN SITU DATA 80
10.5 COMPARISON BETWEEN V004 AND V003 82
10.6 REFERENCES 83
10.6.1 TES HDO/H_2O References *83*
10.6.2 TES References *83*
10.6.3 General References *83*

11. METHANE 84

11.1 OVERVIEW OF CURRENT VALIDATION STATUS OF TES V004 METHANE 84
11.2 TES/DACOM COMPARISONS 84
11.3 TES/AIRS COMPARISONS 85
11.4 TES/GEOS-CHEM COMPARISONS 86

11.5 TES/FTIR COMPARISONS 88
11.6 COMPARISON OF V004 WITH V003 RETRIEVALS 88
11.7 COMMENTS OR LIMITS ON UTILITY OF THE DATA 88
11.8 EXECUTIVE SUMMARY 88
11.9 REFERENCES 89
11.9.1 TES Methane References 89
11.9.2 TES References 89
11.9.3 General References 89

12. CLOUD PRODUCTS 91

12.1 BACKGROUND 91
12.2 CHANGES FROM TES V003 TO V004 91
12.3 CLOUD TOP PRESSURE 93
12.4 CLOUD EFFECTIVE OPTICAL DEPTH 95

APPENDICES 97

A. ACRONYMS 97

LIST OF FIGURES

Figure 5-1 TES-sonde absolute differences for 44 comparisons using TES V001 (cases passing the more selective criteria) with ozone (Worden et al., 2007). 22

Figure 5-2 TES-sonde percent differences and absolute differences in six latitude zones. Individual profiles are shown in gray, mean and one standard deviation ranges are overlaid in dark blue and broken light-blue, respectively. Mean minus one standard deviation and mean plus one standard deviation ranges are overlaid in black. The number of coincident comparisons is "n." This Figure illustrates comparisons using TES V004. (A: Arctic, B: Northern Midlatitudes, C: Northern Subtropics, D: Tropics, E: Southern low- and midlatitudes, and F: Antarctic) 26

Figure 5-3 TES-sonde ozone percent differences and absolute differences in six latitude zones. Individual profiles are shown in gray, and the mean and 1 standard deviation range are overlaid in black. *N* is the number of profiles plotted after removing cloudy scenes and flagged TES data. This study illustrates comparisons using TES V002 27

Figure 5-4 The TES-stare sequence on April 14th, 2008 over Barrow, Alaska, started at 21:45 (UTC), and the ozonesonde on that day at Barrow was launched at 22:13 (UTC), using V003 (a) and V004 (b) TES data. 28

Figure 5-5 The TES-stare sequence on July 5th, 2008 over Egbert, Ontario, started at 17:58 (UTC), and the ozonesonde on that day at Egbert was launched at 18:25 (UTC), using V003 (a) and V004 (b) TES data. 29

Figure 5-6 The TES-stare sequence on January 19th, 2009 over Natal, Brazil, started at 16:08 (UTC), and the ozonesonde on that day at Egbert was launched at 15:50 (UTC), using and V004 TES data. 30

Figure 5-7 The TES-stare sequence on August 29th, 2009 over Moody Tower, Houston, Texas, started at 19:47 (UTC), and the ozonesonde on that day at Egbert was launched at 18:57 (UTC), using and V004 TES data. 31

Figure 5-8 TES-sonde ozone percent differences and absolute differences (for TES V002) for the four seasons (months abbreviated in parentheses) in the northern midlatitudes (35 to 56° N). Individual profiles are shown in gray, and the mean and 1 standard deviation range are overlaid in black. *N* is the number of profiles plotted after removing cloudy scenes and flagged TES data. (Nassar et al. 2008). 32

Figure 5-9 TES-sonde ozone percent differences and absolute differences (for TES V004) for the four seasons (months abbreviated in parentheses) in the northern midlatitudes (35 to 56° N). Individual profiles are shown in gray, mean and one standard deviation ranges are overlaid in dark blue and broken light-blue, respectively. Mean minus one standard deviation and mean plus one standard deviation ranges are overlaid in black. The number of coincident comparisons is "n." This Figure illustrates comparisons using TES V004. 34

Figure 6-1 Time series of measured normalized Integrated Spectral Magnitude (ISM) (top panel), beamsplitter temperature (middle panel), and average DOFS for 30°N-30°S latitude. The ISM is normalized to 1.0 at the beginning of the time series. 40

Figure 6-2 TES CO Global Distributions at 681.3 hPa for the Four Typical Months, Jan, April, July, and Oct 2007. 41

Figure 6-3 Averaged Argus and TES CO and difference profiles for Oct-AVE (upper three panels) and CR-AVE campaign (lower two panels). The Red line is the Argus data adjusted by the TES averaging kernel. For Oct-AVE case, the areas of the TES averaging kernels are shown with all selected cases having this value greater than 0.4. 43

Figure 6-4 Summary plots for TES and DACOM CO profile comparisons during INTEX-B near Houston, March 2006 (left panel pairs), near Hawaii, Apr-May 2006 (middle panel pairs), and near Anchorage, May 2006 (right panel pairs). All the colored symbols and lines are defined the same as in Figure 6-5. 45

Figure 6-5 Comparisons of total CO column reported by TES and MOPITT. The first two panels are the 'direct' comparisons. The last two panels are the comparisons after the TES CO being adjusted to MOPITT a priori profile and MOPITT CO profiles being adjusted by applying TES averaging kernels (M. Luo et al., 2007a). 46

Figure 7-1 Temperatures from RS-80, RS-90 and RS-92 sondes in the NCEP database compared with TES V004, binned by latitude. In each panel, n individual temperature differences are shown (thin grey lines), with bias (solid red line) and rms (dashed red line). The TES operator has been applied to the sonde profiles, and differences are calculated as TES – sonde. Typically a TES cold bias is seen in the upper troposphere (especially at 30-60 N). Much of the rms is due to temporal fluctuations in temperature and uncertainty in the actual release time of the sondes. Figure prepared by K. Cady-Pereira from output of the sonde comparison tool. 52

Figure 7-2 TES-NCEP comparisons, similar to Figure 7-1, for maximum distances < 300 km (left) and < 200 km (right). There is a slight improvement in both bias and rms for the closer coincidence due to spatial variability of tropospheric temperature. 53

Figure 7-3 TES-NCEP comparison, similar to Figure 7-1, for two surface types: land (left) and ocean (right). The lower tropospheric rms is improved over ocean because the surface emissivity is better constrained. 53

Figure 7-4 Temperature profiles from all radiosondes in the NOAA ESRL database compared with TES V004 for 2004-2008, including individual temperature differences (thin grey lines), bias (solid red line), rms difference (dashed red line), and the TES observation error (solid blue line). The TES operator has been applied to the radiosonde profiles, and the differences are calculated as TES minus radiosonde (with averaging kernel). It is seen that the bias is typically less than 0.7 K. The rms is 1 K in the stratosphere and upper troposphere, increasing to 1.5 to 2 K in the lower troposphere. Little difference is seen between cloudy (left) and clear sky scenes (right), except that the near-surface bias is smaller for cloudy scenes (due to low information content, the temperature is closer to the a priori in this case)..... 54

Figure 7-5 Temperature differences between TES and NOAA ESRL radiosondes, similar to Figure 7-4, for two surface types: land (left) and water (right). Bias (solid red line) is less than 0.7 K with subtle differences in the lower troposphere. The rms (dashed red line) is generally less than 1.5 K. 55

Figure 9-1 Diagonal of the TES nadir averaging kernel for water vapor, runid 4803, Transect special observation at Beltsville, MD, 12 Aug 2006. Sensitivity to water vapor decreases at high altitude, typically at pressures less than 200 hPa. Figure generated by M. Luo..... 61

Figure 9-2 Water vapor percent differences between TES V004 and radiosondes in the NOAA ESRL database within 100 km and -0.5 to +1.5 hours. In each panel, n individual matches are shown (thin grey lines) with rms (dashed red lines) and bias (solid red lines). The TES operator has been applied to the radiosonde profiles, and differences are calculated as (TES-radiosonde)/TES. Figure prepared using software from K. Cady-Pereira from output of the TES sonde comparison tool. 64

Figure 9-3 Water vapor percent differences between TES V004 and GMAO GEOS-5 analyses interpolated to the location of the TES retrievals. Similar legend as in Figure 9-2..... 64

Figure 9-4 Water vapor percent differences between GMAO GEOS-5 analyses and NOAA ESRL radiosonde profiles within 100 km and -0.5 to +1.5 hours. The rms differences are dominated by spatial variability of water vapor on the scale of tens of km. Similar legend as in Figure 9-2..... 65

Figure 9-5 Water vapor percent differences between TES V004 and radiosondes in the NOAA ESRL database within 100 km and -0.5 to +1.5 hours. Left: Oceanic comparisons during local daytime shows a bias between TES and radiosondes. Right: Oceanic comparisons during local nighttime have significantly smaller bias. Similar legend to Figure 9-2..... 66

Figure 9-6 Water vapor percent differences between GMAO GEOS-5 and radiosondes in the NOAA ESRL database. Left: Oceanic comparisons during local daytime have a smaller bias than Figure 9-5. Right: Oceanic comparisons during local nighttime..... 67

Figure 9-7 Water vapor percent differences between TES V004 and radiosondes in the NOAA ESRL database within 100 km and -0.5 to +1.5 hours. Left: Land comparisons during local daytime shows a bias between TES and radiosondes. Right: Land comparisons during local nighttime have significantly smaller bias. Similar legend to Figure 9-2. 67

Figure 9-8 Nighttime water vapor percent differences between TES V004 and radiosondes in the NOAA ESRL database by latitude zone. 69

Figure 9-9 Nighttime water vapor percent differences between GMAO GEOS-5 and radiosondes in the NOAA ESRL database by latitude zone. 70

Figure 10-1 Comparison of Flask (red x with vertical lines), JPL ALIAS instrument (black diamonds), and Picarro (purple line). 76

Figure 10-2 Left Panel TES and rawinsonde H_2O. The diamonds are the first 5 pressure levels in the TES H_2O profile used to construct the delta-D profile. Right Panel: The TES delta-D profile (corrected for bias), the a priori constraint and the constructed "true" delta-D profile. The error bars are due to measurement and interfering geophysical parameters. 78

Figure 10-3 In Situ H_2O and Delta-D valus for Nov 5 2008. The dotted lines in the top panel correspond to the diamonds overlapping the TES H_2O profile in Figure 10-2 (left panel). The dotted lines in the bottom panel are the chosen delta-D values used to construct the "true" delta-D profile in the lower troposphere. 79

Figure 10-4 Rows of the individual averaging kernel matrices for H_2O (left panel) and HDO (right panel) 80

Figure 10-5 Comparison of In Situ data from the Picarro instrument during October 2008 with TES data within 1000 km of Hawaii for the same time period. 81

Figure 10-6 Comparison between V003 and V004 of the data before and after correction. 82

Figure 11-1 Example of TES/DACOM/AIRS comparison during INTEX-B. Top left: measured, retrieved and a priori/initial guess profiles. Thicker parts of TES and AIRS lines show the altitude region where retrievals have greatest sensitivity. Solid part of the DACOM line shows DACOM measurements, while dot-dashed parts of the DACOM line show the region that was extrapolated using the TES a priori constraint vector. Top right: Averaging kernels from the TES methane retrieval. Colored lines show averaging kernels for individual pressure levels while the dashed line shows the profile of the sum of the row of the averaging kernel (scaled by a factor of 0.1). Bottom right: Averaging kernels from the AIRS retrieval. Bottom left: TES, DACOM and AIRS RTVMR values, showing the regions over which the TES and AIRS retrievals have their greatest sensitivity. 85

Figure 11-2 Scatter plot of DACOM versus TES RTVMRs for INTEX-B measurements. The dotted line shows the 1:1 relationship, while the dashed line shows the mean high bias in the TES RTVMRs (+3.7 %). 86

Figure 11-3 Top row: Zonal means of RTVMR for July 2005 calculated using 10 degree latitude bins from TES, GEOS-Chem with TES averaging kernels and a priori applied, GEOS-Chem without the TES a priori applied, and the TES prior. Middle row: Differences of zonal means from GEOS-Chem, with bias removal based on the zonal means at 50-60S. Bottom row: zonal means of the diagonal element of the transformed averaging kernel in RTVMR space, showing sensitivity of the RTVMR to the measurement (as opposed to the a priori.) Left panels show results for the TES V004 data, while right panels show results for the TES V003 data. 87

Figure 12-1 2-D histogram of TES retrieved cloud top pressure and cloud effective optical depth at 975 cm^{-1} for Global Survey run ID 3396. The left panel shows the results for V003 and the right panel for V004. The color bar indicates the frequency of occurrence in fraction.. 92

Figure 12-2 TES retrieved cloud top pressure and cloud effective optical depth at 975 cm^{-1} with error estimates for runid 3396. 92

Figure 12-3 Histogram of Cloud Top Pressure Differences between MODIS and TES in hPa.. 93

Figure 12-4 Histogram of TES-MODIS cloud top pressure differences for V004 TES data. Left column is data with an effective optical depth less than 3, right hand column is for optical depths greater than 3. Upper row is cloud top pressure less than 350 hPa, bottom row is cloud top pressure greater than 700 hPa. 94

Figure 12-5 Comparison of histograms of cloud top pressure differences (TES-MODIS) for clouds with effective optical depth less than 3 and cloud top pressure less than 350 hPa for V002 (left panel) and V003 (right panel). The histogram for V003 is much more sharply peaked. 95

Figure 12-6 Scatterplot of MODIS visible cloud optical depth and TES effective cloud optical depth at 975 cm^{-1} 96

LIST OF TABLES

Table 1-1 Definitions of Data Maturity based on those used by the EOS-Terra MISR Team 1

Table 1-2 Current Validation Status of TES L2 Data Products 2

Table 2-1 Description of TES Global Survey Modifications 5

Table 2-2 Description of TES Special Observation Modes 6

Table 2-3 Description of the TES L2 Data Product Version Labels 9

Table 2-4 Description of the TES L2 Data Product Files Currently Available 11

1. Overview or TES Product Validation

This document is intended to provide our best determination of the quality of the TES data products based on detailed comparisons between TES L2 data products and other independent data sets.

Validation is defined, for purposes of this report, as comparison between quantities measured by TES and other data products that represent the state of the atmosphere. This definition will evolve as the validation effort matures. Data used in these figures come from processing at the TES Science Computing Facility and are all publicly available.

The TES L2 nadir products have undergone extensive quality control and validation testing. Table 1-1 shows the definitions of data maturity developed by the Terra-MISR (Multi-angle Imaging SpectroRadiometer) team and adopted by the TES team (http://eosweb.larc.nasa.gov/PRODOCS/misr/Quality_Summaries/maturity_def.html).

Using these definitions, the current validation status of the TES L2 data products are given in Table 1-2. Currently, all the TES L2 nadir products are ready for scientific use with the exception of the emissivity reported over land surfaces. TES methane products should be used in a manner similar to that outlined in Payne et al. 2009 (see section 11). The TES limb products are provisionally validated but should not be used without working with the TES team. Limb data was taken only for the first 9 months of the TES mission and some special observations in 2006. The TES limb data is provisionally validated, but should be used only in collaboration with the TES science team at JPL. This validation report does not include analysis of the limb data validation.

Table 1-1 Definitions of Data Maturity based on those used by the EOS-Terra MISR Team

Term	Definition
Beta	Early release products for users to gain familiarity with data formats and parameters.
Provisional	Limited comparisons with independent sources have been made and obvious artifacts fixed.
Validated Stage 1	Biases are estimated from independent measurements at selected locations and times.
Validated Stage 2	Biases are estimated from more widely distributed independent measurements.
Validated Stage 3	Biases are estimated from independent measurements representing global conditions.
Note: TES L2 retrievals include fully characterized internal error estimates and do not obtain error estimates from external sources. Uncertainty in the TES validation work describes biases when compared to other data sources.	

Table 1-2 Current Validation Status of TES L2 Data Products

Species	Validation Status
Nadir Ozone	Validated Stage 3
Nadir Carbon Monoxide	Validated Stage 3
Nadir Temperature	Validated Stage 3
Nadir Water (Lower/Middle Troposphere)	Validated Stage 3
Nadir Water (Upper Troposphere)	Validated Stage 2
Sea Surface Temperature	Validated Stage 3
Nadir Methane	Validated Stage 2
Sea Surface Temperature	Validated Stage 3
Cloud Properties	Validated Stage 2
Note: TES L2 limb products (Nitric Acid, Ozone, Temperature and Water) are provisionally validated but are not included in this report.	

In order to compare TES profile data with other measurements, vertical smoothing and sensitivity must be accounted for by applying the appropriate averaging kernels (such as those supplied with the TES data products). The error estimates included in the L2 data products are meaningful based on the current validation analysis.

1.1 Applicable Documents

Note: All TES documentation are available online at the TES website, http://tes.jpl.nasa.gov/documents/ and at the NASA (National Aeronautics and Space Administration) Langley Atmospheric Science Data Center (ASDC) http://eosweb.larc.nasa.gov/PRODOCS/tes/table_tes.html . All TES related publications are available at the TES web site http://tes.jpl.nasa.gov/documents/publications/

[1] Lewicki, S., D. Shepard, M. Madatyan and S. Gluck (2009), TES Science Data Processing Standard and Special Observation Data Products Specifications, Version 11.9, JPL Internal Report D-22993, May 26, 2009, for public released data, software release 11.3.

[2] Osterman, G., (editor), K. Bowman, K. Cady-Pereira, T. Clough, A. Eldering, B. Fisher, R. Herman, D. Jacob, L. Jourdain, S. Kulawik, M. Lampel, Q. Li, J. Logan, M. Luo, I. Megretskaia, R. Nassar, G. Osterman, S. Paradise, V. Payne, H. Revercomb., N.

Richards, M. Shephard, D. Tobin, S. Turquety, F. Vilnrotter, H. Worden, J. Worden, and L. Zhang (2007), Earth Observing System (EOS) Tropospheric Emission Spectrometer (TES) Data Validation Report (Version F04_04 data), Version 3.0, JPL Internal Report D-33192, November 5, 2007.

[3] Osterman, G., (editor), K. Bowman, A. Eldering, B. Fisher, R. Herman, D. Jacob, L. Jourdain, S. Kulawik, M. Luo, R. Monarrez, G. Osterman, S. Paradise, V. Payne, S. Poosti, N. Richards, D. Rider, D. Shepard, M. Shephard, F. Vilnrotter, H. Worden, J. Worden, H. Yun and L. Zhang (2009), Earth Observing System (EOS) Tropospheric Emission Spectrometer (TES) Level 2 (L2) Data User's Guide (Up to & including Version 4 data), Version 4.0, JPL Internal Report D-38042, May 20, 2009.

2. An Overview of the TES Instrument and Data Products

This section provides information about the TES instrument and the L2 data products. More detailed information on the TES data products is available in the TES L2 Data User's Guide (Osterman et al., 2009) and the TES Data Product Specification Document (Lewicki et al., 2009).

2.1 Instrument Description

The Tropospheric Emission Spectrometer (TES) on EOS-Aura was designed to measure the global, vertical distribution of tropospheric ozone and ozone precursors such as carbon monoxide (Beer et al., 2001; Beer, 2006). TES is a nadir and limb viewing infrared Fourier transform spectrometer (FTS) (http://tes.jpl.nasa.gov/instrument/). The TES spectral range is from 650 to 3250 cm^{-1}. The apodized resolution for standard TES spectra is 0.10 cm^{-1}, however, finer resolution (0.025 cm^{-1}) is available for special observations. The footprint of each nadir observation is 5 km by 8 km, averaged over detectors. Limb observations (each detector) have a projection around 2.3 km x 23 km (vertical x horizontal).

TES is on the EOS-Aura platform (http://aura.gsfc.nasa.gov/) in a near-polar, sun-synchronous, 705 km altitude orbit. The ascending node equator crossings are near 1:45 pm local solar time.

2.2 TES Observation Modes

2.2.1 Global Surveys

TES makes routine observations in a mode referred to as the "global survey". A global survey is run every other day on a predefined schedule and collects 16 orbits (~26 hours) of continuous data. Each orbit consists of a series of repetitive units referred to as a sequence. A sequence is further broken down into scans. Global surveys are always started at the minimum latitude of an Aura orbit. Table 2-1 provides a summary of the initial and modified versions of the TES Global Surveys from Launch to the present day.

Table 2-1 Description of TES Global Survey Modifications

Start Date/ First Run ID	Scans	Sequences	Maximum Number of TES L2 Profiles	Along-Track Distance between Successive Nadir Scan Locations	Description
August 22, 2004 / First GS Run ID 2026 (First 4 GS runs were 4 orbits only) (First full GS is Run ID 2147/Sep 20, 2004)	3 Limb/ 2 Nadir	1152 sequences (72 per orbit)	Maximum of 4608 L2 profiles (1152 sequences x (3 Limb Scans+ 1 Nadir Scan))	~544 km	• At-launch Global Survey (Aura launched on July 15, 2004) • Each sequence composed of 2 calibration scans, 2 nadir viewing scans and 3 limb scans. • The two nadir scans were acquired at the same location on the spacecraft ground track. Their radiances were averaged, providing a single TES L2 profile.
May 21, 2005 / Run ID 2931	3 Nadir	1152 sequences (72 per orbit)	Maximum of 3456 L2 profiles (1152 sequences x 3 nadir scans)	~182 km	• Global survey was modified to conserve instrument life. • Three limb scans were eliminated and replaced by an additional nadir scan. • The 3 Nadir scans were acquired at locations equally spaced along the spacecraft ground track. The radiances of individual scans are not averaged.
January 10, 2006 / Run ID 3239.	3 Nadir	1136 sequences (71 per orbit)	Maximum of 3408 L2 profiles (1136 sequences x 3 nadir scans)	~182 km	• The last sequence in each orbit was replaced with an instrument maintenance operation.
June 6, 2008 / Run ID 7370.	3 Nadir	960 sequences (60 per orbit)	Maximum of 2880 L2 profiles (960 sequences x 3 nadir scans)	~182 km	• Global survey was modified to conserve instrument life. • No measurements poleward of 60°S latitude.
July 30, 2008 / Run ID 8187.	3 Nadir	768 sequences (48 per orbit)	Maximum of 2304 L2 profiles (768 sequences x 3 nadir scans)	~182 km	• Global survey was further modified to conserve instrument life. • No measurements poleward of 50°S, 70°N latitude.

Start Date/ First Run ID	Scans	Sequences	Maximum Number of TES L2 Profiles	Along-Track Distance between Successive Nadir Scan Locations	Description
April 7, 2010 / Run ID 11125	4 Nadir	512 sequences (32 per orbit)	Maximum of 2048 L2 profiles (512 sequences x 4 nadir scans)	Spacing regular, but no longer uniform (56, 195, 187, 122 km)	• Global survey was further modified to conserve instrument life. • No measurements poleward of 30°S, 50°N latitude. • Blackbody calibrations reduced: no calibrations within the GS, only one pre-GS and one post-GS.

2.2.2 Special Observations

Observations are sometimes scheduled on non-global survey days. In general these are measurements made for validation purposes or with highly focused science objectives. These non-global survey measurements are referred to as "special observations". Eight special observation scenarios have been used to date and are summarized in Table 2-2.

Table 2-2 Description of TES Special Observation Modes

Name	Dates	Pointing	Sequences	Scans per Sequence	Distance Between Scans	Comments
Step and Stare	Sep 2004 through Aug 6, 2005	Nadir	6	25	40 km	Continuous along-track nadir views, ~45 degrees of latitude.
Step and Stare	July 1, 2007 through present	Nadir	1	165	45 km	Along track nadir observations spanning 65 degrees of latitude
Step and Stare	Jan 17, 2006 – Oct 8, 2006 and Spring 2008	Nadir	1	125	45 km	Continuous along-track nadir views, ~50 degrees of latitude.
Note: In 2008 both the 125 and 165 scan Step and Stare macros were used						
Transect	Jan 16, 2006 through present	Near Nadir	1	40	12 km	Hi density along-track or off nadir views.
Transect	Aug 20, 2005 – Sept 2, 2005	Near Nadir	1	68	25 km	Hi density along-track or off nadir views.

Name	Dates	Pointing	Sequences	Scans per Sequence	Distance Between Scans	Comments
Stare	Launch through present	Near Nadir	1	32	0 km	All measurements at a single location.
Limb Only	Jan 31, 2006 – May 20, 2006	Limb	1	62	45 km	Continuous along-track limb views, 25 degrees of latitude.
Limb HIRDLS	Feb 13, 2006 Only	Limb	142	3	182 km	2 orbits of continuous limb measurements for HIRDLS (High Resolution Dynamics Limb Sounder) comparison

2.3 TES Scan Identification Nomenclature

Each TES scan is uniquely identified by a set of three numbers called the run ID, the sequence ID and the scan ID. Each major unit of observation is assigned a unique run ID. Run IDs increase sequentially with time. The first on-orbit run ID is 2000. The sequence ID is assigned to repetitive units of measurements within a run. They start at 1 and are automatically incremented serially by the TES flight software. The scan ID is also incremented by the flight software each time a scan is performed. Each time the sequence is set to 1, the scan ID is reset to 0.

Each time TES makes a set of measurements, that data set is assigned an identification number (referred to as a "run ID"). A calendar of the TES run IDs for global surveys and a list of all TES run IDs (including observation data, time and date) can be found at http://tes.jpl.nasa.gov/data/datacalendar/)

2.4 Where to Obtain TES Data

There are two locations for obtaining TES data. Links to both locations are available from the TES site at the Langley Atmospheric Science Data Center (ASDC) http://eosweb.larc.nasa.gov/. The supporting documentation necessary to use TES data is also available at the Langley ASDC site.

- The primary location for obtaining TES data is the Earth Observing System (EOS) Data Gateway https://wist.echo.nasa.gov/api/. This site makes available earlier versions of the TES data.
- A secondary location for obtaining TES data is the Langley ASDC data pool. The data pool has space limitations that make it somewhat dynamic, therefore older versions of TES data may not be available there.

The TES data files are listed in different ways for the different sites. The naming convention will be described in Section 2.5.

All TES data products are in HDF-EOS 5 format and are completely documented in the TES Data Product Specification documents referenced at http://tes.jpl.nasa.gov/documents/ . The site also contains links to the TES documentation mentioned in this manuscript.

Routines for reading the TES Level 2 data products, written in IDL, are available at ASDC TES site. We expect to have IDL routines for determining "C-Curve" ozone retrievals (see section 5.1.1.2 of the TES L2 Data User's Guide (Osterman et al., 2009)) available at the ASDC as well.

2.5 File Formats and Data Versions

Information about the TES data file content and format versioning can be found in the L2 product filenames. Table 2-3 provides information for differentiating between the TES versions. When ordering the data on the EOS Data Gateway, the TES level 2 products can be initially differentiated by the TES Product (ESDT or Earth Science Data Type) version label shown in the first column of Table 2-3. Once the data is downloaded, more information can be gathered from the TES version string in the filename.

The TES L2 Data Products are provided in files separated out by the atmospheric species being measured. The parts of the product filename are:

<inst.>-<platform>_<process level>-<species>-<TES view mode>_r<run id>_<version id>.he5

The TES Version String (version id), contains the Format and content version:

F<format version>_<science content version>

A change to the format version string corresponds to minor updates to the fields available within the file or minor bug fixes. Changes to the science content string reflect major changes in the science content of certain fields in the data products.

An example file name is:

TES-Aura_L2-O3-Nadir_r000002945_F04_04.he5

This particular file contains TES nadir measurements of ozone for run ID 2945 (000002945).

In addition to the atmospheric products, there are data files with additional (ancillary) data that are important for working with TES data. These ancillary files can be used with any species data file and contain the string "Anc" in the filename.

Table 2-3 provides a way to map the TES version string information to the TES data product version. For example, version F03_03 is the first version to contain limb data and version F03_02 data was a significant upgrade to the science content in the data products and therefore is referred to as version 2 (V002) TES data. When ordering TES Level 2 data products through the EOS Data Gateway, the products will be grouped by the TES version number (ESDT) in a form that looks like:

TES/AURA L2 O3 NADIR V003.

If the TES data is ordered through the Langley ASDC Data Pool using the FTP (File Transfer Protocol) interface, the version 3 nadir ozone data will be listed in the form:

TL2O3N.003.

If the TES data is ordered through the Langley Data Pool using the Web interface, the version 3 nadir ozone data will be listed as:

TL2O3N.3.

While the data may be listed differently for the different sites for downloading the products, the filenames will be identical.

There are six different versions of TES L2 data products. It is currently planned that all TES L2 data products should be processed with the latest software release by the end of the 2009 calendar year (complete set of V004 (F05_07) L2 data products). Until that time, there will be a mixture of F04_04 and (F05_05, F05_06, F05_07) data products available. Data from versions prior to V003 (F04_04) are no longer publicly available, but the evolution of the product versions and file formats is provided in this document back to V001 (F01_01 and F02_01).

Table 2-3 Description of the TES L2 Data Product Version Labels

TES Product (ESDT) Version	TES Version String	Format Version	Science Content Version	Description
V001	F01_01	1	1	The first publicly released L2 data
V001	F02_01	2	1	Bug fixes and additional fields
V002	F03_02	3	2	Some additional fields but major upgrade to scientific quality of data.
V002	F03_03	3	3	Limb data and some bug fixes
V003	F04_04	4	4	Improvements to nadir ozone, temperature, methane and to limb products. Fully processed from Sep 2004 through present.

TES Product (ESDT) Version	TES Version String	Format Version	Science Content Version	Description
V004	F05_05 or F05_06 F05_07 (Final V004)	5	5,6 or 7	Improvements to temperature and methane retrievals. F05_07 is the final V004 release using retrieval software R11.3 and when available should be used over F05_05 or F05_06. F05_07 differentiates between GMAO* versions used in retrieval by date and TES run ID (see below) F05_05 refers to data processed using GMAO GEOS-5.1.0 products using TES retrieval software release R11.2 F05_06 refers to data processed using GMAO GEOS-5.2.0 products using TES retrieval software release R11.2

** The TES processing software uses meteorological fields from the NASA Global Modeling and Assimilation Office (GMAO) GEOS (Goddard Earth Observing System) model as inputs to the Level 2 data retrievals.*

2.6 TES Standard L2 Products

Currently the TES data products available for any given run ID are listed in . The products are separated by species with an ancillary file providing additional data fields applicable to all species. A description of the contents of the product files, information on the Earth Science Data Type names and file organization can be found in the TES Data Processing Specification (DPS) document (Lewicki, et al., 2009).

Table 2-4 Description of the TES L2 Data Product Files Currently Available

TES L2 Standard Data Product	TES View Mode	Description
Ozone	Nadir and Limb	TES ozone profiles and some geolocation information
Temperature	Nadir and Limb	TES atmospheric temperature profiles and some geolocation information.
Water Vapor	Nadir and Limb	TES nadir water vapor profiles and some geolocation information
Carbon Monoxide	Nadir	TES nadir carbon monoxide profiles and some geolocation information
HDO	Nadir and Limb	TES HDO (Hydrogen Deuterium Monoxide) profiles and some geolocation information
Methane	Nadir	TES nadir methane profiles and some geolocation information
Nitric Acid	Limb	TES limb nitric acid profiles and some geolocation information
Ancillary	Nadir and Limb	Additional data fields necessary for using retrieved profiles.
Summary	Nadir and Limb	Provides information on retrieved volume mixing ratios/temperatures without averaging kernel, error matrices.
Supplemental	Nadir and Limb	Provides information on non-retrieved species that are used in the Level 2 retrievals (climatologies, covariance matrices, etc.)

TES retrieves surface temperature and it is reported in each nadir species file, however the value in the atmospheric temperature file is the one that should be used for scientific analysis.

2.7 References

2.7.1 TES References

[1] Beer, R., T. A. Glavich, and D. M. Rider (2001), Tropospheric emission spectrometer for the Earth Observing System's Aura satellite, Applied. Optics, 40 (15), 2356-2367, May 20, 2001.

[2] Beer, R. (2006), TES on the Aura Mission: Scientific Objectives, Measurements and Analysis Overview, IEEE Transactions on Geoscience and Remote Sensing, 44 (No.5), Special Issue on Aura, 1102-1105, May 2006.

[3] Lewicki, S., D. Shepard, M. Madatyan and S. Gluck (2009), TES Science Data Processing Standard and Special Observation Data Products Specifications, Version 11.9, JPL Internal Report D-22993, May 26, 2009, for public released data, software release 11.3.

[4] Osterman, G., (editor), K. Bowman, A. Eldering, B. Fisher, R. Herman, D. Jacob, L. Jourdain, S. Kulawik, M. Luo, R. Monarrez, G. Osterman, S. Paradise, V. Payne, S. Poosti, N. Richards, D. Rider, D. Shepard, M. Shephard, F. Vilnrotter, H. Worden, J. Worden, H. Yun and L. Zhang (2009), Earth Observing System (EOS) Tropospheric Emission Spectrometer (TES) Level 2 (L2) Data User's Guide (Up to & including Version 4 data), Version 4.0, JPL Internal Report D-38042, May 20, 2009.

3. Executive Summary

Below is a summary of each data validation section.

- **Section 4 – L1B Radiance:**

Validation of level 1B radiance retrievals was reported by M. W. Shephard et al. (2008). The reader is referred to the previous version TES Validation Report V003 (Osterman et al., 2007) for details.

- **Section 5 – Nadir Ozone:**

Overall, we compare TES V004 nadir ozone profiles using the TES global survey, step-and-stare, transect, and stare retrieval modes with ozonesonde profiles from the Intercontinental Chemical Transport Experiment Ozonesonde Network Study (IONS), the World Ozone and Ultraviolet Radiation Data Center (WOUDC), the Global Monitoring Division of the Earth System Research Laboratory (GMD-ESRL), and the Southern Hemisphere Additional Ozonesonde archives (SHADOZ). Approximately 5000 matches are found using the coincidence criteria of ±3 h and a 300 km radius, spanning a latitude range and time-span from 72.5^{o} S to 80.3^{o} N and 2004 to 2008; the majority of matches were also found by removing cloudy scenes and flagged TES data. The TES averaging kernel and constraint are applied to the ozonesonde data to: 1) compare the TES retrieval and ozonesonde data in an unbiased quantifiable manner (i.e. not biased by the TES a priori) and 2) account for the TES measurement sensitivity and vertical resolution. Excluding profiles with thick clouds, TES-sonde percent and absolute differences were investigated in six latitude zones and, also, during the spring, summer, fall, and winter. TES V004-ozonesonde comparisons, overall, produce percent and absolute biases that are congruent to previous validation studies of TES V001 and V002.

We also compare TES V003 and V004 nadir stare ozone profiles with ozonesonde profiles from the Arctic Intensive Ozonesonde Network Study (ARCIONS, http://croc.gsfc.nasa.gov/arcions/) during the Arctic Research on the Composition of the Troposphere from Aircraft and Satellites (ARCTAS) field mission, SHADOZ, and the Tropospheric Ozone Pollution Project (TOPP, http://physics.valpo.edu/ozone/fulbrightdata.html). The ozonesonde data are from launches timed to match Aura's overpass, where 22 coincidences spanned 5° S to 71° N from April, 2008 to October, 2009. Using the TES "stare" observation mode, 32 observations are taken over each coincident ozonesonde launch within about 2 minutes. By effectively sampling the same air mass 32 times, the observed variability can be attributed almost entirely to the random errors of the TES retrievals, thus allowing for the first time comparisons to be made between the empirically-calculated random errors to the expected random errors from measurement noise, temperature, and interfering species, such as water. This is primarily due to the fact that TES instrument pointed to the location of each sonde launch, thus greatly reducing the temporal/spatial mismatch. For example, the temporal overlap ranges from 3 minutes to about 3 h. This study represents the first validation of high latitude (> 70°) TES ozone, using the TES retrieval mode. We find that the calculated errors are consistent with the actual errors with a similar vertical distribution that varies between 5% and 20% for V003 and V004 TES data. The TES stare retrieval mode characterizes the better the bias between the TES ozone profiles, because the standard error of the mean between the ensemble of TES ozone profiles from each "stare" as compared to the ozone-sonde profile will be much smaller than in the previous studies. In

general, TES ozone profiles are positively biased (by less than 15%) from the surface to the upper-troposphere (~ 1000 to 100 hPa) and negatively biased (by less than 20%) from the upper-troposphere to the lower-stratosphere (100 to 30 hPa) when compared to the ozone-sonde data. Lastly, for V003 and V004 TES data between 44° N and 71° N there is variability in the mean biases (from –14 to +15%), mean theoretical errors (from 6 to 13%), and mean random errors (from 9 to 19%).

Given the significantly larger number of coincidences (totaling 2863 from 35 to 56° N latitude) of TES V004 ozone, the seasonal variability of ozone was investigated. Overall, for all seasons, for TES V004 ozone, profiles are positively biased (by less than 15%) from the surface to the upper-troposphere (~ 1000 to 100 hPa) and negatively biased (by less than 20%) from the upper-troposphere to the lower-stratosphere (100 to 30 hPa) when compared to the ozone-sonde data. Both these features are consistent with that of Boxe et al. (2010). The absolute mean percent differences for all seasons for mid-to-lower tropospheric ozone also show an improvement when compared to Nassar et al. (2008).

- **Section 6 – Carbon Monoxide:**

Comparisons have been carried out between TES carbon monoxide retrievals and those from a variety of satellite and aircraft instruments. Global patterns of carbon monoxide as measured by TES are in good qualitative agreement with those seen by MOPITT on the NASA Terra satellite. Comparisons of profiles of CO between TES and MOPITT show good agreement when a priori information is accounted for correctly. TES carbon monoxide agrees to within the estimated uncertainty of the aircraft instruments, including both errors and the variability of CO itself. TES V004 CO data values do not show systematic changes from V003 with increased number of good quality retrieved profiles.

- **Section** 7 **– Nadir Temperature:**

TES V004 data feature improvements that significantly impact nadir temperature retrievals**.** Improvements were made to the forward model, retrieval strategy, constraints, and climatology (Herman et al., (in prep); Shephard et al., 2008). TES V004 temperature retrievals have been compared with nearly coincident radiosonde (hereafter sonde) measurements from the NCEP database for temperature bias analysis. The bias in the TES nadir temperature retrievals is significantly reduced in V004 to <0.7 K, compared with a 1 to 2 K upper tropospheric cold bias in V003. Here is a breakdown of the bias with different criteria:

bias over ocean is <0.6 K (531 TES-sonde matches),

bias over land is <0.5 K (1118 matches),

TES nadir temperature retrievals were also compared with the NOAA ESRL database for analysis of temperature rms. This database provides a better estimate of rms because exact sonde launch times are known, which allows a closer match in time to the TES retrieval. The TES temperature rms in V004 is 1 K in the stratosphere and upper troposphere and 1.5 K in the lower troposphere (at 500 to 900 hPa), compared to 2-4 K in V003. There is 0.5 to 1 K uncertainty simply due to the spatial and temporal variability of atmospheric temperature.

- **Section 8 – Sea Surface Temperature:**

TES retrievals of sea surface temperature rely on validation of previous data versions, as described in detail in the TES Validation Report V003 (Osterman et al., 2007).

- **Section 9 – Water Vapor:**

For purposes of evaluating the quality of TES water vapor retrievals, the most readily available correlative data are provided by radiosondes. In this study, TES water vapor retrievals are compared with nearly coincident radiosonde measurements. Radiosonde data come from a global database from the National Oceanic and Atmospheric Administration (NOAA) Earth System Research Laboratory (ESRL) Global Systems Division [M. Govett, pers. comm.]. The NOAA ESRL database combines the IGRA global data with North American Global Telecommunications Service (GTS) radiosonde observations. This database features the exact radiosonde launch time, which improves the temporal coincidence between TES and radiosonde significantly. The disadvantage of radiosondes is the spatial mismatch between the satellite retrieval footprint (8 km by 5 km for TES) and the radiosonde data (a vertical profile of in-situ measurement with no horizontal information).

Comparisons have been made between TES V004 water vapor profiles and radiosonde profiles for five years of data (2004-2008). At nighttime, TES has a slight dry bias of 0 to 15% compared to radiosondes, driest bias at 700-800 hPa in the lower troposphere. The rms differences tend to increase from 20% near the surface to 40% in the upper troposphere.

- **Section 10 – HDO/H_2O:**

TES is capable of measuring the HDO/H_2O ratio in the troposphere using thermal infrared radiances between 1200 and 1350 cm^{-1}. Information on the simultaneous retrieval of HDO and H_2O is provided in Worden et al., (2006), including a description of error characterization and vertical sensitivities. The TES measurement of HDO is made in the nadir mode and is most sensitive in the region between 450 and 825 hPa.

From October 11 through November 5 2008, we undertook a validation campaign of the TES water isotope measurements. This Validation of V003 of the TES HDO/H_2O ratio is performed using direct and indirect comparisons of TES measurements over and near the Hawaii Mauna Loa observatory in conjunction with flask measurements at Mauna Loa taken by University of New Mexico and high speed data using cavity ring laser measurements from JPL (Lance Christenson PI, ref: Webster and Heymsfield 2003) and from Los Gatos Research and Picarro that was lent to the University of Colorado and University of New Mexico (David Noone and Joe Galewsky PI). The objective is to better characterize the bias expected in TES HDO/H_2O estimates (Worden et al., 2006).

These comparisons, as discussed in the next sections indicate that the TES HDO/H_2O profiles for V003 need to be adjusted by approximately 6%, accounting for the TES sensitivity of the measurement. As discussed in Section 10.2 of this report and in (Worden et al., 2011) the form for the correction should be:

$$\ln(\mathbf{q}^{HDO}_{corrected}) = \ln(\mathbf{q}^{HDO}_{original}) - \mathbf{A}(\vec{\delta}_{bias}) \quad (1)$$

where $\mathbf{q}^{HDO}_{original}$ is the volume mixing ratio of the HDO profile as provided in the product files, A is the averaging kernel matrix (also provided in the product files), and $\vec{\delta}_{bias}$ is a column vector of the same length as $\mathbf{q}^{HDO}_{original}$ that contains the values 0.06. Note that this correction is only applied to HDO and not to H_2O. For this release, this correction should be applied by the user of the data. For Release 2, we recommend that the user apply a value of 0.045. The difference between the two releases is due to a change in how temperature is estimated in the TES retrievals.

- **Section 11 – Methane:**

Validation of the TES methane product is ongoing. Work so far indicates that the TES methane product does contain useful information, when viewed in an appropriate representation. The use of "representative tropospheric volume mixing ratios" (RTVMRs) has been shown to be valuable. TES V004 methane shows a 3.7 % mean high bias (4.4 % rms difference) with respect to DACOM in-situ aircraft measurements and a 6 % high bias with respect to AIRS v5.0 for comparisons of INTEX-B campaign measurements. TES V004 methane shows a 5 % high bias with respect to GEOS-Chem global monthly mean fields. Latitudinal gradients in TES methane are similar to those in GEOS-Chem, although TES latitudinal gradients are slightly stronger during northern hemisphere summer months.

- **Section 12 – Cloud Products:**

There was one significant change to the TES retrieval algorithm in V004 related to clouds. This was the separation of the retrievals of water, ozone and temperature into separate steps in software.

In looking at the difference between TES and MODIS cloud top pressure, We see reasonable agreement in V004 though not as good as in V003. The mean was reduced to 0.0 hPa in V003, from 48 hPa in V002, but we still see that there are outliers with differences of greater than 300 hPa. In V004, there are now more retrievals with a difference between 100 and 200 hPa, with a large increase near 150 hPa.

At present, we have limited correlative datasets for the validation of the effective cloud optical depth product from TES. For characterization purposes, we have compared MODIS visible optical depths to the TES effective cloud optical depths retrieved at 975 cm^{-1}. The average effective cloud optical depth is very well correlated to the effective cloud optical depth at 975 cm^{-1}, except at small effective optical depth, as shown in previous validation reports.

The expected ratio of visible to infrared optical depth is dependent on the cloud particle sizes and shapes, and is thought to be on the order of 2. A scatter plot of TES effective cloud optical depth at 975 cm^{-1} and MODIS cloud optical depth shows clearly that MODIS optical depths are larger than those from TES, but the scaling ranges from a factor of 10 to 1.

3.1 References

3.1.1 TES References

[1] Herman, R.L., M. W. Shephard, K. E. Cady-Pereira, V. H. Payne, B. M. Fisher, S. S. Kulawik, G. B. Osterman, A. Eldering, S. Pawson, and D. N. Whiteman, New Comparisons of Tropospheric Emission Spectrometer Version 4 Temperature Retrievals with Radiosonde Measurements, in preparation.

[2] Osterman, G., (editor), K. Bowman, K. Cady-Pereira, T. Clough, A. Eldering, B. Fisher, R. Herman, D. Jacob, L. Jourdain, S. Kulawik, M. Lampel, Q. Li, J. Logan, M. Luo, I. Megretskaia, R. Nassar, G. Osterman, S. Paradise, V. Payne, H. Revercomb., N. Richards, M. Shephard, D. Tobin, S. Turquety, F. Vilnrotter, H. Worden, J. Worden, and L. Zhang (2007), Earth Observing System (EOS) Tropospheric Emission Spectrometer (TES) Data Validation Report (Version F04_04 data), Version 3.0, JPL Internal Report D-33192, November 5, 2007.

[3] Shephard, M. W., V. H. Payne, K. E. Cady-Pereira, R. L. Herman, S. S. Kulawik, B. M. Fisher, A. Eldering, and S. A. Clough (2008), Investigation of biases in the TES temperature retrievals, Eos Trans. AGU, 89(23), Joint Assembly Supplement, Abstract A31A-02 (2008).

[4] Worden, J., K. Bowman, D. Noone, R. Beer, S. Clough, A. Eldering, B. Fisher, A. Goldman, M. Gunson, R. Herman, S. S. Kulawik, M. Lampel, M. Luo, G. Osterman, C. Rinsland, C. Rodgers, S. Sander, M. Shephard, and H. Worden (2006), Tropospheric Emission Spectrometer observations of the tropospheric HDO/H_2O ratio: Estimation approach and characterization, *Journal of Geophysical Research, 111*, D16309, (doi:10.1029/2005JD006606) August 25, 2006.

[5] Worden, J., D. Noone, J. Galewsky, A. Bailey, K. Bowman, D. Brown, J. Hurley, S. Kulawik, J. Lee, and M. Strong, Estimate of bias in Aura TES HDO/H2O profiles from comparison of TES and in situ HDO/H2O measurements at the Mauna Loa observatory, *Atmospheric Chemistry and Physics, 11,* 4491–4503, 2011, doi:10.5194/acp-11-4491-2011, May 12, 2011.

3.1.2 General References

[6] Webster, C. R., and A. J. Heymsfield (2003), Water Isotope Ratios D/H, $^{18}O/^{16}O$, $^{17}O/^{16}O$ in and out of Clouds Map Dehydration Pathways, *Science, Vol. 302, no. 5651,* 1742-1745, (DOI: 10.1126/science.1089496), December 5, 2003.

4. L1B Radiance

Validation of level 1B radiance retrievals was reported by M. W. Shephard et al. (2008). The reader is referred to the previous version TES Validation Report V003 (Osterman et al., 2007) for details.

4.1 References

4.1.1 TES L1B Radiance Validation Reference

[1] Osterman, G., (editor), K. Bowman, K. Cady-Pereira, T. Clough, A. Eldering, B. Fisher, R. Herman, D. Jacob, L. Jourdain, S. Kulawik, M. Lampel, Q. Li, J. Logan, M. Luo, I. Megretskaia, R. Nassar, G. Osterman, S. Paradise, V. Payne, H. Revercomb., N. Richards, M. Shephard, D. Tobin, S. Turquety, F. Vilnrotter, H. Worden, J. Worden, and L. Zhang (2007), Earth Observing System (EOS) Tropospheric Emission Spectrometer (TES) Data Validation Report (Version F04_04 data), Version 3.0, JPL Internal Report D-33192, November 5, 2007.

[2] Shephard, M. W., H. M. Worden, K. E. Cady-Pereira, M. Lampel, M. Luo, K. W. Bowman, E. Sarkissian, R. Beer, D. M. Rider, D. C. Tobin, H. E. Revercomb, B. M. Fisher, D. Tremblay, S. A. Clough, G. B. Osterman, and M. Gunson (2008), Tropospheric Emission Spectrometer Nadir Spectral Radiance Comparisons, *J. Geophys. Res., 113*, D15S05, (doi:10.1029/2007JD008856), April 22, 2008.

4.1.2 TES References

[3] Bowman K. W., C. D. Rodgers, S. S. Kulawik, J. Worden, E. Sarkissian, G. Osterman, T. Steck, M. Lou, A. Eldering, M. Shephard, H. Worden, M. Lampel, S. A. Clough, P. D. Brown, C. P. Rinsland, M. Gunson, and R. Beer (2006), Tropospheric emission spectrometer: Retrieval method and error analysis, *IEEE Trans. Geosci. Remote Sens., 44(5)*, 1297-1307, May 2006.

[4] Clough, S. A., M. W. Shephard, E. J. Mlawer, J. S. Delamere, M. J. Iacono, K. Cady-Pereira, S. Boukabara, and P. D. Brown (2005), Atmospheric radiative transfer modeling: a summary of the AER codes, Short Communication, *J. Quant. Spectrosc. Radiat. Transfer, 91* (2005) 233-244.

[5] Worden, J., S. S. Kulawik, M. W. Shephard, S. A. Clough, H. Worden, K. Bowman, and A. Goldman (2004), Predicted errors of tropospheric emission spectrometer nadir retrievals from spectral window selection, *J. Geophys. Res., 109*, *D09308,* May 15, 2004.

4.1.3 General References

[6] Aumann, H. H., M. T. Chahine, C. Gautier, M. D. Goldberg, E. Kalnay, L. M. McMillin, H. Revercomb, P. W. Rosenkranz, W. L. Smith, D. H. Staelin, L. L. Strow, and J. Susskind (2003), AIRS/AMSU/HSB on the Aqua mission: Design, Science Objectives, Data Products, and Processing Systems, *IEEE Trans. Geosci. Remote Sensing, 41,* 253-264 (2003).

[7] Aumann, H. H., S. Broberg, D. Elliott, S. Gaiser, and D. Gregorich (2006), Three years of Atmospheric Infrared Sounder radiometric calibration validation using sea surface temperatures, *J. Geophys. Res., 111,* (doi:10.1029/2005JD006822), 2006.

[8] Bloom, S., A. da Silva, D. Dee, M. Bosilovich, J.-D. Chern, S. Pawson, S. Schubert, M. Sienkiewicz, I. Stajner, W.-W. Tan, M.-L. Wu (2005). Documentation and Validation of the Goddard Earth Observing System (GEOS) Data Assimilation System - Version 4. Technical Report Series on Global Modeling and Data Assimilation 104606, Vol. 26, 187 pages, April 2005. Available from (paste entire link including pdf into browser):

http://ntrs.nasa.gov/archive/nasa/casi.ntrs.nasa.gov/20050175690_2005173043.pdf

[9] Gauss M., G. Myhre, G. Pitari, M. J. Prather, I. S. A. Isaksen, T. K. Berntsen, G. P. Brasseur, F. J. Dentener, R. G. Derwent, D. A. Hauglustaine, L. W. Horowitz, D. J. Jacob, M. Johnson, K. S. Law, L. J. Mickley, J.-F. Muller, P.-H. Plantevin, J. A. Pyle, H. L. Rogers, D. S. Stevenson, J. K. Sundet, M. van Weele, and O. Wild (2003), Radiative forcing in the 21st century due to ozone changes in the troposphere and the lower stratosphere. *J. Geophys. Res., 108(D9)*, 4292 (2003).

[10] Hagan, D. E., and P. J. Minnett (2003), AIRS Radiance Validation Over Ocean From Sea Surface Temperature Measurements, *IEEE Trans. Geosci. Remote Sensing, 41*, 432-441, (2003).

[11] Revercomb, H. E., H. Buijs, H. B. Howell, D. D. LaPorte , W. L. Smith, and L. A. Sromovsky (1988a), Radiometric calibration of IR Fourier transform spectrometers: solution to a problem with the High-Resolution Interferometer Sounder, *Appl. Opt.,Vol. 27*, *Issue 15,* 3210-3218 (1988a).

[12] Revercomb, H. E., D. D. LaPorte, W. L. Smith, H. Buijs, D. G. Murcray, F. J. Murcray, and L.A. Sromovsky (1988b), High-Altitude Aircraft Measurements of Upwelling IR Radiance: Prelude to FTIR from Geosynchronous Satellite, *Mikrochimica Acta [Wien], II,* 439-444 (1988b).

[13] Revercomb, H. E., W. L. Smith, F. A. Best, J. Giroux, D. D. LaPorte, R. O. Knuteson, M. W. Werner, J. R. Anderson, N. N. Ciganovich, R. W. Cline, S. D. Ellington, R. G. Dedecker, T. P. Dirkx, R. K. Garcia, and H. B. Howell (1996), Airborne and ground-based Fourier transform spectrometers for meteorology: HIS, AERI and the new AERI-UAV. Proceedings SPIE Optical Instruments for Weather Forecasting, ed. G.W. Kamerman, 2832, 106-117 (1996).

[14] Tobin, D.C., H. E. Revercomb, R. O. Knuteson, F. A. Best, W. L. Smith, N. N. Ciganovich, R. G. Dedecker, S. Dutcher, S. D. Ellington, R. K. Garcia, H. B. Howell, D. D. LaPorte, S. A. Mango, T. S. Pagano, J. K. Taylor, P. van Delst, K. H. Vinson, and M. W. Werner (2006), Radiometric and spectral validation of Atmospheric Infrared Sounder observations with the aircraft-based Scanning High-Resolution Interferometer Sounder, *J. Geophys. Res., 111, D09S02*, (doi:10.1029/2005JD006094), 2006.

5. Validation of TES V004 nadir ozone profiles using ozonesonde measurements

5.1 Overview

Overall, we compare TES V004 nadir ozone profiles using the TES global survey, step-and-stare, transect, and stare retrieval modes with ozonesonde profiles from the Intercontinental Chemical Transport Experiment Ozonesonde Network Study (IONS), the World Ozone and Ultraviolet Data Center (WOUDC), the Global Monitoring Division of the Earth System Research Laboratory (GMD-ESRL), and the Southern Hemisphere Additional Ozonesonde archives (SHADOZ). Approximately 5000 matches are found using the coincidence criteria of ±3 h and a 300 km radius, spanning a latitude range and time-span from 72.5^o S to 80.3^o N and 2004 to 2008; the majority of matches were also found by removing cloudy scenes and flagged TES data. The TES averaging kernel and constraint are applied to the ozonesonde data to: 1) compare the TES retrieval and ozonesonde data in an unbiased quantifiable manner (i.e. not biased by the TES a priori) and 2) account for the TES measurement sensitivity and vertical resolution. Excluding profiles with thick clouds, TES-sonde percent and absolute differences were investigated in six latitude zones and, also, during the spring, summer, fall, and winter. TES V004-ozonesonde comparisons, overall, produce percent and absolute biases that are congruent to previous validation studies of TES V001 and V002.

We also compare TES V003 and V004 nadir stare ozone profiles with ozonesonde profiles from the Arctic Intensive Ozonesonde Network Study (ARCIONS, http://croc.gsfc.nasa.gov/arcions/) during the Arctic Research on the Composition of the Troposphere from Aircraft and Satellites (ARCTAS) field mission, SHADOZ, and the Tropospheric Ozone Pollution Project (TOPP, http://physics.valpo.edu/ozone/fulbrightdata.html). The ozonesonde data are from launches timed to match Aura's overpass, where 22 coincidences spanned 5° S to 71° N from April, 2008 to October, 2009. Using the TES "stare" observation mode, 32 observations are taken over each coincident ozonesonde launch within about 2 minutes. By effectively sampling the same air mass 32 times, the observed variability can be attributed almost entirely to the random errors of the TES retrievals, thus allowing for the first time comparisons to be made between the empirically-calculated random errors to the expected random errors from measurement noise, temperature, and interfering species, such as water. This is primarily due to the fact that TES instrument pointed to the location of each sonde launch, thus greatly reducing the temporal/spatial mismatch. For example, the temporal overlap ranges from 3 minutes to about 3 h. This study represents the first validation of high latitude (> 70°) TES ozone, using the TES retrieval mode. We find that the calculated errors are consistent with the actual errors with a similar vertical distribution that varies between 5% and 20% for V003 and V004 TES data. The TES stare retrieval mode characterizes the better the bias between the TES ozone profiles, because the standard error of the mean between the ensemble of TES ozone profiles from each "stare" as compared to the ozone-sonde profile will be much smaller than in the previous studies. In general, TES ozone profiles are positively biased (by less than 15%) from the surface to the upper-troposphere (~ 1000 to 100 hPa) and negatively biased (by less than 20%) from the upper-troposphere to the lower-stratosphere (100 to 30 hPa) when compared to the ozone-sonde data. Lastly, for V003 and V004 TES data between 44° N and 71° N there is variability in the mean

biases (from –14 to +15%), mean theoretical errors (from 6 to 13%), and mean random errors (from 9 to 19%).

Given the significantly larger number of coincidences (totaling 2863 from 35 to 56° N latitude) of TES V004 ozone, the seasonal variability of ozone was investigated. Overall, for all seasons, for TES V004 ozone, profiles are positively biased (by less than 15%) from the surface to the upper-troposphere (~ 1000 to 100 hPa) and negatively biased (by less than 20%) from the upper-troposphere to the lower-stratosphere (100 to 30 hPa) when compared to the ozone-sonde data. Both these features are consistent with that of Boxe et al. (2010). The absolute mean percent differences for all seasons for mid-to-lower tropospheric ozone also show an improvement when compared to Nassar et al. (2008).

5.2 TES Ozonesonde Comparisons

An unbiased (i.e., from the a priori) and quantitative comparison is made between TES V001, V002, V003, and V004. This is done by applying the TES operator to ozonesonde profiles. This facilitates direct comparison by smoothing the sonde data with the TES averaging kernel and also allows calculation of a TES-sonde percent and absolute difference. In these comparisons, regions where TES has low sensitivity (e.g., cloudy scenes or the Arctic/Antarctic LT), results in low values for the TES averaging kernel; therefore, such scenarios are screened by inspecting the averaging kernels and the effective optical depth in the LT. This procedure is important as it avoids mistaking a lack of sensitivity (or low averaging kernel) for good agreement between the data sets – *i.e.*, the TES percent and absolute differences. In this chapter, TES-sonde matches were identified and filtered using the TES SondeTool idl code (developed mainly by P. Saha), and plotted with idl code written by K. Cady-Pereira.

Note: the majority of the proceeding discussion will pertain to TES V002 validation study (Nassar et al., 2008), as it described the comparison of about 1600 coincidences, spanning 72° S to 80° N from October 2004 to October 2006, compared to Worden et al. (2007), that compared about 40 coincident measurements, spanning 14° S to 59° N during the fall of 2004 (Figure 5-1). Figure 5-1 reveals a clear bias, with TES measuring higher ozone in the UT, peaking at about 200 hPa. Ozone percent and absolute difference (or bias) profiles are shown in Figure 5-2 (i.e., TES V004 minus sonde) for six latitude zones (i.e., the Arctic, north midlatitudes, northern subtropics, tropics, southern low- and midlatitudes, and Antarctic). The southern low (subtropics) and midlatitudes were combined as a single zone because of the small number of coincident TES-ozonesonde measurements (122 matches). Percent and absolute difference profiles are shown from the surface up to 10 hPa (left panels). In Figure 5-2, all individual profiles are plotted in gray, mean and standard deviation ranges are overlaid in dark blue and broken light blue, respectively. The mean minus standard deviation and mean plus standard deviation (or the one standard deviation ranges) are overlaid in black. The number of profiles is referred to by 'n.' Figure 5-3 shows TES-sonde ozone percent differences and absolute differences in the same latitude zones as Figure 5-2. In Figure 5-3, percent and absolute difference profiles are shown from the surface up to 10 hPa (left panels) and 200 hPa (right panels), respectively. A height of 200 hPa was chosen for absolute difference plots to focus on the troposphere. Individual profiles are shown in gray, and the mean and 1 standard deviation range are overlaid in black. *N* is the number of profiles plotted after removing cloudy scenes and flagged TES data.

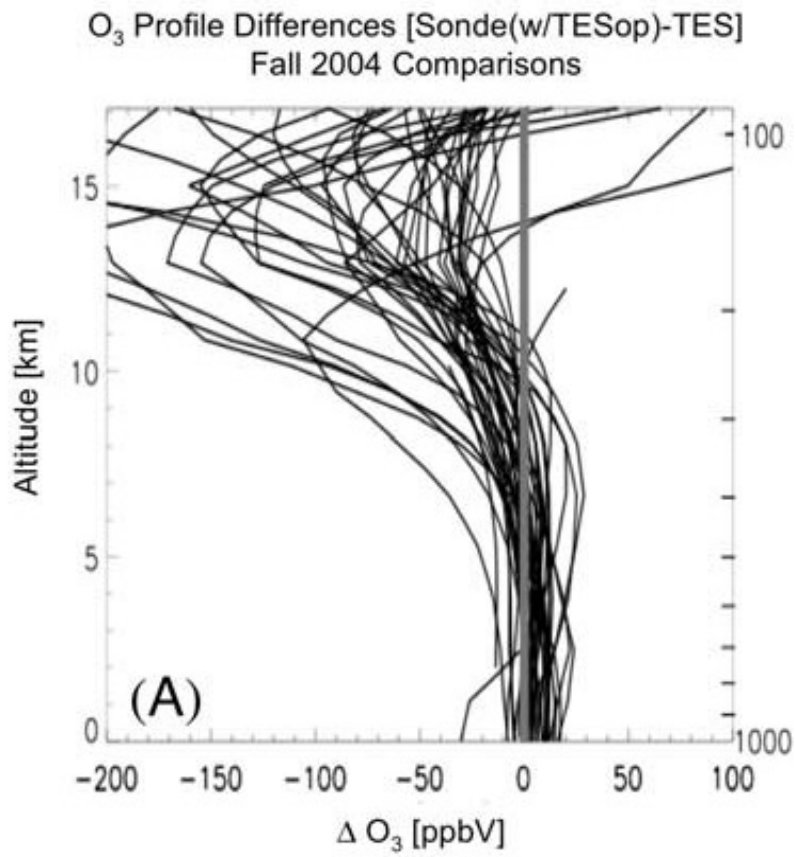

Figure 5-1 TES-sonde absolute differences for 44 comparisons using TES V001 (cases passing the more selective criteria) with ozone (Worden et al., 2007).

In all six latitude zones, Figure 5-2 shows an overall positive bias in the TES V004 O_3 retrievals, compared to the ozonesondes. This positive bias is more apparent in the mean O_3 percent and absolute difference profiles. Overall, both the mean percent and absolute bias plots range from 0-25% for the troposphere. Figure 5-2 also shows that the absolute value of the O_3 difference and bias generally increase near the tropopause and in the lower stratosphere. Similar to comparison of TES V004 with ozonesondes, Figure 5-3 shows that there is a positive bias in the TES measurements relative to the sondes for TES V002 O_3. The mean bias generally ranges from 0 to 15% for the troposphere, compared to a range of 0 to 25% for TES V004. Similar to TES V004, the absolute value of the bias and standard deviation generally increase near the tropopause and in the lower stratosphere, but this translates to a small percent difference as ozone levels are higher there. In the southern low- and midlatitudes, tropics, and northern subtropics the mean bias exceeds 20% in the lower-to-mid troposphere. In these latitude zones, especially the northern midlatitudes, both the mean and standard deviation at low attitudes are inflated by a few large outliers that have been left in for comparison. These outliers represent about 3–4 % of all unflagged profiles in these latitude zones; in other words, the large outliers shown in Figure 5-1 represent 3–4% of all individual profiles (or 3–4% of 5000 coincidence measurements). Figure 5-2 and Figure 5-3 show additional similarities in terms of outliers inflating mean biases of the tropics and subtropics, which exceeds 20%. These outliers also represent only 1–2% of all unflagged profiles, similar to the TES V004 comparisons. The only minor difference is that this

inflation by outliers is also expressed in the southern low- and midlatitudes of the TES V004 comparisons. Similarly to TES V004, these anomalous profiles occur over both land and ocean, and do not appear to be related to the absolute level of ozone. Overall, both the Arctic and Antarctic for TES V004-ozonesonde comparisons exhibit a positive percent bias and almost no variation in the absolute bias as a function of altitude. For TES V004-ozonesonde comparisons the only real exception to the general positive bias was from 20 to 70 hPa at the Arctic and Antarctic; these exceptions display a negative bias from 0 to -10%. For TES V002, almost no percent bias is observed for the Arctic, while a positive bias is observed for the Antarctic's percent bias; nearly no variation with altitude is observed the absolute bias for both regions. For TES V002-ozonesonde comparisons the region from about 70–300 hPa in the southern low and midlatitudes is the only real exception to the general positive bias. It appears that TES V004 shows an improvement in characterizing high latitude ozone levels and the surface brightness temperatures. Ozone levels in the high latitude regions are low and the brightness temperature at the surface is very low, resulting in low sensitivity, which in turn, causes the TES retrieval to revert back to the a priori. Figure 5-2 and Figure 5-3 give a good overview of the variability and percent and absolute biases in TES profiles. Yet, given the overwhelming similarity between Figure 5-2 and Figure 5-3 (i.e., the TES V002- and 3-ozonesonde comparisons in the six latitude bins) and that there are approximately 2 degrees of freedom for signal in the troposphere, we expect a similar quantitative representation for TES V004 versus sonde correlations in the UT and LT for the six latitude zones (specifically, the bias of the mean, the standard deviation or root-mean-square error, and the correlation coefficient).

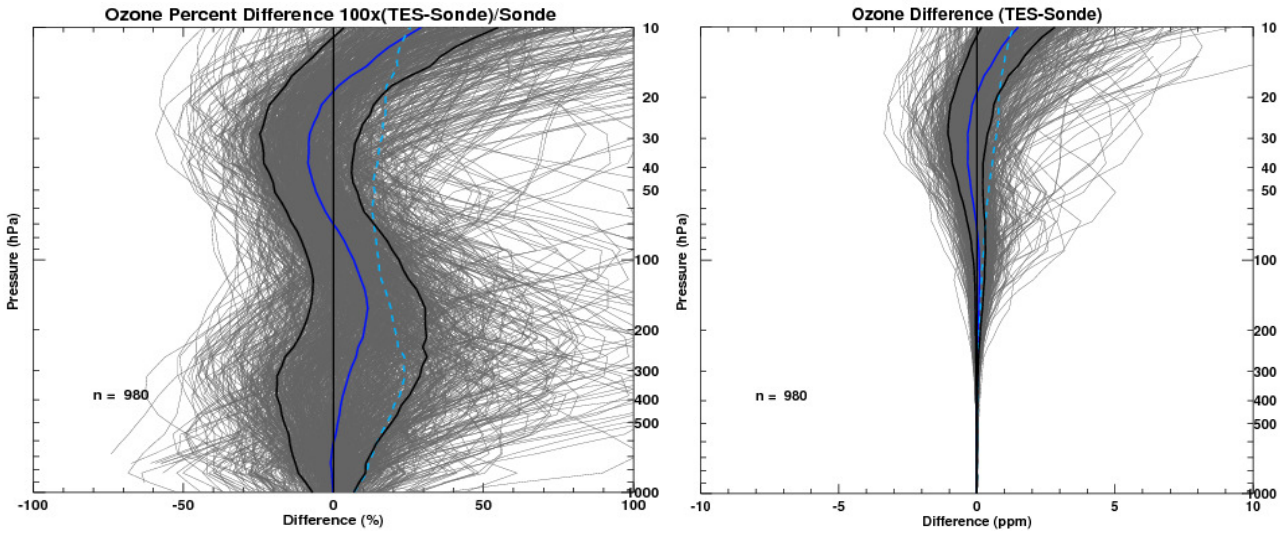

(A: Arctic)

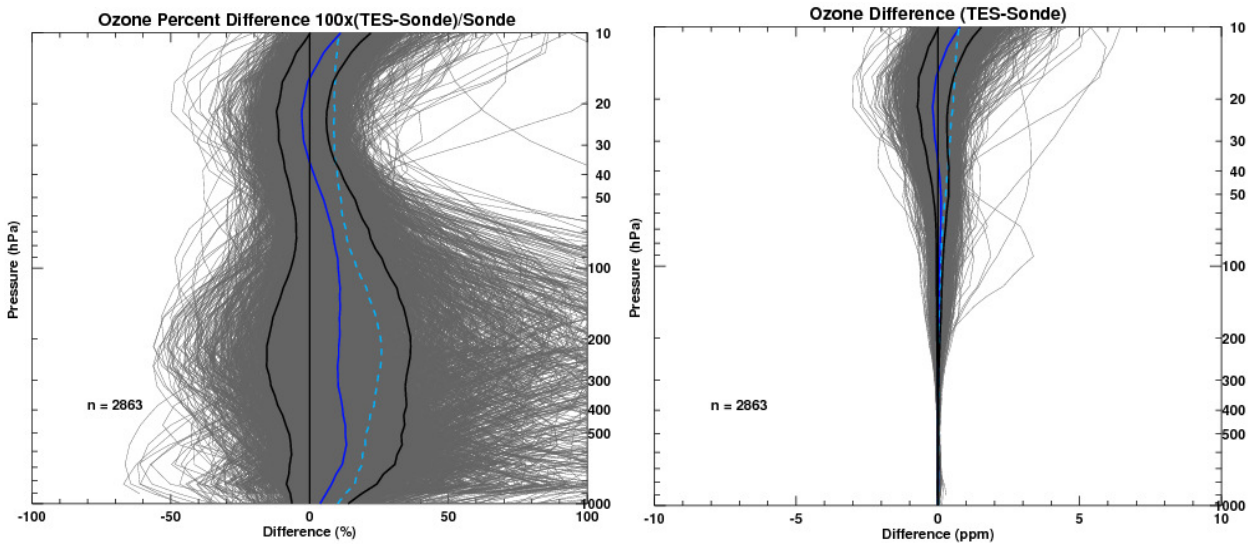

(B: Northern Midlatitudes)

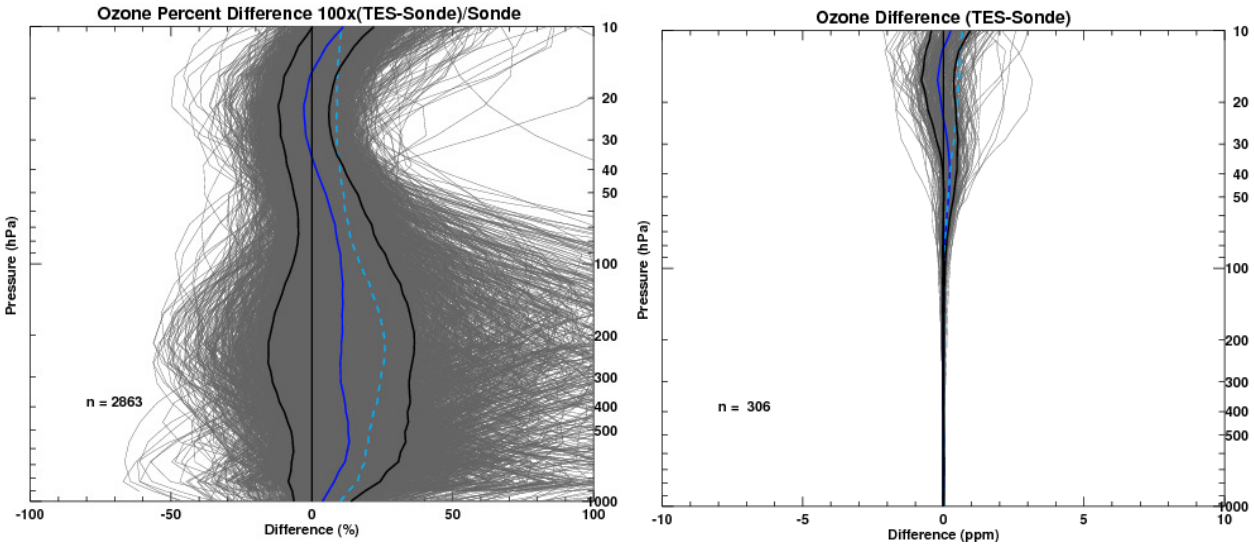

(C: Northern Subtropics)

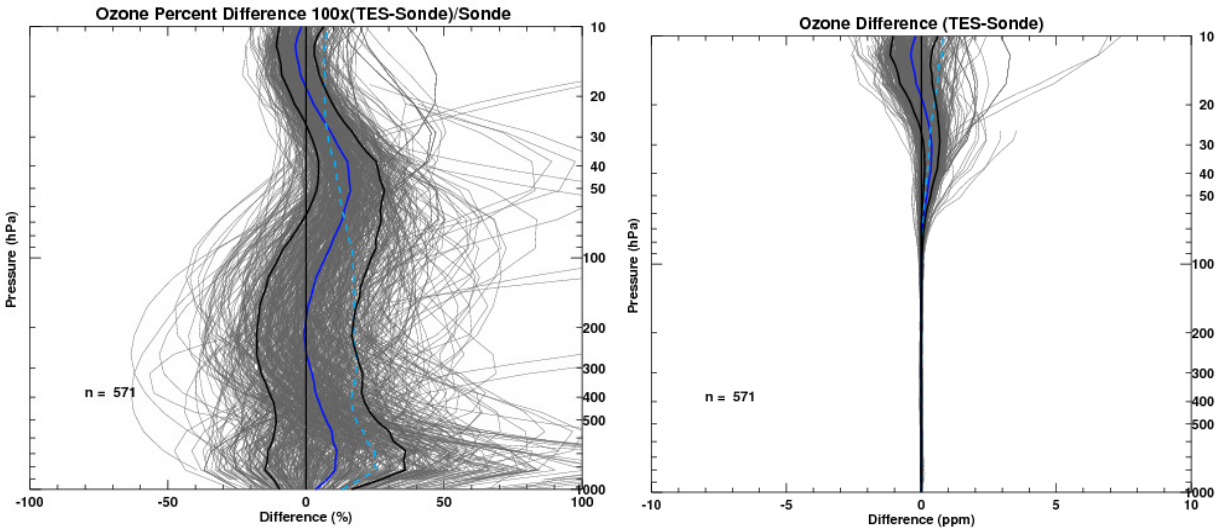

(D: Tropics)

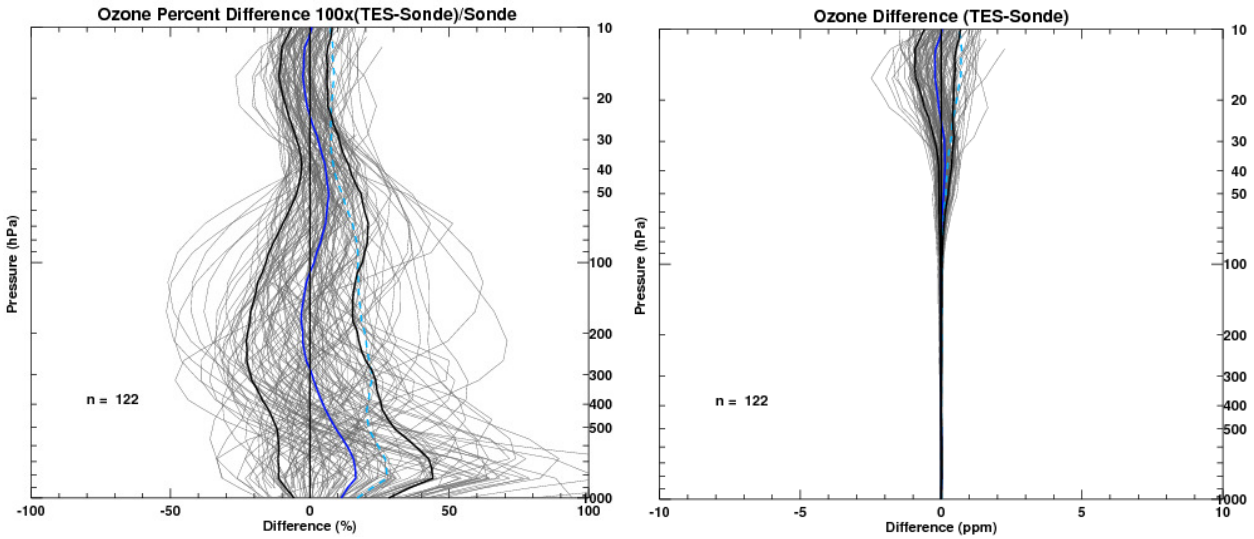

(E: Southern low- and midlatitudes)

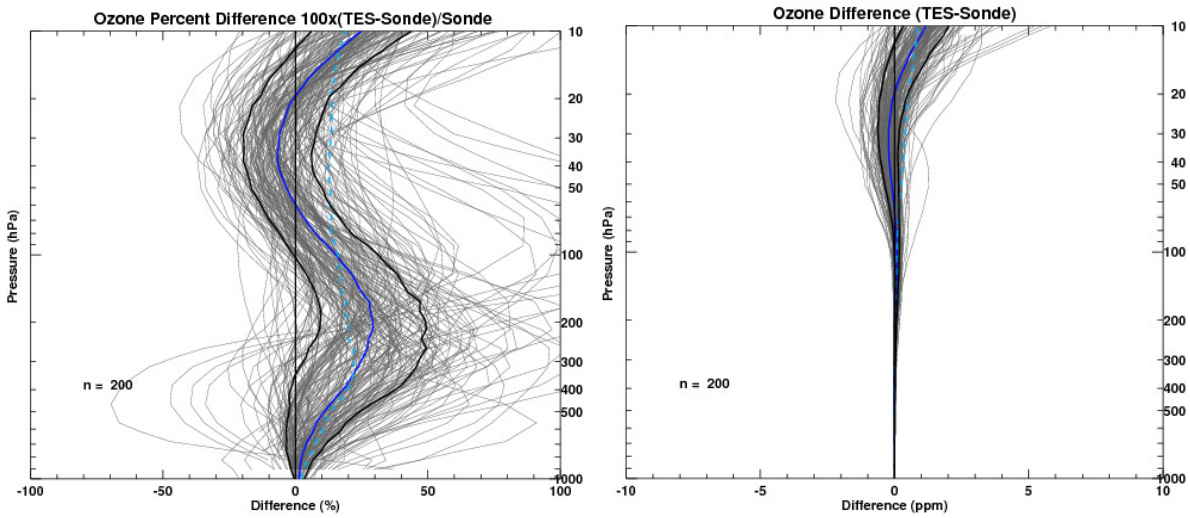

(F: Antarctic)

Figure 5-2 TES-sonde percent differences and absolute differences in six latitude zones. Individual profiles are shown in gray, mean and one standard deviation ranges are overlaid in dark blue and broken light-blue, respectively. Mean minus one standard deviation and mean plus one standard deviation ranges are overlaid in black. The number of coincident comparisons is "n." This Figure illustrates comparisons using TES V004. (A: Arctic, B: Northern Midlatitudes, C: Northern Subtropics, D: Tropics, E: Southern low- and midlatitudes, and F: Antarctic)

TES V003 and V004 nadir stare ozone profiles were also compared with ozonesonde profiles from ARCIONS during ARCTAS, SHADOZ, and the TOPP (Boxe et al., 2010). The ozonesonde data are from launches timed to match Aura's overpass, where 22 coincidences spanned 5° S to 71° N (Barrow, Alaska) from April 2008 to October 2009. Using the TES "stare" observation mode, 32 observations are taken over each coincident ozonesonde launch within about 2 minutes. By effectively sampling the same air mass 32 times, the observed variability can be attributed almost entirely to the random errors of the TES retrievals, thus allowing for the *first* time comparisons to be made between the empirically-calculated random errors to the expected random errors from measurement noise, temperature, and interfering species, such as water. This is primarily due to the fact that TES instrument pointed to the location of each sonde launch, thus greatly reducing the temporal/spatial mismatch. Figure 5-4 (a) and (b) and Figure 5-5 (a) and (b) show comparisons for TES V003 and V004 with ozonesondes for Barrow, Alaska and Egbert, Ontario during 2008 spring and summer of ARCTAS. Figure 5-6 and Figure 5-7 illustrate TES V004-ozonesonde comparisons for Natal, Brazil in January, 2009 and Houston, Texas in August, 2009, respectively. Figure 5-4 through Figure 5-7 all show comparable congruence between the O_3 a priori profile, the mean TES O_3 profile, the sonde O_3 profile, and the profile representing the sonde with the TES-Operator applied, which are all in agreement with previous validation studies. These figures also illustrate, via the averaging kernel as a function of pressure, that TES has sensitivity to LT O_3, especially for cloud-free scenes. Overall, for all 22 coincident measurements, a positive bias (by less than 15%) is observed from the surface to the UT and a negative bias (less than 20%) is observed from the UT to the LS. Lastly, we find that the calculated errors are consistent with the actual errors with a similar vertical distribution, varying between 5 and 20% for TES V003 and V004 ozone data.

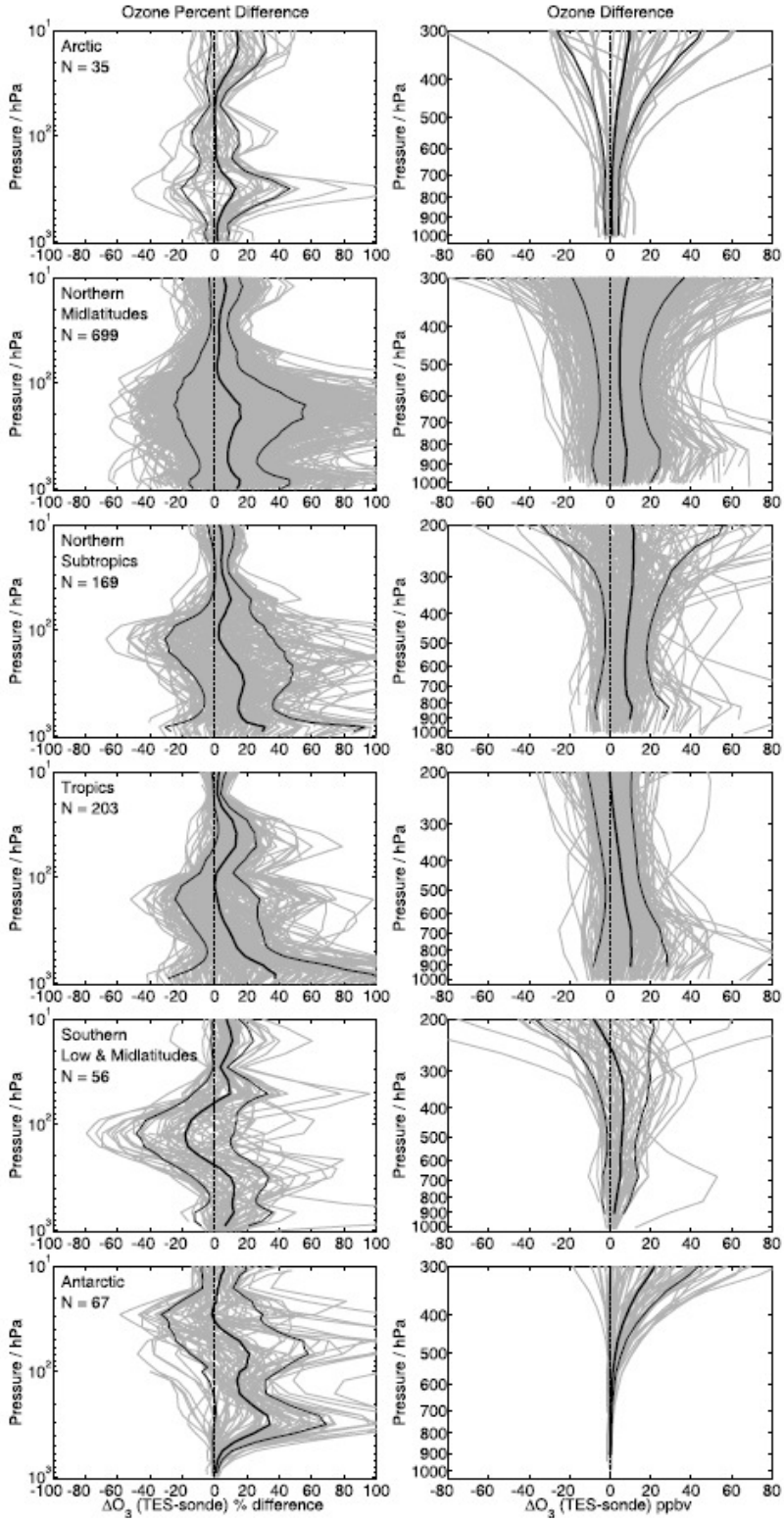

Figure 5-3 TES-sonde ozone percent differences and absolute differences in six latitude zones. Individual profiles are shown in gray, and the mean and 1 standard deviation range are overlaid in black. *N* is the number of profiles plotted after removing cloudy scenes and flagged TES data. This study illustrates comparisons using TES V002.

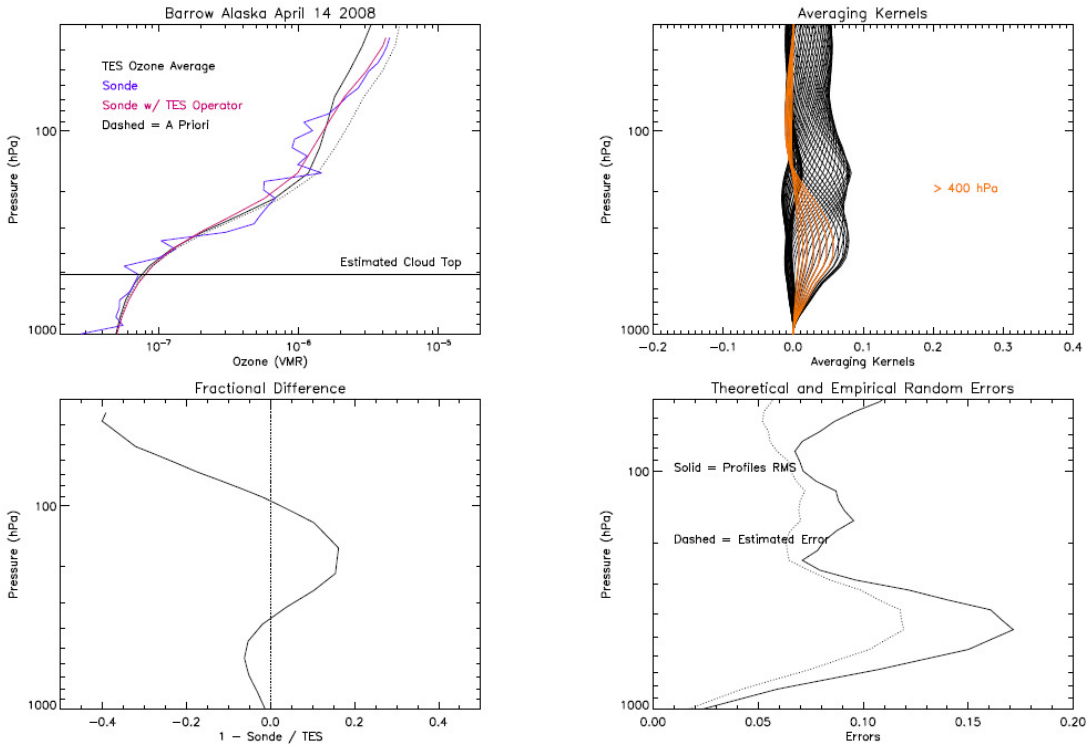

5-4(a) V003

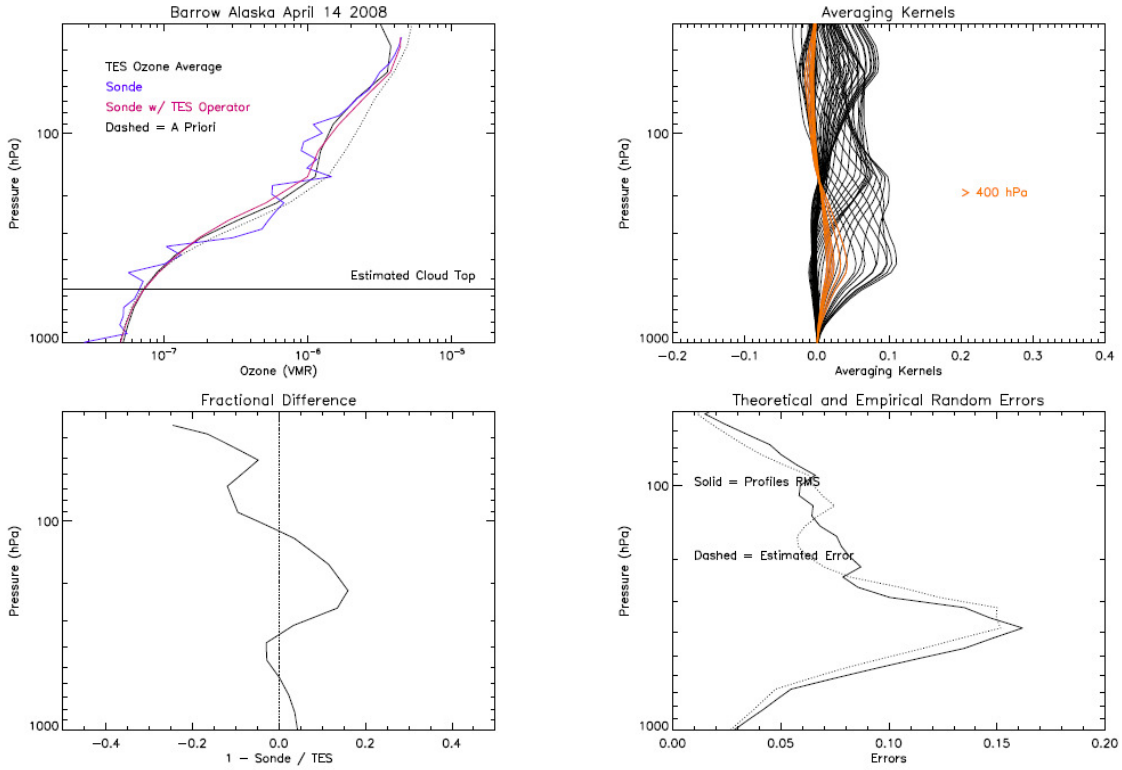

5-4(b) V004

Figure 5-4 The TES-stare sequence on April 14th, 2008 over Barrow, Alaska, started at 21:45 (UTC), and the ozonesonde on that day at Barrow was launched at 22:13 (UTC), using V003 (a) and V004 (b) TES data.

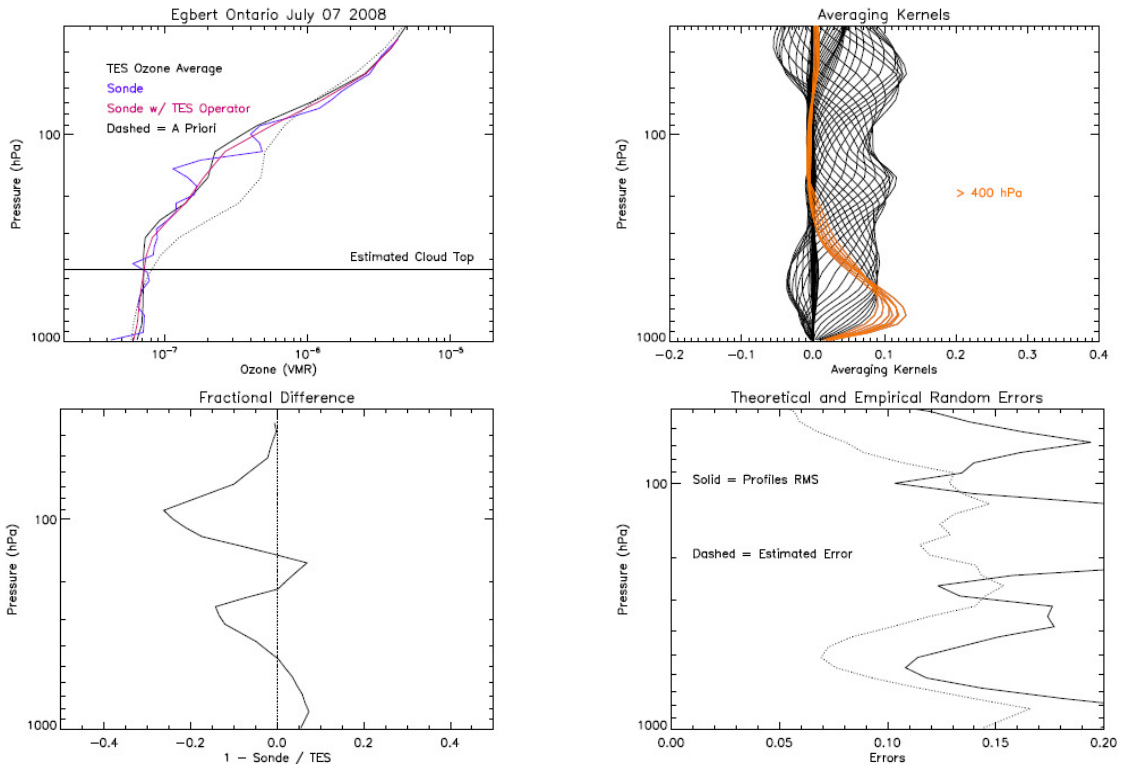

5-5(a) V003

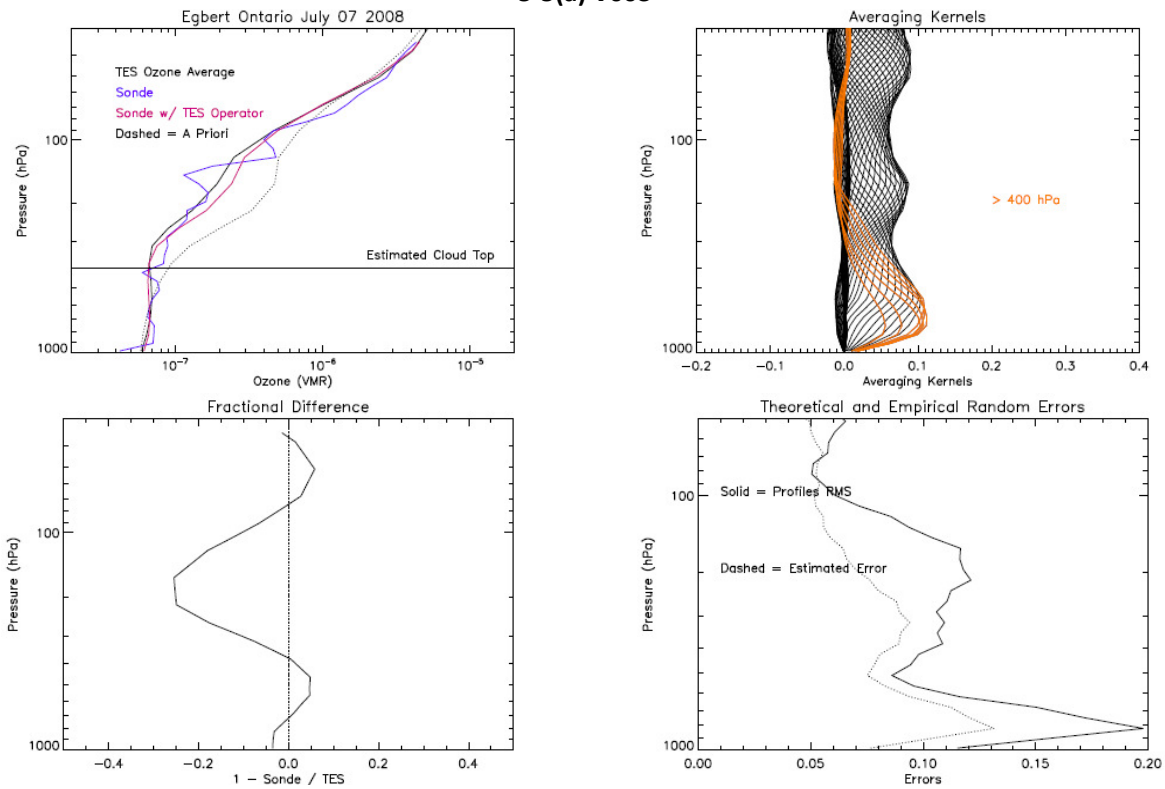

5-5(b) V004

Figure 5-5 The TES-stare sequence on July 5th, 2008 over Egbert, Ontario, started at 17:58 (UTC), and the ozonesonde on that day at Egbert was launched at 18:25 (UTC), using V003 (a) and V004 (b) TES data.

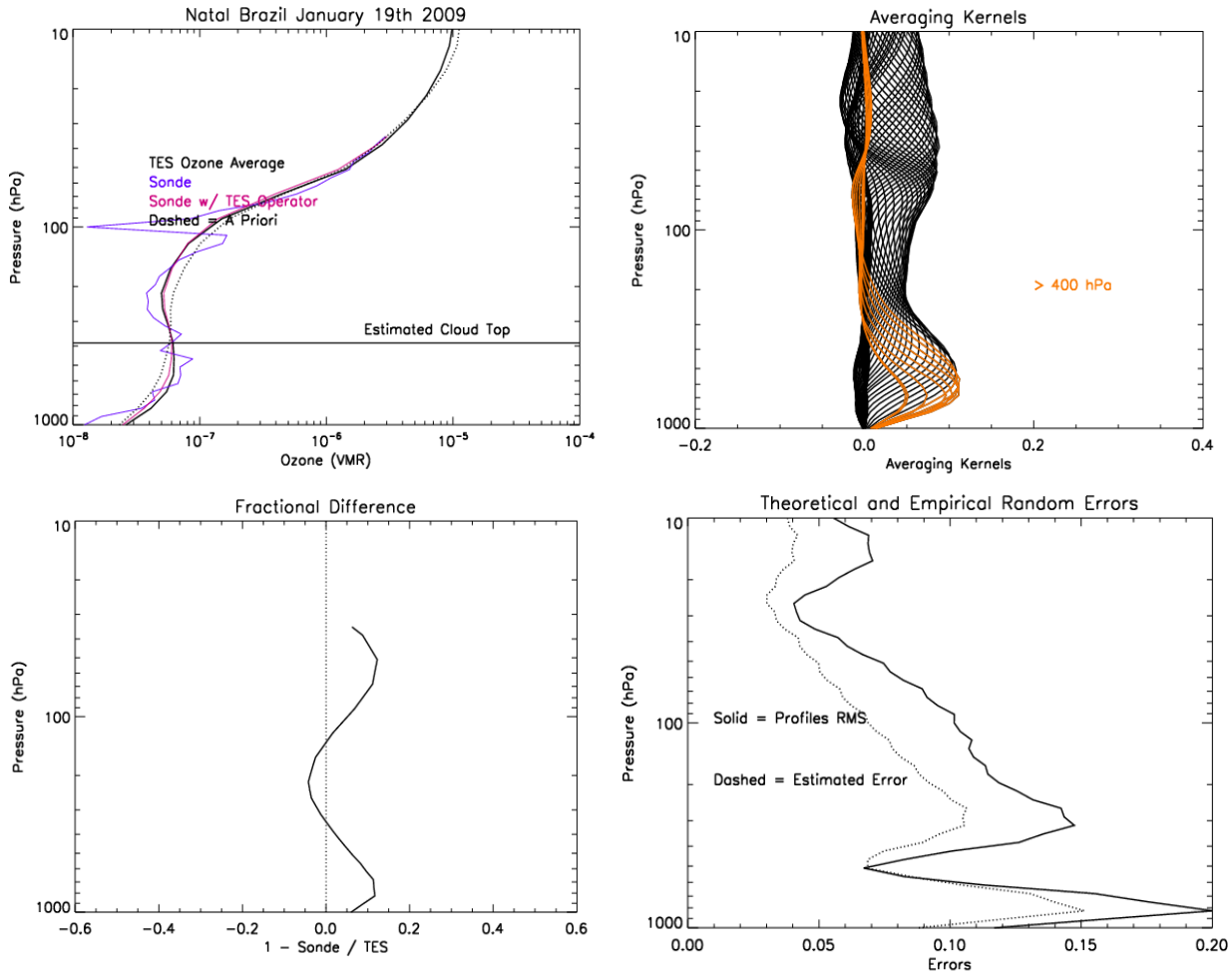

Figure 5-6 The TES-stare sequence on January 19th, 2009 over Natal, Brazil, started at 16:08 (UTC), and the ozonesonde on that day at Egbert was launched at 15:50 (UTC), using and V004 TES data.

Nassar et al. (2008) also investigated the seasonal variability of TES V002 ozone since there were a sufficient number of coincidences (totaling 700 from 35 to 56° N latitude) in the northern midlatitudes. Percent and absolute difference profiles are shown for winter, spring, summer, and fall (Figure 5-8). The altitude of the peak in the mean percent difference profiles was lowest in the winter and highest in the summer, which likely relates to the changing tropopause height and variability of ozone (Logan, 1999); still, the altitude at which the mean percent difference peaks for the winter and summer are not significantly higher or lower compared to the spring and fall. The seasonal division also shows that the low altitudes outliers predominantly occur in the summer and to a lesser degree in the spring and that the summer northern midlatitude bias profiles somewhat resemble the northern subtropics or the tropics in the upper troposphere. With the exception of a small negative bias at ~ 90 to 100 hPa in the summer for V002 mean ozone percent difference, the mean O_3 percent and absolute differences generally show a positive bias for all seasons. Overall, these findings are in agreement with Boxe et al. (2010), which shows a positive bias in TES V004 O_3 (by less than 15%) from the surface to the UT.

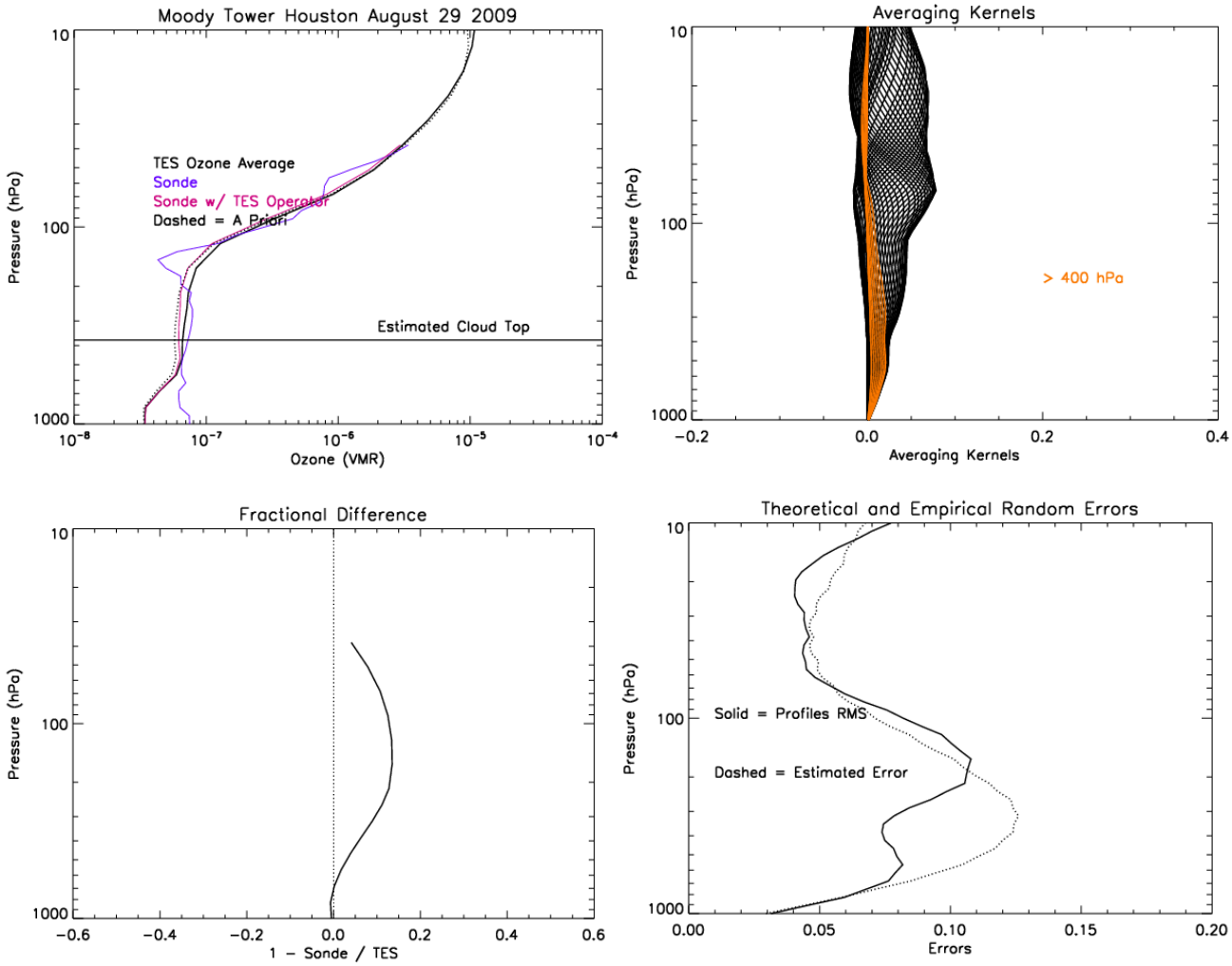

Figure 5-7 The TES-stare sequence on August 29th, 2009 over Moody Tower, Houston, Texas, started at 19:47 (UTC), and the ozonesonde on that day at Egbert was launched at 18:57 (UTC), using and V004 TES data.

Figure 5-9 displays O_3 percent and absolute differences for winter, spring, summer, and fall for TES V004 ozone. These measurements range from 35 to 56° N latitude, with a total of 2863 coincidences, which is a factor of ~ 4 larger than Nassar et al. (2008). Figure 5-9, representative of a statistically-greater data set, shows several improvements when compared to Nassar et al. (2008) and Boxe et al. (2010) comparisons of TES V002, V003, and V004 ozone with ozonesondes. The mean O_3 percent difference profiles produced in Figure 5-9 show a positive bias less than 15%, which is an improvement compared to Nassar et al. (2008); in addition, Figure 5-9 shows that the mean O_3 percent differences exhibit a small negative bias, less than about 5%. Both these features are consistent with that of Boxe et al. (2010). The absolute mean percent differences for all seasons for mid-to-lower tropospheric ozone also show an improvement when compared to Nassar et al. (2008).

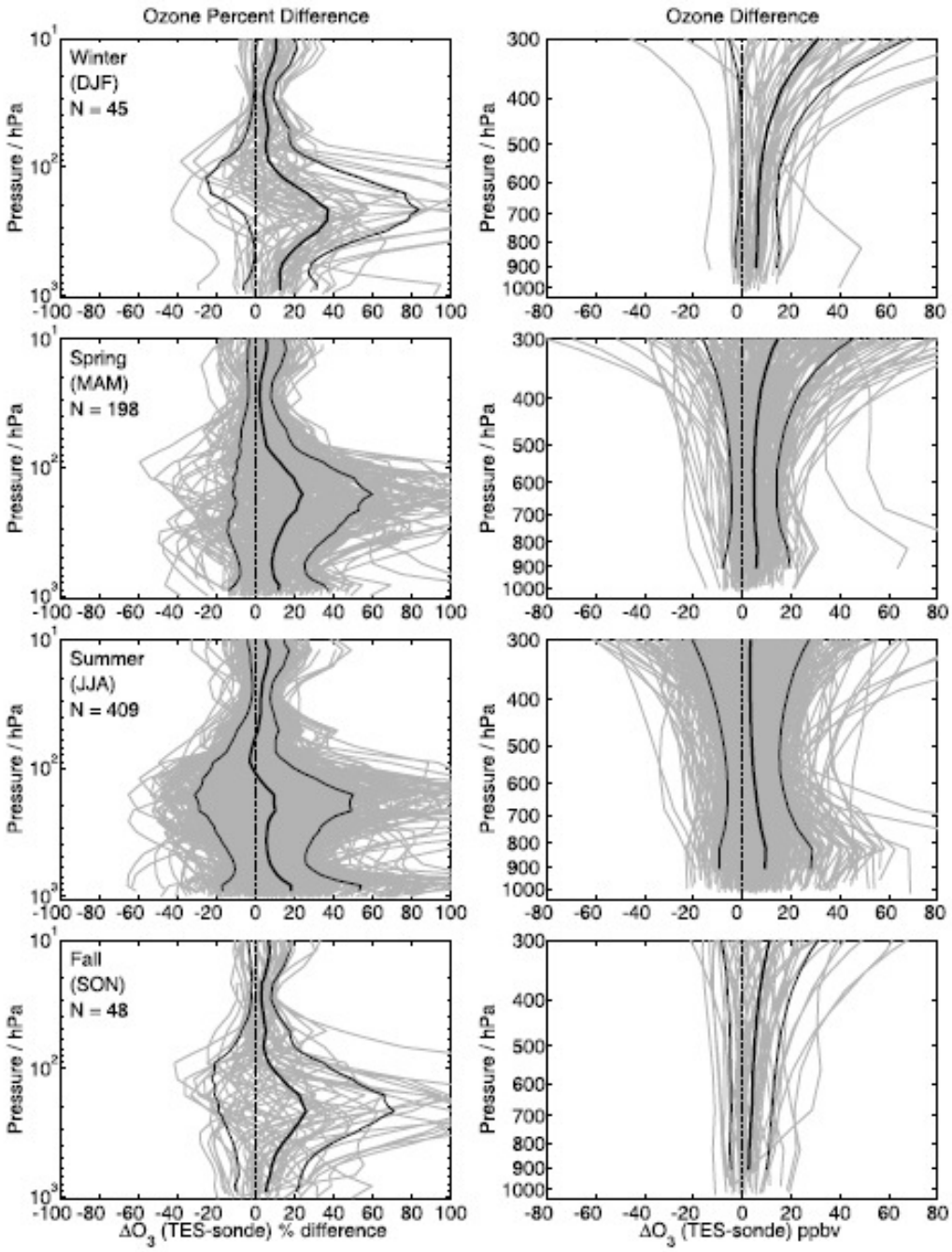

Figure 5-8 TES-sonde ozone percent differences and absolute differences (for TES V002) for the four seasons (months abbreviated in parentheses) in the northern midlatitudes (35 to 56° N). Individual profiles are shown in gray, and the mean and 1 standard deviation range are overlaid in black. *N* is the number of profiles plotted after removing cloudy scenes and flagged TES data. (Nassar et al. 2008).

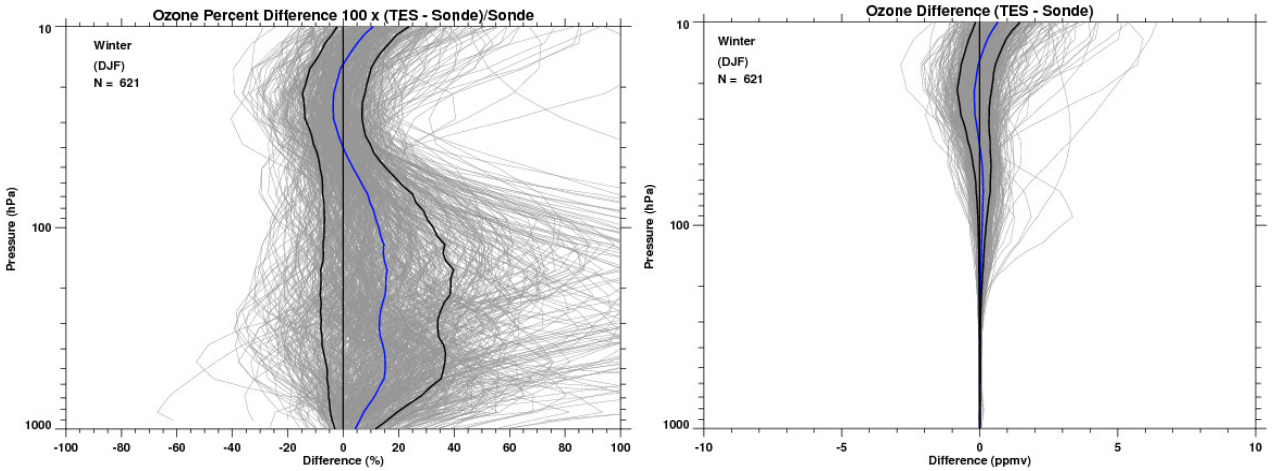

Winter

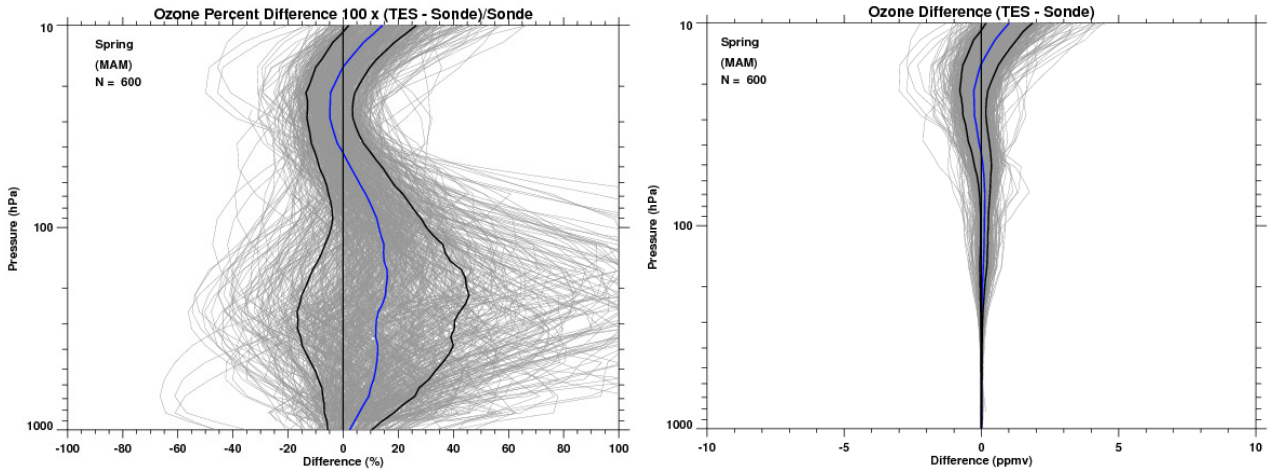

Spring

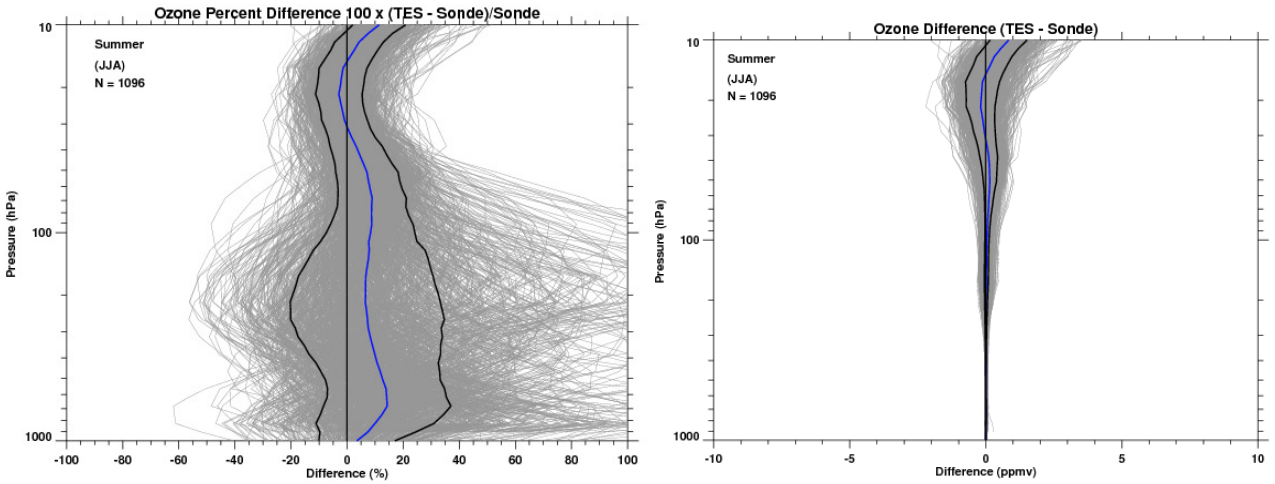

Summer

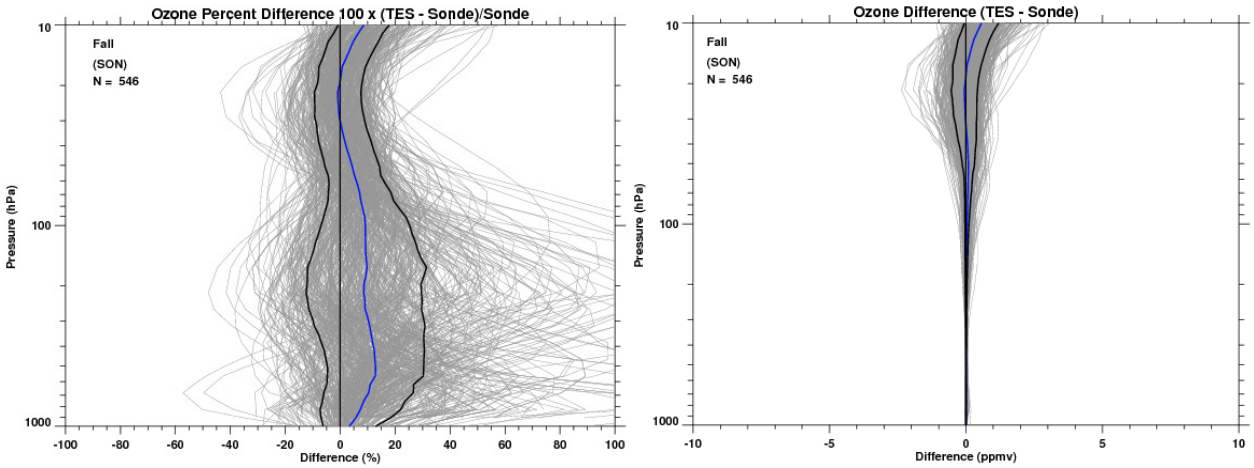

Fall

Figure 5-9 TES-sonde ozone percent differences and absolute differences (for TES V004) for the four seasons (months abbreviated in parentheses) in the northern midlatitudes (35 to 56° N). Individual profiles are shown in gray, mean and one standard deviation ranges are overlaid in dark blue and broken light-blue, respectively. Mean minus one standard deviation and mean plus one standard deviation ranges are overlaid in black. The number of coincident comparisons is "n." This Figure illustrates comparisons using TES V004.

5.3 References

5.3.1 Primary TES Nadir Ozone References

[1] Boxe, C.S., Worden, J.R., Bowman, K.W., Kulawik, S.S., Neu, J.L., Ford, W.C., Osterman, G.B., Herman, R. L., Eldering, A., Tarasick, D.W., Thompson, A.M., Doughty, D.C., Hoffmann, M.R., and Oltmans, S.J., Validation of northern latitude Tropospheric Emission Spectrometer stare ozone profiles with ARC-IONS sondes during ARCTAS: sensitivity, bias and error analysis, *Atmospheric Chemistry and Physics*, doi:10.5194/acp-10-9901-2010, October 20, 2010.

[2] Nassar, R., J. A. Logan, H. M. Worden, I. A. Megretskaia, K. W. Bowman, G. B. Osterman, A. M. Thompson, D. W. Tarasick, S. Austin, H. Claude, M. K. Dubey, W. K. Hocking, B. J. Johnson, E. Joseph, J. Merrill, G. A. Morris, M. Newchurch, S. J. Oltmans, F. Posny, F. J. Schmidlin, H. Vömel, D. N. Whiteman, and J. C. Witte (2008), Validation of Tropospheric Emission Spectrometer (TES) Nadir Ozone Profiles Using Ozonesonde Measurements, *J. Geophys. Res. 113*, D15S17, (doi:10.1029/2007JD008819), May 7, 2008.

[3] Osterman, G., S. S. Kulawik, H. M. Worden, N. A. D. Richards, B. M. Fisher, A. Eldering, M. W. Shephard, L. Froidevaux, G. Labow, M. Luo, R. L. Herman, K. W. Bowman, and A. M. Thompson, Validation of Tropospheric Emission Spectrometer (TES) Measurements of the Total, Stratospheric and Tropospheric Column Abundance of Ozone, *J. Geophys. Res., 113*, D15S16, (doi:10.1029/2007JD008801) May 7, 2008.

[4] Richards, N. A. D., G. B. Osterman, E. V. Browell, J. W. Hair, M. Avery and Q. Li, Validation of Tropospheric Emission Spectrometer ozone profiles with aircraft

observations during the Intercontinental Chemical Transport Experiment–B, *J. Geophys. Res., 113*, D16S29, (doi:10.1029/2007JD008815) May 23, 2008.

[5] Worden, H. M., J. Logan, J. R. Worden, R. Beer, K. Bowman, S. A. Clough, A. Eldering, B. M. Fisher, M. R. Gunson, R. L. Herman, S. S. Kulawik, M. C. Lampel, M. Luo, I. A. Megretskaia, G. B. Osterman, and M. W. Shephard (2007), Comparisons of Tropospheric Emission Spectrometer (TES) ozone profiles to ozonesondes: Methods and initial results, *J. Geophys. Res., 112*, D03309, (doi:10.1029/2006JD007258), February 15, 2007.

[6] Worden, J., X. Liu, K. Bowman, K. Chance, R. Beer, A. Eldering, M. Gunson, and H. Worden, (2007), Improved Tropospheric Ozone Profile Retrievals Using OMI and TES Radiances, *Geophys. Res. Lett., 34,* L01809, (doi:10.1029/2006GL027806) January 10, 2007.

5.3.2 TES References

[7] Beer, R., T. A. Glavich, D. M. Rider (2001), Tropospheric Emission Spectrometer for the Earth Observing System's Aura satellite, *Applied. Optics, 40 (15),* 2356-2367, May 20, 2001.

[8] Beer, R. (2006), TES on the Aura Mission: Scientific Objectives, Measurements and Analysis Overview, *IEEE Transactions on Geoscience and Remote Sensing, 44 (No.5),* 1102-1105, May 2006.

[9] Bowman K.W., C. D. Rodgers, S. S. Kulawik, J. Worden, E. Sarkissian, G. Osterman, T. Steck, M. Lou, A. Eldering, M. Shepherd, H. Worden, M. Lampel, S. Clough, P. Brown, C. Rinsland, M. Gunson, R. Beer, "Tropospheric Emission Spectrometer: Retrieval Method and Error Analysis", *IEEE Trans. Geoscience and Remote Sensing, 44, (No.5),* 1297-1307. May 2006.

[10] Eldering, A., S. S. Kulawik, J. Worden, K. Bowman, G. Osterman (2008), Implementation of cloud retrievals for TES Atmospheric retrievals: 2. Characterization of cloud top pressure and effective optical depth retrievals, *Journal of Geophysical Research, Vol. 113,* D16S37, (doi:10.1029/2007JD008858) June 10, 2008.

[11] Jourdain, L., H. M. Worden, J. R. Worden, K. Bowman, Q. Li, A. Eldering, S. S. Kulawik, G. Osterman, K. F. Boersma, B. Fisher, C. P. Rinsland, R. Beer, M. Gunson,. (2007), Tropospheric vertical distribution of tropical Atlantic ozone observed by TES during the northern African biomass burning season, *Geophysical Research Letters, 34*, L04810, (doi:10.1029/2006GL028284) February 23, 2007.

[12] Kulawik, S. S., J. Worden, A. Eldering, K. Bowman, M. Gunson, G. B. Osterman, L. Zhang, S. Clough, M. W. Shephard, R. Beer (2006), Implementation of cloud retrievals for Tropospheric Emission Spectrometer (TES) atmospheric retrievals: part 1. Description and characterization of errors on trace gas retrievals, *J. Geophys. Res., 111*, D24204, (doi:10.1029/2005JD006733), December 22, 2006.

[13] Luo M., C. P. Rinsland, C. D. Rodgers, J. A. Logan, H. Worden, S. Kulawik, A. Eldering, A. Goldman, M. W. Shephard, M. Gunson, and M. Lampel (2007) Comparison of carbon monoxide measurements by TES and MOPITT: Influence of a

priori data and instrument characteristics on nadir atmospheric species retrievals, *Journal of Geophysical Research, Vol. 112*, D09303, (doi:101029/2006JD007663) May 3, 2007.

[14] Osterman, G., (editor), K. Bowman, A. Eldering, B. Fisher, R. Herman, D. Jacob, L. Jourdain, S. Kulawik, M. Luo, R. Monarrez, G. Osterman, S. Paradise, V. Payne, S. Poosti, N. Richards, D. Rider, D. Shepard, M. Shephard, F. Vilnrotter, H. Worden, J. Worden, H. Yun and L. Zhang (2009), Earth Observing System (EOS) Tropospheric Emission Spectrometer (TES) Level 2 (L2) Data User's Guide (Up to & including Version 4 data), Version 4.0, JPL Internal Report D-38042, May 20, 2009.

[15] Worden, J., S. S. Kulawik, M. W. Shephard, S. A. Clough, H. Worden, K. Bowman, and A. Goldman (2004), Predicted errors of tropospheric emission spectrometer nadir retrievals from spectral window selection, *J. Geophys. Res., 109*, D09308, May 15, 2004.

5.3.3 General References

[16] Bloom, S., A. da Silva, D. Dee, M. Bosilovich, J.-D. Chern, S. Pawson, S. Schubert, M. Sienkiewicz, I. Stajner, W.-W. Tan, M.-L. Wu (2005). Documentation and Validation of the Goddard Earth Observing System (GEOS) Data Assimilation System - Version 4. *Technical Report Series on Global Modeling and Data Assimilation 104606, Vol. 26,* 187 pages, April 2005. Available from (paste entire link including pdf into browser):

http://ntrs.nasa.gov/archive/nasa/casi.ntrs.nasa.gov/20050175690_2005173043.pdf

[17] Brasseur, G. P., D. A. Hauglustaine, S. Walters, R. J. Rasch, J.-F. Müller, C. Granier, and X. X. Tie (1998), MOZART, a global chemical transport model for ozone and related chemical tracers 1. Model description, *J. Geophys. Res.*, *103* (D21), 28, 265–28, 289 (1998).

[18] Draxler, R.R. and Rolph, G.D. (2003), HYSPLIT (HYbrid Single-Particle Lagrangian Integrated Trajectory) Model access via NOAA ARL READY Website (http://www.arl.noaa.gov/ready/hysplit4.html). NOAA Air Resources Laboratory, Silver Spring, MD (2003).

[19] Froidevaux, L., Y.B. Jiang, A. Lambert, N.J. Livesey, W.G. Read, J.W. Waters, E.V. Browell, J.W. Hair, M.A. Avery, T.J. McGee, L.W. Twigg, G.K. Sumnicht, K.W. Jucks, J.J. Margitan, B. Sen, R.A. Stachnik, G.C. Toon, P.F. Bernath, C.D. Boone, K.A. Walker, M.J. Filipiak, R.S. Harwood, R.A. Fuller, G.L. Manney, M.J. Schwartz, W.H. Daffer, B.J. Drouin, R.E. Cofield, D.T. Cuddy, R.F. Jarnot, B.W. Knosp, V.S. Perun, W.V. Snyder, P.C. Stek, R.P. Thurstans, P.A. Wagner (2008), Validation of Aura Microwave Limb Sounder stratospheric ozone measurements, *J. Geophys. Res., 113,* D15S20, (doi:10.1029/2007JD008771) 2008.

[20] Jiang, Y. B., L. Froidevaux, A. Lambert, N.J. Livesey, W.G. Read, J.W. Waters, B. Bojkov, T. Leblanc, I.S. McDermid, S. Godin-Beekmann, M.J. Filipiak, R.S. Harwood, R.A. Fuller, W.H. Daffer, B.J. Drouin, R.E. Cofield, D.T. Cuddy, R.F. Jarnot, B.W. Knosp, V.S. Perun, M.J. Schwartz, W.V. Snyder, P.C. Stek, R.P. Thurstans, P.A. Wagner, M. Allaart, S.B. Andersen, G. Bodeker, B. Calpini, H. Claude, G. Coetzee, J. Davies, H. De Backer, H. Dier, M. Fujiwara, B. Johnson, H. Kelder, N.P. Leme, G.

Konig-Langlo, E. Kyro, G. Laneve, L.S. Fook, J. Merrill, G. Morris, M. Newchurch, S. Oltmans, M.C. Parrondos, F. Posny, F. Schmidlin, P. Skrivankova, R. Stubi, D. Tarasick, A. Thompson, V. Thouret, P. Viatte, H. Vomel, P. von der Gathen, M. Yela, G. Zablocki (2007), Validation of Aura Microwave Limb Sounder Ozone by Ozonesonde and Lidar Measurements, *Journal of Geophysical Research, 112,* D24S34, (doi:10.1029/2007JD008776) 2007.

[21] Levelt, P. F., G.H.J. van den Oord, M.R. Dobber, A. Mälkki, H. Visser, J. de Vries, P. Stammes, J. Lundell and H. Saari (2006a), The Ozone Monitoring Instrument, *IEEE Trans. Geoscience and Remote Sensing, 44, (No.5),* 1093-1101, May 2006.

[22] Levelt, P. F., E. Hilsenrath, G.W. Leppelmeier, G.H.J. van den Oord, P.K. Bhartia, J. Tamminen, J.F. de Haan en J.P. Veefkind (2006b), Science objectives of the Ozone monitoring instrument, *IEEE Trans. Geoscience and Remote Sensing, 44, (No.5),*1199-1208, May 2006.

[23] Livesey, N. J., W.G. Read, A. Lambert, R.E. Cofield, D. T. Cuddy, L. Froidevaux, R. A. Fuller, R. F. Jarnot, J. H. Jiang, Y. B. Jiang, B. W. Knosp, L. J. Kovalenko, H. M. Pickett, H. C. Pumphrey, M. L. Santee, M. J. Schwartz, P. C. Stek, P. A. Wagner, J. W. Waters, and D. L. Wu (2007), EOS MLS Version 2.2 Level 2 data quality and description document, Version 2.2x-1.0a Jet Propulsion Laboratory Internal Report D-33509, May 22, 2007.

[24] Livesey N.J., M.J. Filipiak, L. Froidevaux, W.G. Read, A. Lambert, M.L. Santee, J.H. Jiang, H.C. Pumphrey, J.W. Waters, R.E. Cofield, D.T. Cuddy, W.H. Daffer, B.J. Drouin, R.A. Fuller, R.F. Jarnot, Y.B. Jiang, B.W. Knosp, Q.B. Li, V.S. Perun, M.J. Schwartz, W.V. Snyder, P.C. Stek, R.P. Thurstans, P.A. Wagner, M. Avery, E.V. Browell, J-P. Cammas, L.E. Christensen, G.S. Diskin, R-S. Gao, H-J. Jost, M. Loewenstein, J.D. Lopez, P. Nedelec, G.B. Osterman, G.W. Sachse, and C.R. Webster (2008), Validation of Aura Microwave Limb Sounder O3 and CO observations in the upper troposphere and lower stratosphere, *J. Geophys. Res., 113*, D15S02, (doi:10.1029/2007JD008805) March 27, 2008.

[25] Logan, J.A., An analysis of ozonesonde data for the troposphere: Recommendations for testing 3-D models, and development of a gridded climatology for tropospheric ozone*, J. Geophys. Res., 104,* 16115-16149, 1999.

[26] Rodgers, C. D. (2000), *Inverse Methods for Atmospheric Sounding: Theory and Practice.* World Scientific Publishing Co. Ltd., 2000.

[27] Rodgers, C. D. and B. J. Conners (2003), Intercomparison of remote sounding instruments, *J. Geophys. Res., 108,(D3),* 4116, (doi:10.1029/2002JD002299) 2003.

[28] Schoeberl, M.R., J.R. Ziemke, B. Bojkov, N. Livesey, B. Duncan, S. Strahan, L. Froidevaux, S. Kulawik, P.K. Bhartia, S. Chandra, P.F. Levelt, J.C. Witte, A.M. Thompson, E. Cuevas, A. Redondas, D.W. Tarasick, J. Davies, G. Bodeker, G. Hansen, B.J. Johnson, S.J. Oltmans, H. Vomel, M. Allaart, H. Kelder, M. Newchurch, S. Godin-Beekmann, G. Ancellet, H. Claude, S.B. Andersen, E. Kyro, M. Parrondos, M. Yela, G. Zablocki, D. Moore, H. Dier, P. von der Gathen, P. Viatte, R. Stubi, B. Calpini, P. Skrivankova, V. Dorokhov, H. De Backer, F.J. Schmidlin, G. Coetzee, M. Fujiwara, V. Thouret, F. Posny, G. Morris, J. Merrill, C.P. Leong, G. Koenig-Langlo, and E. Joseph.

(2007), A trajectory-based estimate of the tropospheric ozone column using the residual method, *J. Geophys. Res. 112*, D24S49, (doi:10.1029/2007JD008773) December 19, 2007.

[29] Waters, J.W., L. Froidevaux, R.S. Harwood, R.F. Jarnot, H.M. Pickett, W.G. Read, P.H. Siegel, R.E. Cofield, M.J. Filipiak, D.A. Flower, J.R. Holden, G.K. Lau, N.J. Livesey, G.L. Manney, H.C. Pumphrey, M.L. Santee, D.L. Wu, D.T. Cuddy, R.R. Lay, M.S. Loo, V.S. Perun, M.J. Schwartz, P.C. Stek, R.P. Thurstans, M.A. Boyles, S. Chandra, M.C. Chavez, G-S. Chen, B.V. Chudasama, R. Dodge, R.A. Fuller, M.A. Girard, J.H. Jiang, Y. Jiang, B.W. Knosp, R.C. LaBelle, J.C. Lam, K.A. Lee, D. Miller, J.E. Oswald, N.C. Patel, D.M. Pukala, O. Quintero, D.M. Scaff, W.V. Snyder, M.C. Tope, P.A. Wagner, and M.J. Walch, (2006), The Earth Observing System Microwave Limb Sounder (EOS MLS) on the Aura satellite, *IEEE Trans. Geoscience and Remote Sensing, 44, (No.5),* 1075-1092, May 2006.

[30] Ziemke, J.R., S. Chandra, B.N. Duncan, L. Froidevaux, P.K. Bhartia, P.F. Levelt, and J.W. Waters, (2006), Tropospheric ozone determined from Aura OMI and MLS: Evaluation of measurements and comparison with the Global Modeling Initiative's Chemical Transport Model, *J. Geophys. Res., 111,* D19303 (doi:10.1029/2006JD007089) October 5, 2006.

6. Validation of TES Retrievals of Carbon Monoxide

6.1 Overview

All the TES CO data validation activities, including comparisons with in-situ aircraft data, and with MOPITT V003 data, have been carried out for TES V003 or V002 data. In this section we briefly describe that no systematic changes in TES CO V004 data compared to the previous versions are found.

We briefly describe the TES instrument performance over four years on orbit and the effect of the optical bench warm-up conducted early Dec 2005 on filter 1A1 and the CO retrievals. We give an overview of the characterization of TES CO retrievals, including the roles of a priori profiles and the averaging kernels. A brief overview of the global distributions of TES CO measurements is given for different seasons. We present comparisons of TES CO profiles with in situ measurements from several aircraft campaigns, including INTEX-B, AVE, and CR-AVE. Validation of TES CO data using MOPITT measurements, as well as comparisons in the upper troposphere of TES CO data to ACE (Atmospheric Chemistry Experiment) and MLS CO are summarized. These comparisons not only offer good qualitative checks for TES data, *e.g.,* the characteristics of the CO global distribution or the shapes of their vertical profiles, but also offer initial quantitative validations of TES CO retrievals.

6.2 Instrument performance before and after optical bench warm-up

For constant emission source, e.g., on-board black body, the signal strength in TES 1A1 filter (1900-2300cm-1) is not constant over time and the variation of the signal strength is reflected in the CO retrievals. Figure 6-1 displays the normalized integrated spectral magnitude (ISM) (top panel), beam splitter temperature (middle panel), and degree of freedom for signal (DOFS) for latitudes of 30°N-30°S as a function of time (Rinsland et al., 2006). Data after the mid of 2006 stays about the same level. The ISM is a sensitive indicator of the signal levels of the TES detectors and is calculated by integrating a spectrum over wavenumber. It is the primary quantity used to quantify and detect trends in the TES instrument alignment and performance. An overall trend of declining ISM with time and the measured beamsplitter temperature is apparent, with increases in beamsplitter temperatures when the detectors are de-iced periodically. The warming of the TES optical bench on Nov 29-Dec 2, 2005 improved the TES beamsplitter alignment, with an integrated spectral magnitude increase for the 1A1 filter by a factor of 3.4 as compared to the pre-warm up value.

The TES CO retrieval 'sensitivity', or the parameters describing the retrieval vertical information in the troposphere, e.g., the Degree of Freedom for signal (DOF) and the retrieval errors, are much improved after the optical bench warm up in early December 2005 as a result of the better alignment of the instrument and increased signal to noise.

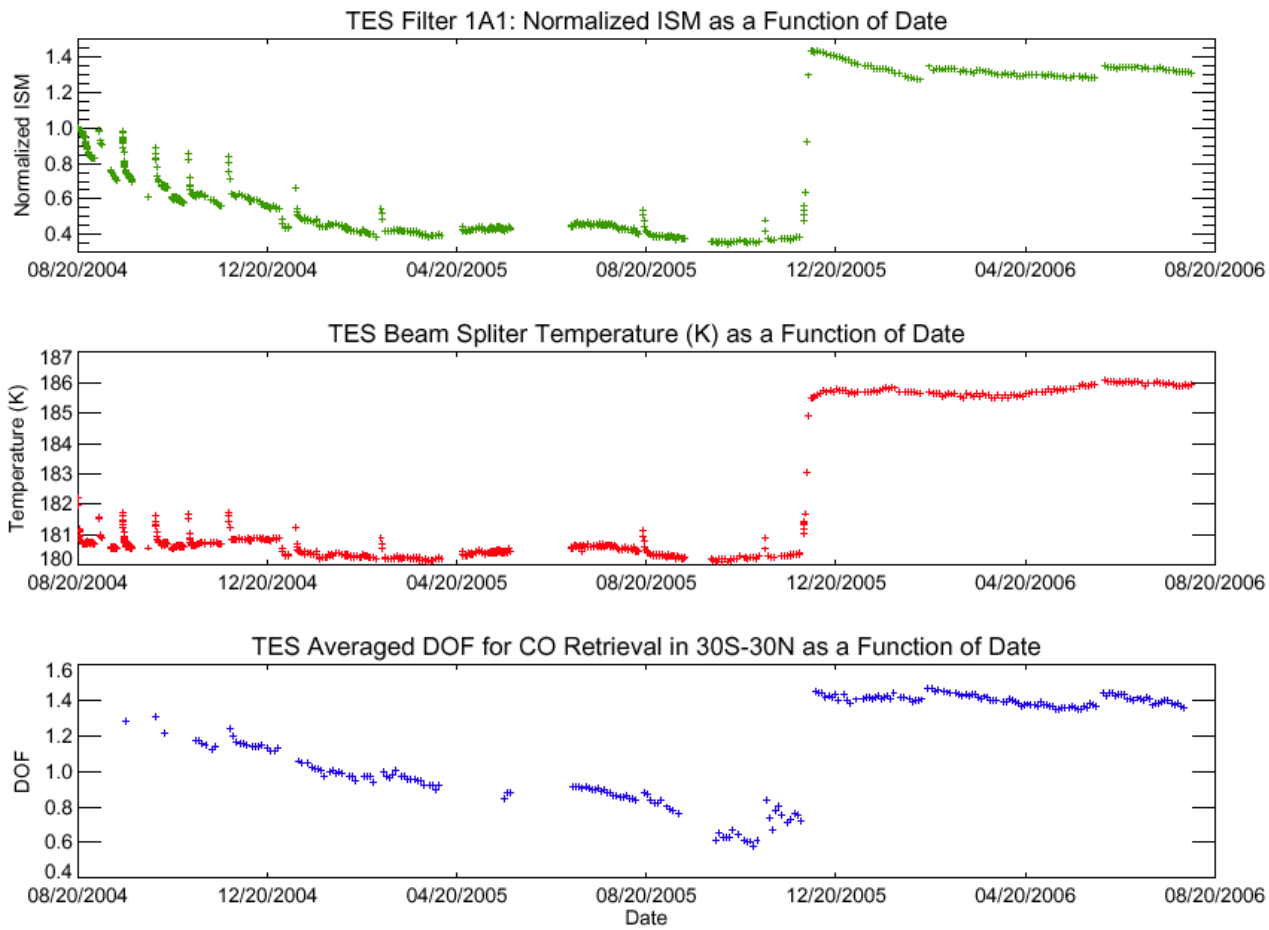

Figure 6-1 Time series of measured normalized Integrated Spectral Magnitude (ISM) (top panel), beamsplitter temperature (middle panel), and average DOFS for 30°N-30°S latitude. The ISM is normalized to 1.0 at the beginning of the time series.

6.3 Global distributions of CO from TES measurements

Carbon monoxide is a by-product of incomplete combustion of fossil fuels and biomass, and is produced by oxidation of methane (CH_4) and other hydrocarbons. The global distributions of TES CO fields reflect this basic understanding, e.g., the enhanced CO regions and their seasonal variations are co-located with the known source regions. Figure 6-2 shows TES CO monthly mean distributions at 681.3 hPa for Jan, Apr, July, and Oct 2007. In general, the northern hemispheric (and the tropics) show much more CO than the southern hemisphere due to the known distribution of natural and industrial sources. CO values in the winter/spring are larger than summer/fall due to the longer lifetime in seasons with less photochemical activity.

In central Africa, the enhanced CO corresponding to biomass burning occurs in two time periods, in Dec/Jan/Feb for latitudes north of the equator and in Jul/Aug/Sep south of the equator, corresponding to the local dry seasons. In South America, the biomass burning induced maximum in CO concentration occurred during Aug/Sep/Oct near equator. Enhanced levels of

CO over E. China can be related local pollution and can be seen throughout the year in the TES observations.

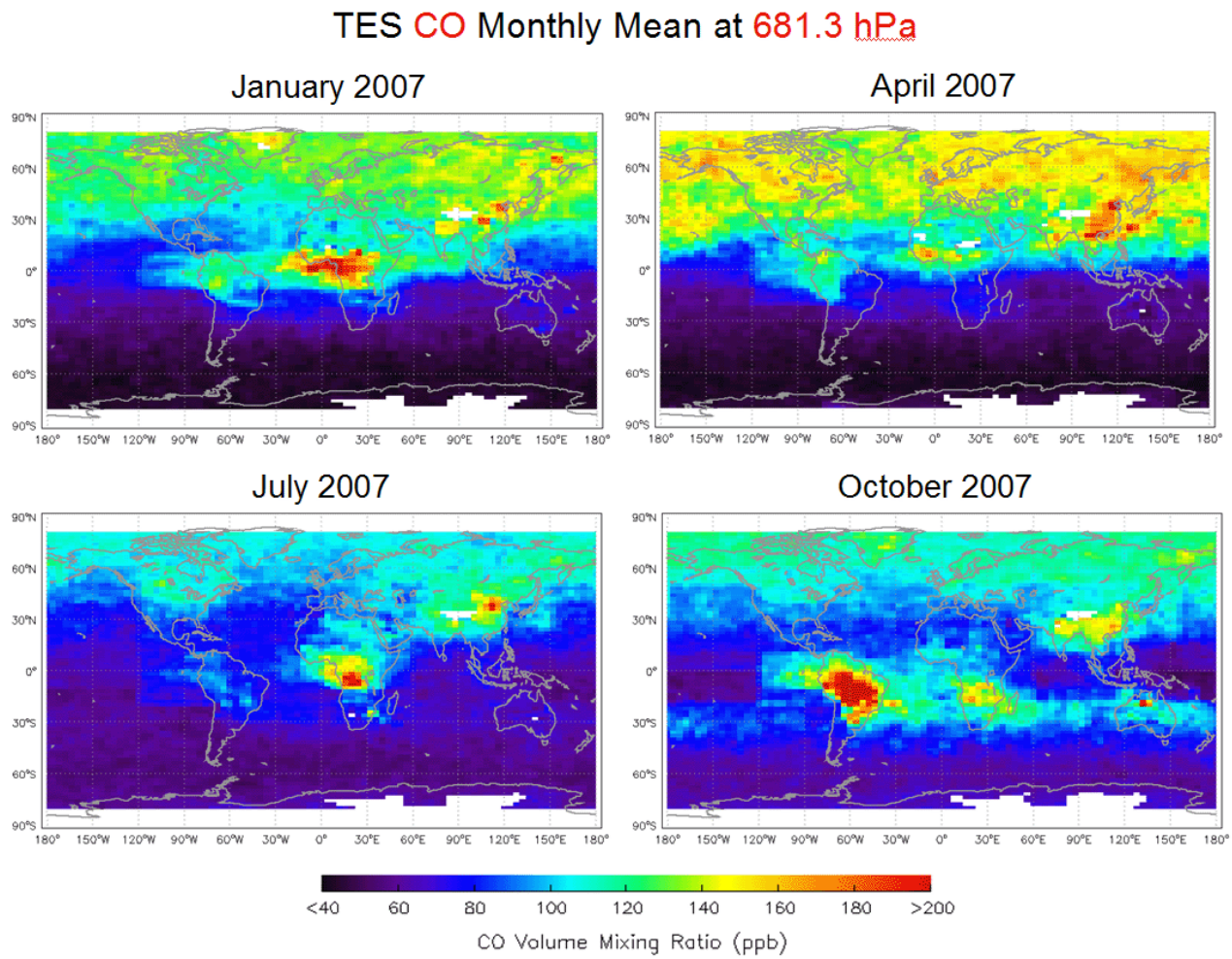

Figure 6-2 TES CO Global Distributions at 681.3 hPa for the Four Typical Months, Jan, April, July, and Oct 2007.

6.4 CO validation: Comparisons to in situ Aircraft Measurement

During the past a few years, several aircraft campaigns were conducted to study tropospheric chemistry and transport and to provide data for validation of the measurements made by the instruments on the Aura satellite. The TES team participated in the Aura Validation Experiment (AVE) campaigns: Oct-Nov 2004 based near Houston, Jan-Feb 2005 based in Portsmouth, NH, PAVE (Polar Aura Validation Experiment), and in Jan-Feb 2006 based in Costa Rica (CR-AVE). TES also participated INTEX-B (International Chemical Transport Experiment) based which had deployments in Houston, Honolulu and Anchorage in March-May 2006. The TES CO data from the time periods of theses campaigns are compared with the in situ measurements for the aircraft flights when there are the best coincidences between TES measurement location and the aircraft

CO profiles. Most validation results are reported in papers by M. Luo et al., 2007b and J. Lopez et al., 2008. We give a summary of the conclusions here.

In all aircraft campaigns, TES made a series of step and stare nadir observations with some footprints coincide with the aircraft tracks and the spiral profiling locations. During the AVE and CR-AVE campaigns, CO was measured by the NASA Ames Research Center Argus instrument on the WB-57 aircraft. The CO profiles were also measured by Aircraft Laser Infrared Absorption Spectrometer (ALIAS) of JPL during the CR-AVE. During the INTEX-B campaign the DACOM instrument by the NASA Langley Research Center was on board to measure CO.

For the TES and aircraft CO comparisons, all possible aircraft profiles, including profiles took while taking-off and landing and the vertical spirals, are extracted to match with TES profiles closest in times and locations. A few aircraft profiles and ~2-4 TES CO profiles per aircraft profile can be identified per campaign station, normally within a couple of hour and a couple to a few hundred kilometers. The next procedure is to apply TES retrieval operator to the in-situ profile, $x_{aircraft}$, to obtain the simulated aircraft profile as seen by TES, $x_{simul\text{-}aircraft}$,

$$x_{simul\text{-}aircraft} = Ax_{aircraft} + (I - A)x_a. \qquad \text{(Equation 6-1)}$$

where x_a is the TES CO retrieval a priori profile from the MOZART model (Model for OZone And Related chemical Tracers), and A is the averaging kernel. This profile as seen by TES is then compared to the TES retrieved CO profile. Figure 6-3 and Figure 6-4 summarized TES and the in-situ measurements of CO comparison statistics. The averaged comparisons are the best in Houston region for the two campaigns in Oct 2004 and March 2006. The differences between Argus and TES CO profiles are within TES retrieval errors and equivalent to CO spatial/temporal variability detected in both TES and Argus measurements. The comparisons of TES and DACOM CO profiles near Hawaii and Anchorage in April-May 2006 are not as good. In these regions, the aircraft DACOM CO profiles are characterized by plumes or enhanced CO layers, consistent with known features in the tracer fields due to transpacific transport of polluted air parcels originating from East Asia.

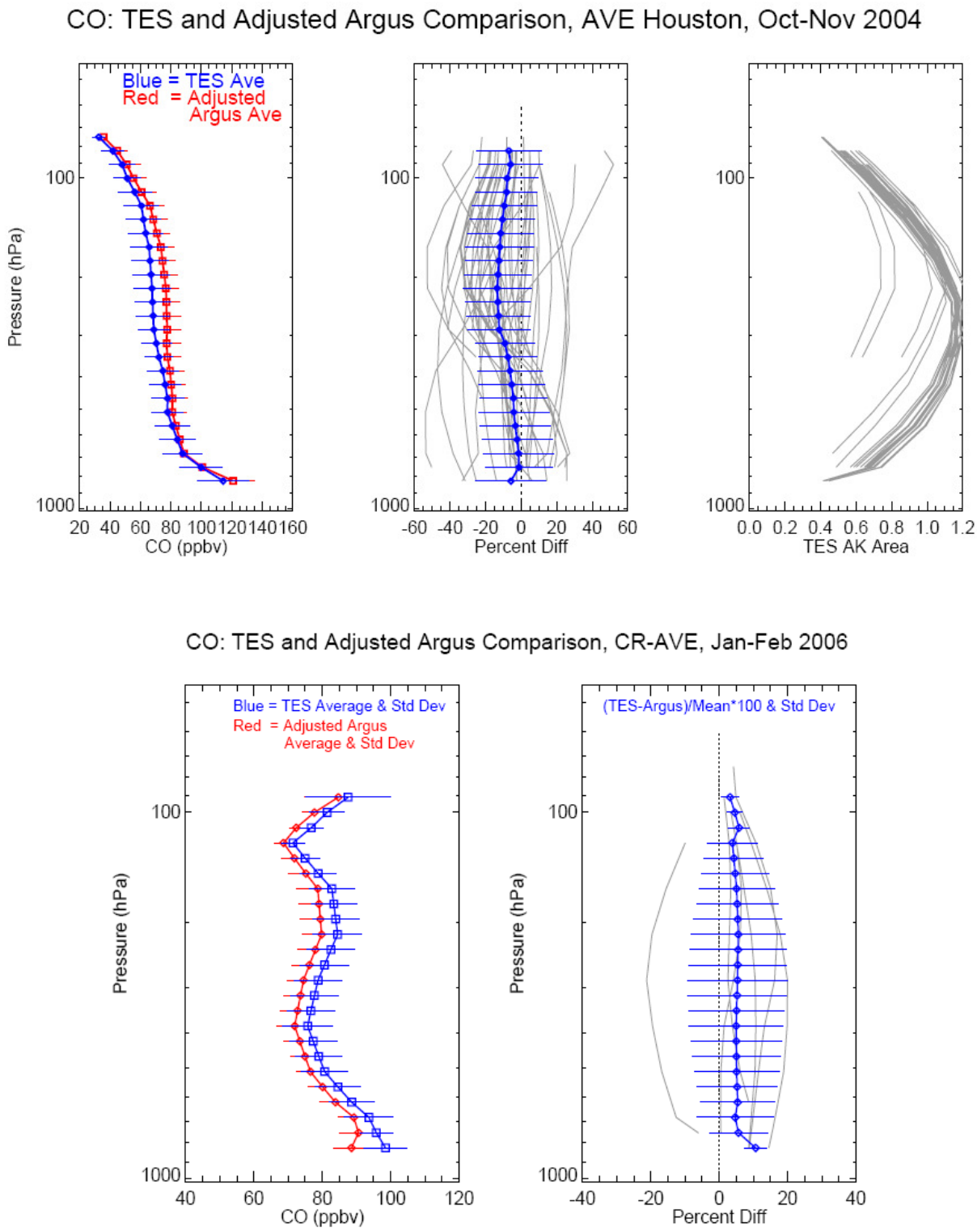

Figure 6-3 Averaged Argus and TES CO and difference profiles for Oct-AVE (upper three panels) and CR-AVE campaign (lower two panels). The Red line is the Argus data adjusted by the TES averaging kernel. For Oct-AVE case, the areas of the TES averaging kernels are shown with all selected cases having this value greater than 0.4.

CO: TES and Adjusted DACOM Comparison for INTEX-B near Houston, March 2006

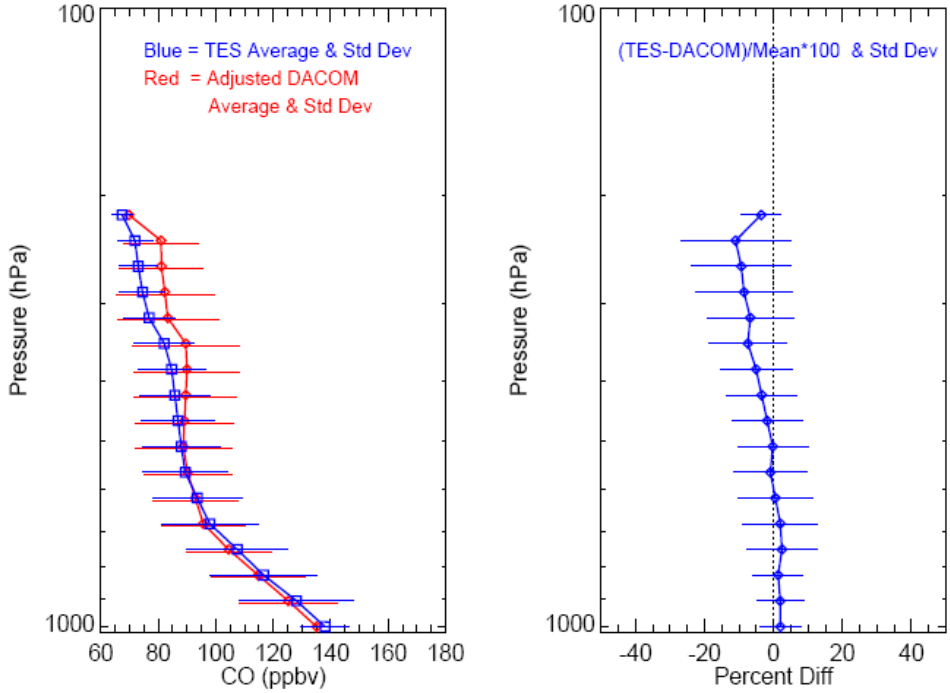

CO: TES and Adjusted DACOM Comparison for INTEX-B near Hawaii, April 2006

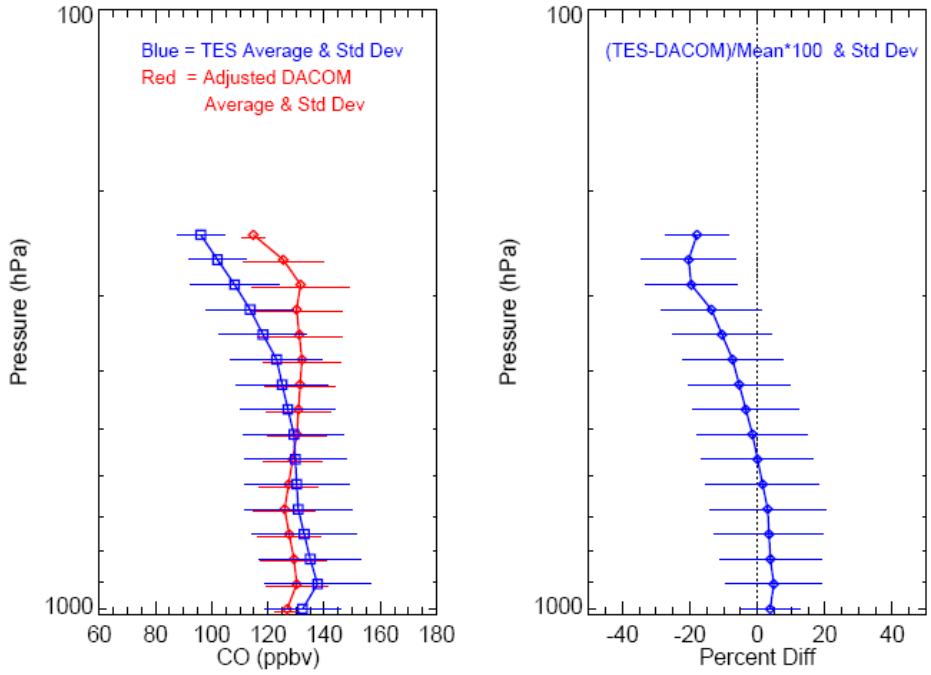

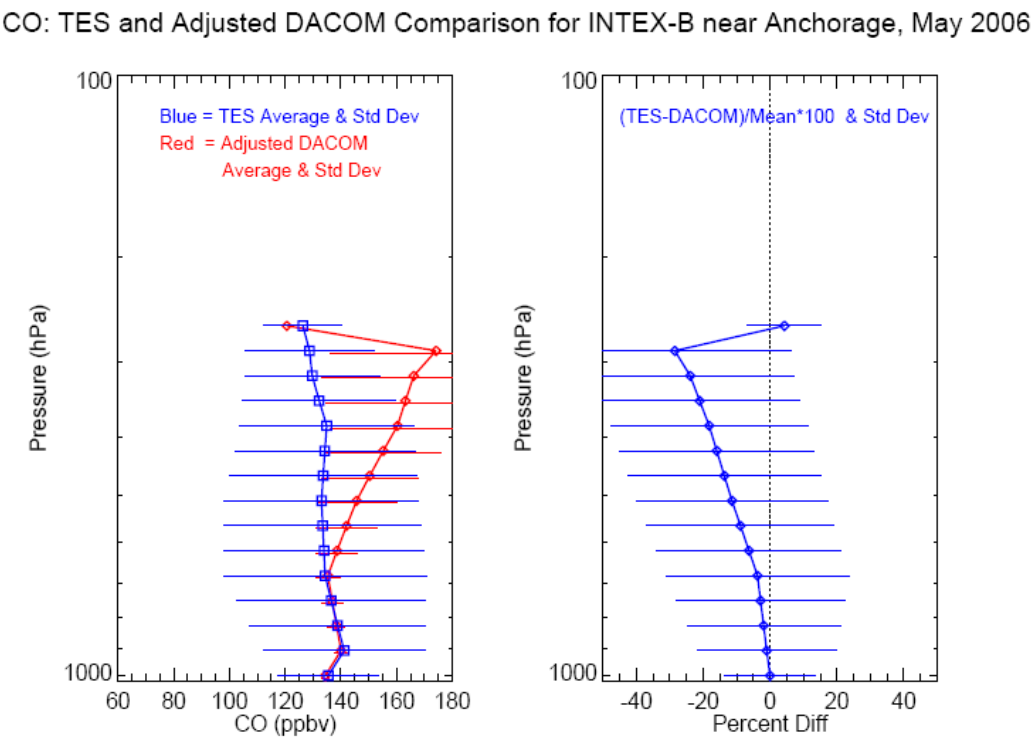

Figure 6-4 Summary plots for TES and DACOM CO profile comparisons during INTEX-B near Houston, March 2006 (left panel pairs), near Hawaii, Apr-May 2006 (middle panel pairs), and near Anchorage, May 2006 (right panel pairs). All the colored symbols and lines are defined the same as in Figure 6-5.

6.5 CO validation: comparisons to MOZAIC, ACE, MLS, and AIRS data sets

Some preliminary results are obtained in TES CO data validation using the CO data sets of MOZAIC (Measurements of Ozone and water vapor by In-service AIrbus aircraft, http://mozaic.aero.obs-mip.fr), ACE (Atmospheric Chemistry Experiment), MLS (Microwave Limb Sounder), and AIRS (Atmospheric Infrared Sounder). Detailed results are documented either in the previous version TES Validation Report V003 (Osterman et al., 2007) or papers (Rinsland et al., 2008, Warner et al., 2007).

6.6 CO Validation: Comparisons to MOPITT Data

The retrieval results of TES 16-orbit global survey measurements in Sept 20-21, 2004 (Run ID 2147) have been examined extensively by the TES science team. This day's TES CO data are also compared to the MOPITT (Measurements Of Pollution In The Troposphere) CO measurements (M. Luo et al., 2007a). Quantitative comparisons between TES and MOPITT CO at low, mid and upper troposphere and total column for this day are presented. Two steps are performed in the comparison, adjusting TES CO profiles to MOPITT a priori profile, and applying TES averaging kernels to MOPITT retrieved profiles. The final comparison is to compare TES retrieved CO profiles adjusted to MOPITT *a priori* and the MOPITT retrieved CO profiles adjusted to MOPITT averaging kernel. The agreement between the two CO fields becomes much better in all tropospheric levels and the total column, especially in the lower and upper troposphere where both instruments do not have much sensitivity in their measurements. Figure 6-5 shows the direct and final comparisons of the total CO columns between TES and

MOPITT. The final comparisons show TES CO is slightly lower than that of MOPITT by <5% in global averages.

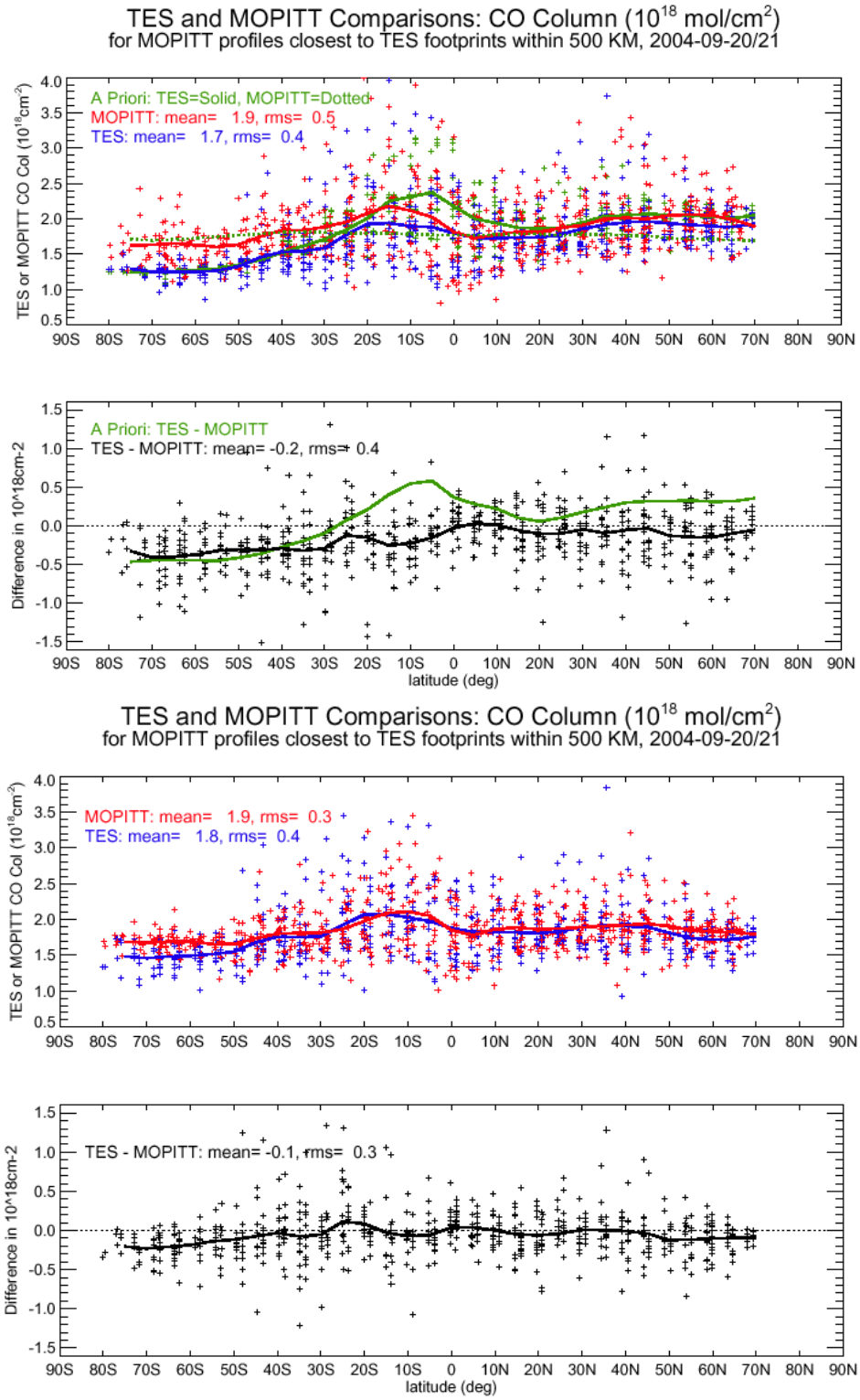

Figure 6-5 Comparisons of total CO column reported by TES and MOPITT. The first two panels are the 'direct' comparisons. The last two panels are the comparisons after the TES CO

being adjusted to MOPITT a priori profile and MOPITT CO profiles being adjusted by applying TES averaging kernels (M. Luo et al., 2007a).

(Ho et al. 2009) have also performed TES – MOPITT CO comparisons using July 2006 data. Similar conclusions are obtained.

6.7 CO validation: summary

Carbon Monoxide: Comparisons have been carried out between TES carbon monoxide retrievals and those from a variety of satellite and aircraft instruments. Global patterns of carbon monoxide as measured by TES are in good qualitative agreement with those seen by MOPITT on the NASA Terra satellite. Comparisons of profiles of CO between TES and MOPITT show good agreement when a priori information is accounted for correctly. TES carbon monoxide agrees to within the estimated uncertainty of the aircraft instruments, including both errors and the variability of CO itself. TES V004 CO data values do not show systematic changes from V003 with increased number of good quality retrieved profiles.

6.8 References

6.8.1 TES Carbon Monoxide References

[1] Ho, S.-P., D. P. Edwards, J. C. Gille, M. Luo, G. B. Osterman, S. S. Kulawik, and H. Worden (2009), A global comparison of carbon monoxide profiles and column amounts from Tropospheric Emission Spectrometer (TES) and Measurements of Pollution in the Troposphere (MOPITT), *Journal of Geophysical Research, 114*, D21307, (doi:10.1029/2009JD012242) November 6, 2009.

[2] Lopez, J. P., M. Luo, L. E. Christensen, M. Loewenstein, H. Jost, C. R. Webster, and G. Osterman (2008), TES carbon monoxide validation during two AVE campaigns using the Argus and ALIAS instruments on NASA's WB-57F, *Journal of Geophysical Research, 113*, D16S47, (doi:10.1029/2007JD008811) August 2, 2008.

[3] Luo, M., C. P. Rinsland, C. D. Rodgers, J. A. Logan, H. Worden, S. Kulawik, A. Eldering, A. Goldman, M. W. Shephard, M. Gunson, and M. Lampel (2007a), Comparison of carbon monoxide measurements by TES and MOPITT: the influence of a priori data and instrument characteristics on nadir atmospheric species retrievals, *J. Geophys. Res., 112*, D09303, (doi:101029/2006JD007663) May 3, 2007a.

[4] Luo, M., C. Rinsland, B. Fisher, G. Sachse, G. Diskin, J. Logan, H. Worden, S. Kulawik, G. Osterman, A. Eldering, R. Herman and M. Shephard (2007b), TES carbon monoxide validation with DACOM aircraft measurements during INTEX-B 2006, *J. Geophys. Res.*, *112,* D24S48, (doi:10.1029/2007JD008803) December 20, 2007b.

[5] Rinsland, C. P., M. Luo, J. A. Logan, R. Beer, H. M. Worden, J. R. Worden, K. Bowman, S. S. Kulawik, D. Rider, G. Osterman, M. Gunson, A. Goldman, M. Shephard, S. A. Clough, C. Rodgers, M. Lampel, and L. Chiou (2006), Nadir Measurements of carbon monoxide distributions by the Tropospheric Emission Spectrometer onboard the Aura Spacecraft: Overview of analysis approach and

examples of initial results, *Geophys. Res. Lett., 33*, (L2280610.1029/2006GL027000) November 22, 2006.

[6] Rinsland, C. P., M Luo, M. W. Shephard, C. Clerbaux, C. D. Boone, P. F. Bernath, L. Chiou, and P. F. Coheur (2008), Tropospheric Emission Spectrometer (TES) and Atmospheric Chemistry Experiment (ACE) measurements of tropospheric chemistry in tropical southeast Asia during a moderate El Niño in 2006, *J Quant Spectrosc Radiat Transfer, 109/10*, 10.1016/j.jqsrt.2007.12.020, 1931-1942, May 16, 2008.

[7] Warner, J., C. Barnet, M. Luo, G. Sachse (2008), Improved Tropospheric Carbon Monoxide Profiles Using Collocated AIRS and TES Satellite Measurements, submitted to *Geophys. Res. Lett.,* 2008.

6.8.2 TES References

[8] Osterman, G., (editor), K. Bowman, K. Cady-Pereira, T. Clough, A. Eldering, B. Fisher, R. Herman, D. Jacob, L. Jourdain, S. Kulawik, M. Lampel, Q. Li, J. Logan, M. Luo, I. Megretskaia, R. Nassar, G. Osterman, S. Paradise, V. Payne, H. Revercomb., N. Richards, M. Shephard, D. Tobin, S. Turquety, F. Vilnrotter, H. Worden, J. Worden, and L. Zhang (2007), Earth Observing System (EOS) Tropospheric Emission Spectrometer (TES) Data Validation Report (Version F04_04 data), Version 3.0, JPL Internal Report D-33192, November 5, 2007, available at: http://eosweb.larc.nasa.gov/PRODOCS/tes/validation/.

7. Validation of TES nadir Temperature Retrievals with Radiosondes

7.1 Executive Summary

The newly available TES V004 data feature improvements that significantly impact nadir temperature retrievals**.** Improvements were made to the forward model, retrieval strategy, constraints, and CO_2 climatology (Herman et al., (in prep); Shephard et al., 2008). TES V004 temperature retrievals have been compared with nearly coincident radiosonde (hereafter sonde) measurements from NCEP and NOAA ESRL databases. The NCEP sonde database is larger than the available NOAA ESRL database, so NCEP is used for temperature bias analysis. The bias in the TES temperature retrievals is significantly reduced in V004 to <0.7 K, compared with a 1 to 2 K upper tropospheric cold bias in V003. Here is a breakdown of the bias with different criteria:

bias over ocean is < 0.6 K (531 TES-sonde matches),

bias over land is < 0.5 K (1118 matches),

The rms is best determined from the NOAA ESRL database because exact sonde launch times are known, which allows a closer match in time to the TES retrieval. The TES temperature rms in V004 is 1 K in the stratosphere and upper troposphere and 1.5 K in the lower troposphere (at 500 to 900 hPa), compared to 2-4 K in V003. There is 0.5 to 1 K uncertainty simply due to the spatial and temporal variability of atmospheric temperature.

7.2 Improvements in TES temperature retrieval in V004

The newly available TES V004 includes several improvements that affect the retrieval of temperature (TATM), as described further by Herman et al., (in prep) and Shephard et al. (2008). These improvements include updates to the forward model, a new retrieval strategy, new constraints and improved CO_2 climatology. Spectroscopic updates to the forward model include CO_2 line mixing and line coupling (Niro et al., 2005), revised HITRAN H_2O linewidths (Gordon et al., 2007) and linestrengths (Coudert et al., 2008). Shephard et al. (2008) has reported that the CO_2 updates have improved the consistency of temperatures retrieved from the CO_2 ν_2 and ν_3 bands, based on retrievals from the AIRS and IASI instruments.

In V004, a new sequential retrieval strategy has been implemented. This has been made feasible by improvements in calibration and the forward model for the 2B1 filter (Shephard et al., 2008). In previous versions V002 and V003, TATM, H_2O, and O_3 were retrieved simultaneously (Bowman et al., 2002, 2006; Worden et al., 2004). For the V004 retrieval strategy, step one is retrieval of TATM (2B1 filter). The microwindows selected for temperature retrieval are within the CO_2 ν_2 band, spanning 671.32 to 901.48 cm^{-1} (14.896 μm to 11.093 μm). In step two, H_2O and O_3 are jointly retrieved from microwindows in the spectral bands of H_2O (2A1 filter) and O_3 (1B2 filter).

Constraints have been changed from climatological to altitude-dependent Tikhonov constraints (Kulawik et al., 2006). Furthermore, there is now surface temperature (TSUR) initial guess refinement for daytime land retrievals when the initial guess is too low.

The TES V004 L2 retrieval process has a new CO_2 climatology. This climatology incorporates

improved seasonal and geographic variations in CO_2 as well as scaling to account for the annual increase in global CO_2 levels. This is highly relevant to temperature retrievals from CO_2 spectroscopic lines because inaccurate assumptions about atmospheric CO_2 concentrations may lead to significant errors in atmospheric temperature retrievals, up to 0.5 K (see Figure 14 of Divakarla et al., 2006). The climatology is based on model results for the year 2004 from a chemical transport model (CTM) used in conjunction with a variety of other models to provide CO_2 surface fluxes [David Baker, pers. comm.]. The CTM used to create the time-varying three-dimensional CO_2 fields (longitude, latitude and pressure) is the Model of Atmospheric Transport and Chemistry (MATCH) (Nevison et al., 2008). Key surface CO_2 fluxes are derived from models including biospheric fluxes from the CASA land biosphere model, oceanic fluxes from the WHOI model and a realistic, annually-varying fossil fuel source scheme (Nevison et al., 2008). The CO_2 fields generated by the model compare well to GLOBALVIEW atmospheric CO_2 data. Model results were provided to the TES team for the year 2004. Monthly mean profiles were calculated for two longitude bins and 10-degree latitude bins. This binned monthly mean climatology for 2004 was then scaled upward yearly (by 1.0055) to match the annual increase in CO_2.

7.3 A priori constraint vector

The initial guess in the TES retrieval algorithm is set equal to an a priori profile (constraint vector). The TES V004 a priori constraint vectors come from NASA's Goddard Earth Observing System (GEOS) data assimilation system GEOS-5 (Rienecker et al., 2008). These are produced by the Global Modeling and Assimilation Office (GMAO) at the NASA Goddard Space Flight Center (GSFC). GEOS-5 profiles are produced on a 0.625° longitude by 0.5° latitude grid. These profiles are interpolated to the locations and pressure levels of TES retrievals. The a priori covariance matrices used for retrieval regularization are described in Bowman et al. (2006). Previously, TES V002 temperature a priori constraint vectors came from GMAO GEOS-4 (Herman et al. (in prep), and references therein).

GEOS-5 assimilates a wide range of operational satellite data and in situ sonde measurements. Sonde profiles are strong constraints on the thermal structure and winds throughout the troposphere, with an emphasis on continental regions where the observing network is denser. Space-based observations include the High Resolution Infrared Sounders (HIRS) and Advanced Microwave Sounders (AMSU) instruments on NOAA's operational sounders, which directly constrain temperature and moisture. GEOS-5 includes a direct assimilation of radiances from AMSU and HIRS in a three-dimensional variational assimilation, as well as radiances from the Advanced Infrared Sounder (AIRS) and AMSU instruments on NASA's EOS Aqua platform (Zhu and Gelaro, 2008). The previous GEOS-4 assimilated observations of temperature and water vapor using a one-dimensional variational approach (Bloom et al., 2005), where a retrieval was made using a six-hour forecast as a priori state; the retrieved variables were assimilated.

7.4 Current Validation Status of V004 nadir temperature

This section summarizes the latest validation comparisons for V004 TES nadir temperature retrievals. More detailed analysis will be reported by Herman et al. (in prep). TES global surveys spanning the years 2004 to 2008 have been compared with sondes. TES retrievals have been filtered by the master quality flag (Osterman et al., 2007). The TES operator has been applied to the sonde profiles, and differences are shown as (T_{TES} - $T_{insituw/AK}$). Levels where TES

has no sensitivity to temperature (i.e. where the sum of the row of the averaging kernel equals zero) are not included in the calculation of the mean difference.

7.4.1 NCEP sonde database compared with TES V004 TATM

The National Weather Service's National Center for Environmental Prediction (NCEP) maintains the quality controlled Integrated Global Radiosonde Archive (IGRA) (Durre et al., 2006). The sondes are typically launched four times daily (0, 6, 12, and 18 UTC (Universal Time Coordinated)) at more than 800 sites around the globe. We utilized this database to find TES global survey observations coincident with sonde profiles at all latitudes. At the time of this report, not all TES retrievals have been reprocessed in V004, but these comparisons include retrievals from 2004 through 2008 in all four seasons. The standard quality flag was applied to the TES retrievals.

Many types of sondes are included in the NCEP database. For the highest accuracy, we focus exclusively on Vaisala RS-80, RS-90 and RS-92 sondes. The RS-90 and RS-92 temperate sensors have ±0.2°C (2σ) uncertainty in the troposphere at night (Miloshevich et al., 2006). To improve the statistics, Vaisala RS-80, RS-90 and RS-92 sondes have been grouped together. These sondes are expected to exhibit similar temperature responses. The main problem with the NCEP database is that the sonde launch time has been rounded to the nearest 6 hours (0, 6, 12, 18 UTC). The actual launch time is unavailable and may be, in many cases, offset by an hour or more. This translates into increased rms due to the temporal mismatch between sonde measurement and satellite overpass. Tobin et al., (2006) compared pairs of sondes launched one hour apart from the DOE ARM SGP (Department of Energy Atmospheric Radiation Measurement – Southern Great Plains) site, and found an rms of 0.5 K due to atmospheric variability in one hour.

Figure 7-1, Figure 7-2 and Figure 7-3 show comparisons of TES with NCEP sondes for various criteria. For a pair of observations to be considered coincident, we require NCEP sonde launch times and TES observation times within two hours, and sonde launch locations within 250 km of the nearest TES footprint. These criteria were chosen to try to balance the trade-off between co-located, simultaneous observations and the statistical need for a large number of comparisons. These were the only criteria (plus standard quality flag), unless shown otherwise in the figures. Outliers have been removed by using an iterative 3-sigma rejection algorithm. Typically, we find that:

bias over ocean is <0.6 K (531 TES-sonde matches),

bias over land is <0.5 K (1118 matches),

A TES cold bias of 0.6 K or less is typically seen in the upper troposphere (200 to 300 hPa), with some latitudinal variation.

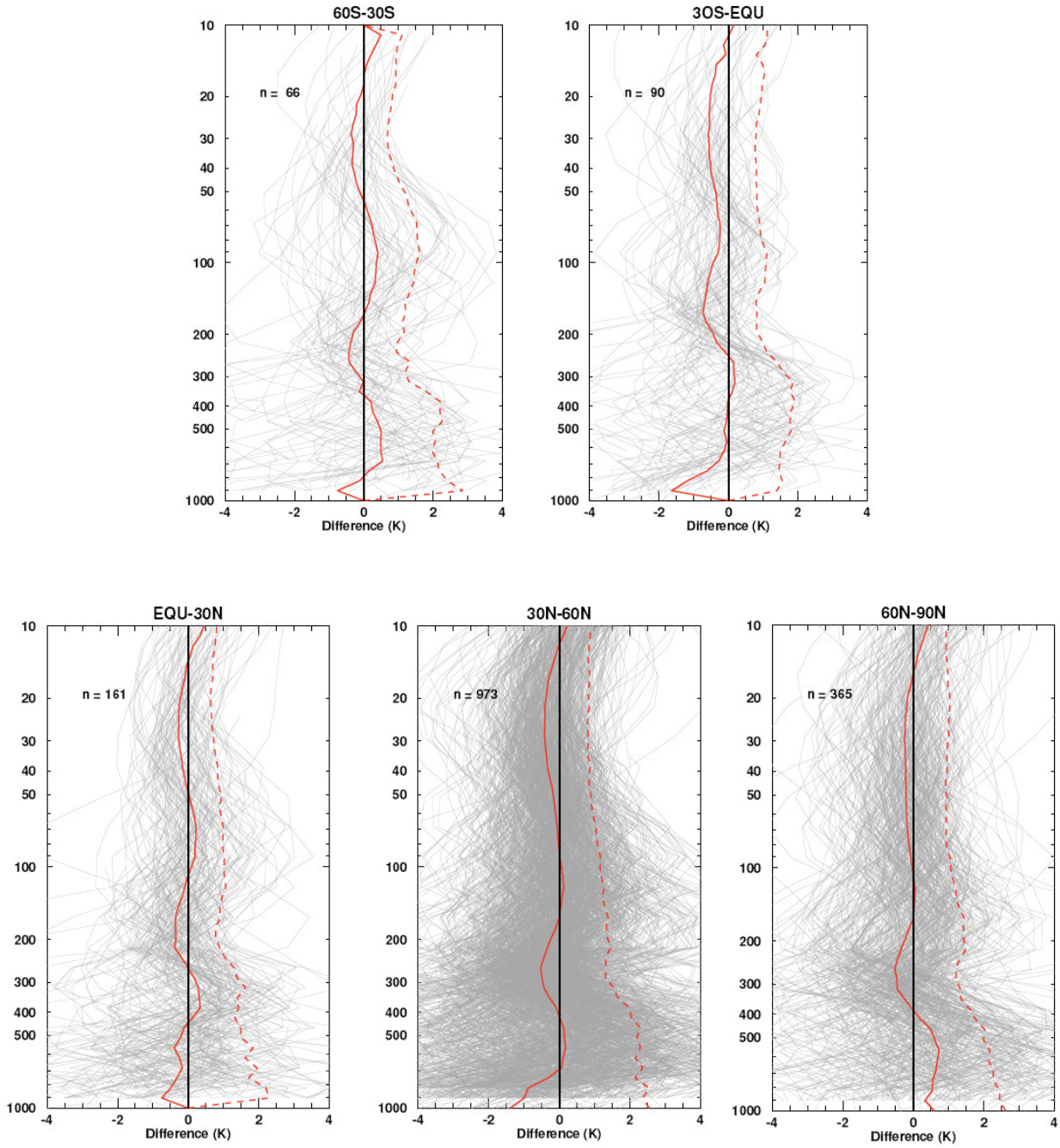

Figure 7-1 Temperatures from RS-80, RS-90 and RS-92 sondes in the NCEP database compared with TES V004, binned by latitude. In each panel, n individual temperature differences are shown (thin grey lines), with bias (solid red line) and rms (dashed red line). The TES operator has been applied to the sonde profiles, and differences are calculated as TES – sonde. Typically a TES cold bias is seen in the upper troposphere (especially at 30-60 N). Much of the rms is due to temporal fluctuations in temperature and uncertainty in the actual release time of the sondes. Figure prepared by K. Cady-Pereira from output of the sonde comparison tool.

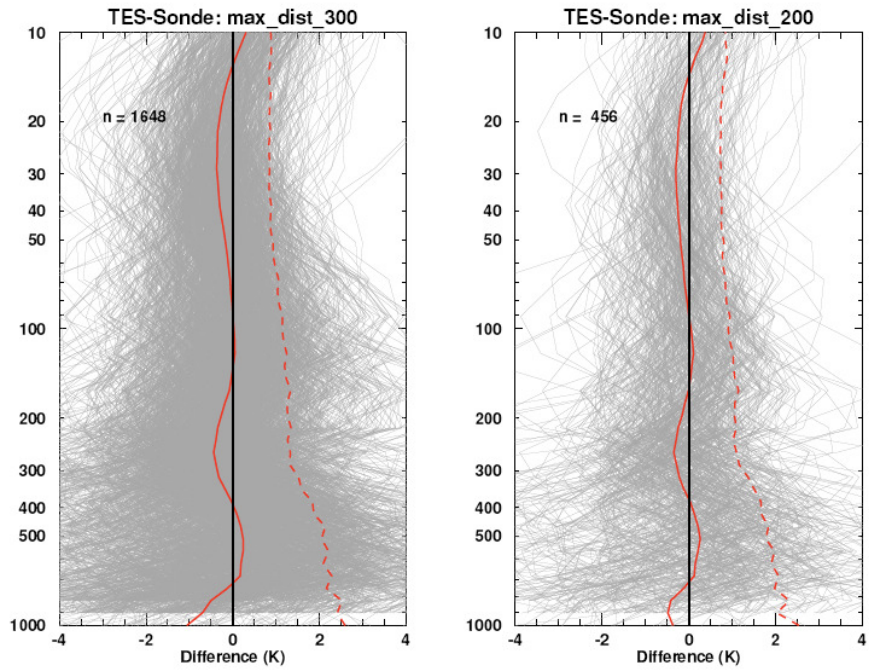

Figure 7-2 TES-NCEP comparisons, similar to Figure 7-1, for maximum distances < 300 km (left) and < 200 km (right). There is a slight improvement in both bias and rms for the closer coincidence due to spatial variability of tropospheric temperature.

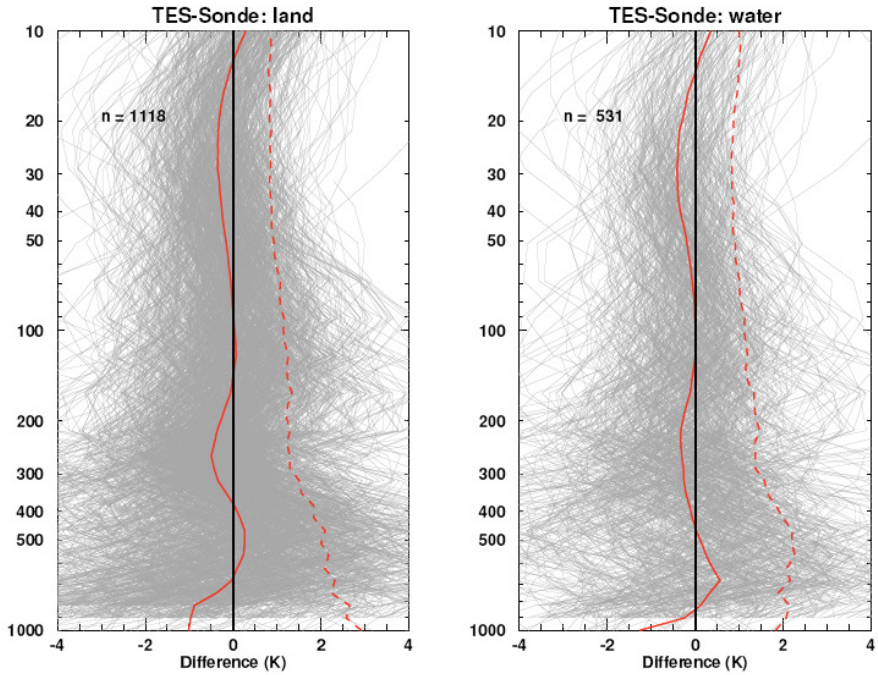

Figure 7-3 TES-NCEP comparison, similar to Figure 7-1, for two surface types: land (left) and ocean (right). The lower tropospheric rms is improved over ocean because the surface emissivity is better constrained.

7.4.2 NOAA ESRL sonde database compared with TES V004 TATM

The next set of comparisons was done with a global sonde database from the National Oceanic and Atmospheric Administration (NOAA) Earth System Research Laboratory (ESRL) Global Systems Division, formerly Forecast Systems Laboratory [M. Govett, pers. comm.]. The advantage of this database is that it includes the exact sonde release time (for sonde dates up to the end of 2007), which improves the temporal coincidence between TES and sonde, and the temperature rms. The NOAA ESRL database combines the IGRA global data with North American Global Telecommunications Service (GTS) sonde observations. Both undergo extensive checks for errors and hydrostatic consistency.

TES global surveys from 2004-2007 are matched with sonde profiles from the NOAA ESRL database within 100 km and -0.5 hr to +1.5 hr. The tightly constrained time match is possible because the exact sonde release time is known. Times are offset so that, on average, the sonde has ascended to the middle troposphere by the time of the Aura overpass and TES retrieval.

Figure 7-4 and Figure 7-5 show comparisons of TES with NOAA ESRL sondes. Similar to previous figures, outliers have been removed by using an iterative 3-sigma rejection algorithm. The solid red line is the temperature bias (TES minus sonde with averaging kernel) and the dashed red line is the temperature rms. The blue line is the TES observation error (measurement error plus systematic error). It is shown that the closer time coincidence improves the rms to 1-1.5 K.

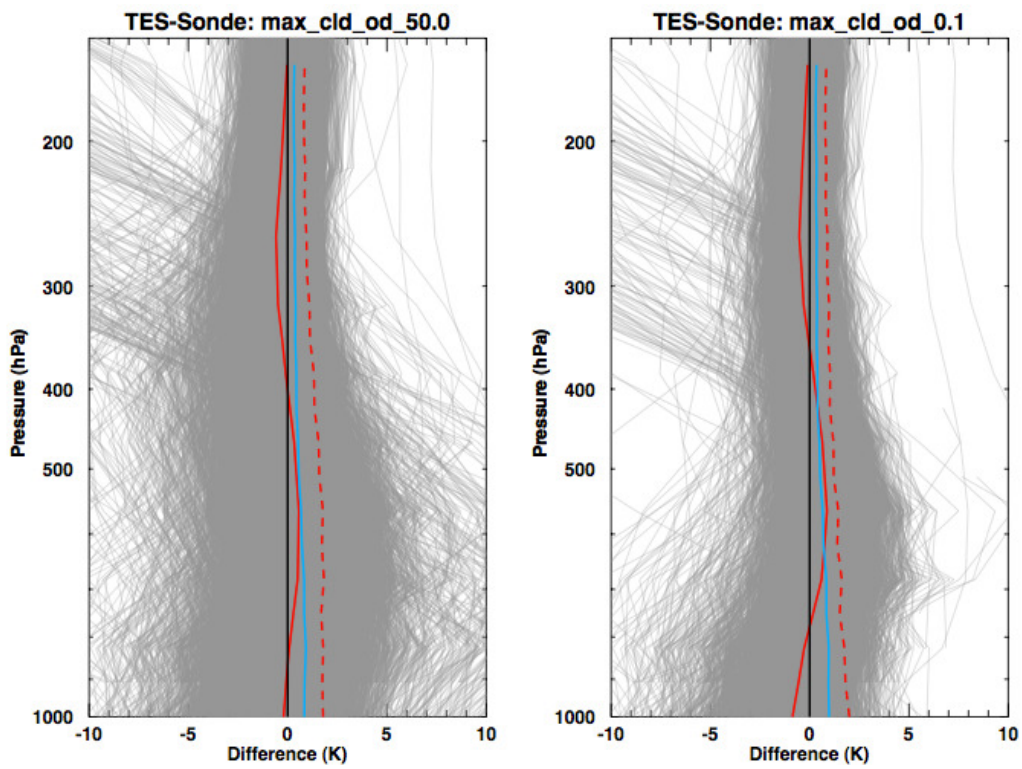

Figure 7-4 Temperature profiles from all radiosondes in the NOAA ESRL database compared with TES V004 for 2004-2008, including individual temperature differences (thin grey lines), bias (solid red line), rms difference (dashed red line), and the TES observation error (solid blue line). The TES operator has been applied to the radiosonde profiles, and the differences are

calculated as TES minus radiosonde (with averaging kernel). It is seen that the bias is typically less than 0.7 K. The rms is 1 K in the stratosphere and upper troposphere, increasing to 1.5 to 2 K in the lower troposphere. Little difference is seen between cloudy (left) and clear sky scenes (right), except that the near-surface bias is smaller for cloudy scenes (due to low information content, the temperature is closer to the a priori in this case).

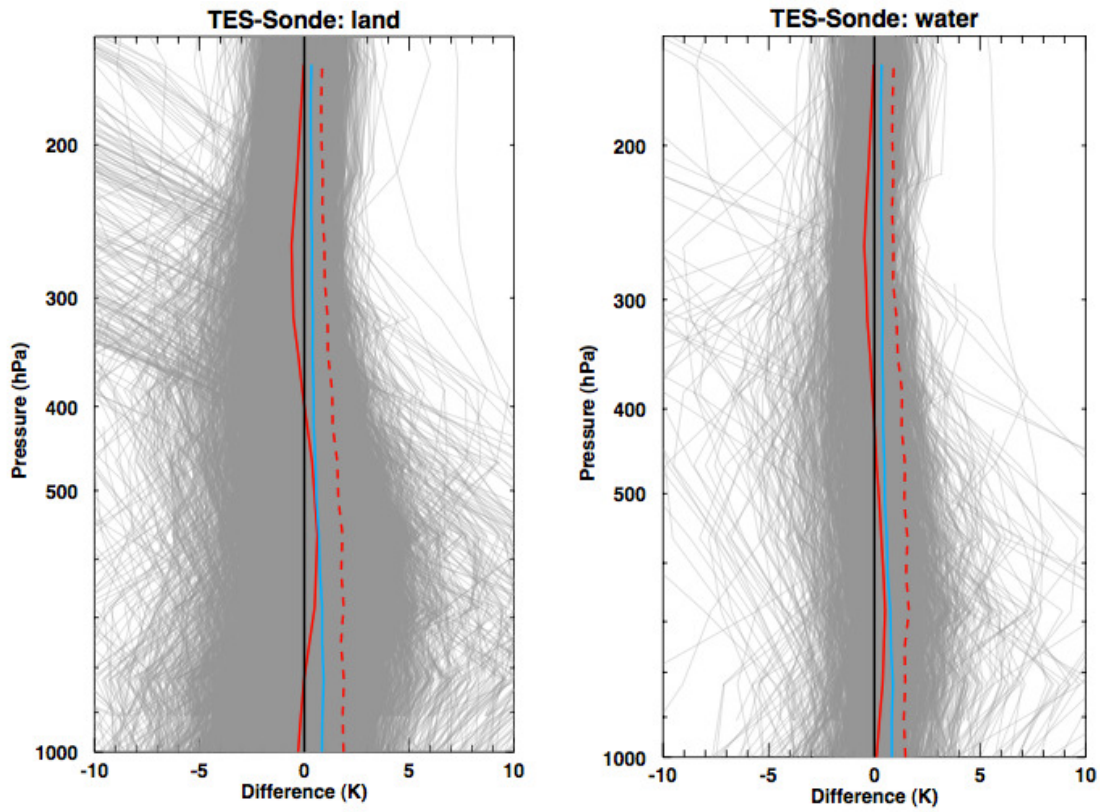

Figure 7-5 Temperature differences between TES and NOAA ESRL radiosondes, similar to Figure 7-4, for two surface types: land (left) and water (right). Bias (solid red line) is less than 0.7 K with subtle differences in the lower troposphere. The rms (dashed red line) is generally less than 1.5 K.

7.5 Comparison of V004 validation with V003/V002 retrievals

Overall, the V004 improvements have decreased the bias and rms of TES temperature retrievals compared to earlier versions V003 and V002.

Relative to RS-90 and RS-92 sondes, TES V002 had a cold bias in the upper troposphere and lower stratosphere, with a maximum TES cold bias of 1.4 K peaking at 400 hPa pressure, and a slight warm bias in the lower troposphere. TES V003 retrievals had improved bias in the upper troposphere and lower stratosphere (<0.5 K absolute bias at 10-250 hPa), but a 1 K cold bias with respect to sondes at pressures of 400 hPa and greater in the lower troposphere. The rms in V002 and V003 was considerable, between 2 and 4 K.

7.6 Summary

Validation of the new TES V004 temperature product is presented here. The V004 temperature has several improvements including: updates to the forward model, a new retrieval strategy, new constraints and improved CO_2 climatology from a 3-D CTM scaled to match the annual trend of CO_2. In this study, TES V004 temperature retrievals are compared with nearly coincident sonde measurements from the quality controlled NCEP IGRA and NOAA ESRL databases. The TES averaging kernels and a priori constraints have been applied to the in situ data, using temperature and water vapor constraint vectors from GMAO GEOS-5 analyses. The biases in the TES temperature retrievals are significantly reduced in V004 to 0.7 K or better, compared with a 1 to 2 K upper tropospheric cold bias in V003. The rms in V004 is typically 1 K in the stratosphere and upper troposphere increasing to 1.5 K in the lower troposphere, compared to 2-4 K in V003. There is 0.5 to 1 K uncertainty simply due to the spatial and temporal variability of atmospheric temperature.

7.7 References

7.7.1 TES Temperature References

[1] Herman, R.L., M. W. Shephard, K. E. Cady-Pereira, V. H. Payne, B. M. Fisher, S. S. Kulawik, G. B. Osterman, A. Eldering, S. Pawson, and D. N. Whiteman, New Comparisons of Tropospheric Emission Spectrometer Version 4 Temperature Retrievals with Radiosonde Measurements, in preparation.

[2] Shephard, M. W., V. H. Payne, K. E. Cady-Pereira, R. L. Herman, S. S. Kulawik, B. M. Fisher, A. Eldering, and S. A. Clough (2008), Investigation of biases in the TES temperature retrievals, *Eos Trans. AGU, 89(23),* Joint Assem. Supplement, Abstract A31A-02 (2008).

7.7.2 TES References

[3] Bowman, K. W., J. Worden, T. Steck, H. M. Worden, S. Clough, and C. Rodgers (2002), Capturing time and vertical variability of tropospheric ozone: A study using TES nadir retrievals, *J. Geophys. Res., 107, No. D23*, 4723, (doi:10.1029/2002JD002150) December 14, 2002.

[4] Bowman, K. W., C. D. Rodgers, S. S. Kulawik, J. Worden, E. Sarkissian, G. Osterman, T. Steck, M. Luo, A. Eldering, M. W. Shephard, H. Worden, M. Lampel, S. A. Clough, P. Brown, C. Rinsland, M. Gunson, R. Beer (2006), Tropospheric emission spectrometer: Retrieval method and error analysis, *IEEE Trans. Geosci. Remote Sens., 44(5)*, 1297-1307, May 2006.

[5] Gordon, I.E., L. S. Rothman, R. R. Gamache, D. Jacquemart, C. Boone, P. F. Bernath, M. W. Shephard, J. S. Delamere, S. A. Clough (2007), Current updates of water vapor line list in HITRAN: A new "Diet" for air-broadened half-widths, *Journal of Quantitative Spectroscopy & Radiative Transfer, 108,* 389-402, (doi:10.1016/j.jqsrt.2007.06.009) 2007.

[6] Kulawik, S. S., G. B. Osterman, D. B. A. Jones, and K. W. Bowman (2006), Calculation of Altitude-Dependent Tikhonov Constraints for TES Nadir Retrievals, *IEEE Transactions on Geoscience and Remote Sensing, 44 (No.5),* Special Issue on Aura, 1334-1342, May 2006.

[7] Osterman, G. B. (editor), K. Bowman, K. Cady-Pereira, T. Clough, A. Eldering, B. Fisher, R. Herman, D. Jacob, L. Jourdain, S. Kulawik, M. Lampel, Q. Li, J. Logan, M. Luo, I. Megretskaia, R. Nassar, G. Osterman, S. Paradise, V. Payne, H. Revercomb., N. Richards, M. Shephard, D. Tobin, S. Turquety, F. Vilnrotter, H. Worden, J. Worden, and L. Zhang (2007), Earth Observing System (EOS) Tropospheric Emission Spectrometer (TES) Data Validation Report (Version F04_04 data), Version 3.0, JPL Internal Report D-33192, November 5, 2007, available at: http://eosweb.larc.nasa.gov/PRODOCS/tes/validation/

[8] Worden, J., S. S. Kulawik, M. W. Shephard, S. A. Clough, H. Worden, K. Bowman, and A. Goldman (2004), Predicted errors of tropospheric emission spectrometer nadir retrievals from spectral window selection, *J. Geophys. Res., 109*, D09308, May 15, 2004.

7.7.3 General References

[9] Bloom, S., A. da Silva, D. Dee, M. Bosilovich, J.-D. Chern, S. Pawson, S. Schubert, M. Sienkiewicz, I. Stajner, W.-W. Tan, M.-L. Wu (2005). Documentation and Validation of the Goddard Earth Observing System (GEOS) Data Assimilation System - Version 4. *Technical Report Series on Global Modeling and Data Assimilation 104606, Vol. 26,* 187 pages, April 2005. Available from (paste entire link including pdf into browser):

http://ntrs.nasa.gov/archive/nasa/casi.ntrs.nasa.gov/20050175690_2005173043.pdf.

[10] Coudert, L. H., G. Wagner, M. Birk, Y. I. Baranov, W. J. Lafferty, and J.-M. Flaud (2008), The $H_2{}^{16}O$ molecule: Line position and line intensity analyses up to the second triad, *J. Molec. Spectros., Vol. 251, Issues 1-2 ,* 339-357, September-October 2008).

[11] Divakarla, M. G., C. D. Barnet, M. D. Goldberg, L. M. McMillin, E. Maddy, W. Wolf, L. Zhou, and X. Liu (2006), Validation of Atmospheric Infrared Sounder temperature and water vapor retrievals with matched radiosonde measurements and forecasts, *J. Geophys. Res., 111,* D09S15, (doi: 10.1029/2005JD006116) April 6, 2006.

[12] Durre, I., R.S. Vose, and D.B. Wuertz (2006), Overview of the integrated global radiosonde archive*, J. Climate, 19(1),* 53-68, January, 1, 2006.

[13] Miloshevich, L. M., H. Vömel, D. N. Whiteman, B. M. Lesht, F. J. Schmidlin, and F. Russo (2006), Absolute accuracy of water vapor measurements from six operational radiosonde types launched during AWEX-G and implications for AIRS validation, *J. Geophys. Res., 111,* D09S10, (doi: 10.1029/2005JD006083) April 7, 2006.

[14] Nevison, C. D., N. M. Mahowald, S. C. Doney, I. D. Lima, G. R. van der Werf, J. T. Randerson, D. F. Baker, P. Kasibhatla, and G. A. McKinley (2008), Contribution of ocean, fossil fuel, land biosphere and biomass burning carbon fluxes to seasonal and

interannual variability in atmospheric CO2, *J. Geophys. Res., 113,* G01010, (doi:10.1029/2007JG000408) February 12, 2008.

[15] Niro, F., F. Hase, C. Camy-Peyret, S. Payan, and J. M. Hartmann (2005), Spectra calculations in central and wing regions of CO_2 IR bands between 10 and 20 μm. II. Atmospheric solar occultation spectra, *J. Quant. Spectrosc. Radiat. Transfer, 90*, 43-59, (doi:10.1016/j.jqsrt.2004.04.004) 2005.

[16] Rienecker, M. M., M. J. Suarez (editor), R. Todling, J. Bacmeister, L. Takacs, H.-C. Liu, W. Gu, M. Sienkiewicz, R. D. Koster, R. Gelaro, I. Stajner and J.E. Nielson (2008), The GEOS-5 Data Assimilation System- Documentation of Versions 5.0.1, 5.1.0, and 5.2.0 *NASA Technical Report Series on Global Modeling and Data Assimilation 104606, Vol.27.*, December 2008.

[17] Tobin, D. C., H. E. Revercomb, R. O. Knuteson, B. M. Lesht, L. L. Strow, S. E. Hannon, W. F. Felt, L. A. Moy, E. J. Fetzer, and T. S. Cress (2006), Atmospheric Radiation Measurement site atmospheric state best estimates for Atmospheric Infrared Sounder temperature and water vapor retrieval validation, *J. Geophys. Res., 111,* doi: 10.1029/2005JD006103.

[18] Zhu, Y., and R. Gelaro (2008), Observation Sensitivity Calculations Using the Adjoint of the Gridpoint Statistical Interpolation (GSI) Analysis System, *Monthly Weather Review, Volume 136, Issue 1*, pp. 335-351, (DOI:10.1175/MWR3525.1) January 2008 - available from http://gmao.gsfc.nasa.gov/pubs/ref/archive/ref_2008.php.

8. Sea Surface Temperature

TES retrievals of sea surface temperature rely on validation of previous data versions, as described in detail in the TES Validation Report V003 (Osterman et al., 2007). V003 sea surface temperature (SST) was compared with Reynolds Optimally Interpolated (ROI) weekly SST for the time period Jan 2005 through July 2008. In clear sky conditions, TES SST versus ROI has a bias of -0.04 K (daytime) and -0.20 K (nighttime). The day/night difference is within the uncertainty of the predicted value based on ocean skin versus ocean bulk SST [D. Kerola, pers. comm.].

8.1 References

8.1.1 TES References

[1] Beer, R. (2006), TES on the Aura Mission: Scientific Objectives, Measurements and Analysis Overview, *IEEE Transactions on Geoscience and Remote Sensing, 44 (No.5), Special Issue on Aura,* 1102-1105, May 2006.

[2] Bowman, K. W., C.D. Rodgers, S. S. Kulawik, J. Worden, E. Sarkissian, G. Osterman, T. Steck, M. Lou, A. Eldering, M. Shephard, H. Worden, M. Lampel, S. Clough, P. Brown, C. Rinsland, M. Gunson, R. Beer (2006), Tropospheric Emission Spectrometer: Retrieval Method and Error Analysis, *IEEE Transactions on Geoscience and Remote Sensing, 44 (No.5), Special Issue on Aura,* 1297-1307, May 2006.

[3] Kulawik, S. S., J. Worden, A. Eldering, K. Bowman, M. Gunson, G. B. Osterman, L. Zhang, S. A. Clough, M. W. Shephard, R. Beer (2006), Implementation of cloud retrievals for Tropospheric Emission Spectrometer (TES) atmospheric retrievals: part 1. Description and characterization of errors on trace gas retrievals, *J. Geophys. Res., 111,* D24204, (doi:10.1029/2005JD006733) December 22, 2006.

[4] Osterman, G., (editor), K. Bowman, K. Cady-Pereira, T. Clough, A. Eldering, B. Fisher, R. Herman, D. Jacob, L. Jourdain, S. Kulawik, M. Lampel, Q. Li, J. Logan, M. Luo, I. Megretskaia, R. Nassar, G. Osterman, S. Paradise, V. Payne, H. Revercomb., N. Richards, M. Shephard, D. Tobin, S. Turquety, F. Vilnrotter, H. Worden, J. Worden, and L. Zhang (2007), Earth Observing System (EOS) Tropospheric Emission Spectrometer (TES) Data Validation Report (Version F04_04 data), Version 3.0, JPL Internal Report D-33192, November 5, 2007

[5] Worden, H., R. Beer, K. W. Bowman, B. Fisher, M. Luo, D. Rider, E. Sarkissian, D. Tremblay, J. Zong, (2006), TES Level 1 Algorithms: Interferogram Processing, Geolocation, Radiometric and Spectral Calibration, *IEEE Transactions on Geoscience and Remote Sensing, 44 (No.5), Special Issue on Aura,* 1288-1296, May 2006.

8.1.2 General References

[6] Masuda, K., T. Takashima and Y. Takayama (1988) Emissivity of pure and sea waters for the model sea surfaces in the infrared window regions, *Remote Sensing of Environment, 24,* 313-329, (1988).

[7] Smith, T. M., R. W. Reynolds and C. F. Ropelewski (1994), Optimal Averaging of Seasonal Sea Surface Temperatures and Associated Confidence Intervals (1860-1989), *J. Climate, 7,* 949-964, (1994).

9. Water Vapor

A number of comparisons have been made between TES V004 water vapor and other data sources, including radiosondes and aircraft. More than most species retrieved by TES, tropospheric water vapor is highly variable over short distances. Therefore, the key to water validation is to perform statistics on large datasets to determine possible biases. The most mature of all these analyses is the comparison to radiosondes and that work is presented in this document.

TES retrieves water vapor in the troposphere, with a sensitivity that decreases significantly at pressures less than 200 hPa, as shown below. Figure 9-1 shows information about typical TES water vapor retrievals during special observations in Transect viewing mode. These Transect scans are spaced 12 km apart, providing coverage that is much more dense than the routine TES Global Survey viewing mode. Specifically, Figure 9-1 shows the diagonal of the averaging kernel, an indicator of relative sensitivity of TES to water vapor at each pressure level.

The main objectives for obtaining retrieved water vapor from TES are to measure the isotopic ratio of HDO/H2O (see Section 10) and to obtain the most likely state of the atmosphere within the field-of-view. This applies whether water vapor is a tracer of air mass, of chemical interest, or whether it is an interferent. The central objective of TES is the measurement of global profiles of tropospheric ozone and its precursors, of which water is a key one. Many validations of water vapor retrievals rely heavily on profiles obtained from radiosonde measurements.

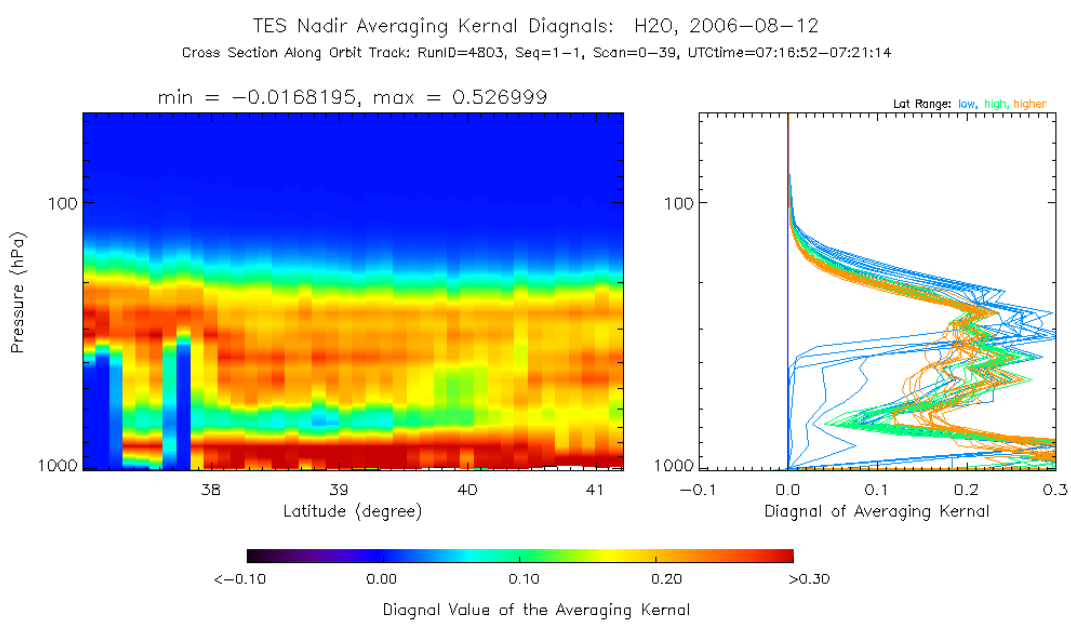

Figure 9-1 Diagonal of the TES nadir averaging kernel for water vapor, runid 4803, Transect special observation at Beltsville, MD, 12 Aug 2006. Sensitivity to water vapor decreases at high altitude, typically at pressures less than 200 hPa. Figure generated by M. Luo.

9.1 Previous versions of TES Water Vapor

TES uses an optimal estimation non-linear least squares retrieval (Bowman et al., 2006). The main differences between V002 and V003 that influence the TES water vapor retrievals are: (i) improved TES temperature retrievals due to inclusion of the CO_2 $\nu 2$ spectral region with improved CO_2 forward model calculations (Shephard et al., 2008a); (ii) the migration of TES initial guess and a priori from GEOS-4 to GEOS-5; (iii) a lowered minimum value for the a priori cloud optical depth in order to better handle clouds with lower optical depths; and (iv) the addition of more surface microwindows to help characterize the surface.

The main difference between V003 and V004 is sequential retrievals of temperature, ozone and water vapor. Sequential retrieval reduces the potential impact of systematic errors not adequately accounted for in the retrieval. For V003, TES water vapor is reported from the H2O/HDO joint retrieval step, which comes after the O3/H2O/T joint retrieval step. For V004, the sequential steps are as follows: atmospheric temperature is retrieved using microwindows in the CO2 ν2 region. In the next step, water vapor and ozone are jointly retrieved. Next, water vapor and HDO are jointly retrieved. Water is reported from the H2O/HDO step. Shephard et al. (2008a) showed that V004 significantly reduces biases relative to the a priori GEOS-5 compared to earlier versions of the TES retrievals. Shephard et al. (2008a) also performed a radiance closure experiment on TES V003 water vapor from the Water Vapor Validation Experiments (WAVES) campaign at Beltsville, Maryland. This experiment indicated that the estimated systematic errors from the forward model, TES V003 measurements, in-situ observations, and the retrieved temperature profile and clouds were likely not large enough to account for systematic differences in tropospheric water vapor. Analysis is ongoing for V004 data from WAVES and the more recent Measurements of Humidity in the Atmosphere Validation Experiments (MOHAVE) (Leblanc et al., 2011).

9.2 A priori constraint vector

The initial guess in the TES retrieval algorithm is set equal to an a priori profile (constraint vector). The TES v004 a priori constraint vectors come from NASA's Goddard Earth Observing System (GEOS) data assimilation system GEOS-5 (Rienecker et al., 2008). These analyses are produced by the Global Modeling and Assimilation Office (GMAO) at the NASA Goddard Space Flight Center (GSFC). GEOS-5 profiles are produced on a 0.625° longitude by 0.5° latitude grid. These profiles are interpolated to the locations and pressure levels of TES retrievals. The a priori covariance matrices used for retrieval regularization are described in Bowman et al. (2006). GEOS-5 assimilates a wide range of operational satellite data and in situ radiosonde measurements. Radiosonde profiles are strong constraints on the thermal structure and winds throughout the troposphere, with an emphasis on continental regions where the observing network is denser. Space-based observations include the High Resolution Infrared Sounders (HIRS) and Advanced Microwave Sounders (AMSU) instruments on NOAA's operational sounders, which directly constrain temperature and moisture. GEOS-5 includes a direct assimilation of radiances from AMSU and HIRS in a three-dimensional variational assimilation, as well as radiances from the Advanced Infrared Sounder (AIRS) and AMSU instruments on NASA's EOS Aqua platform (Zhu and Gelaro, 2008). The previous GEOS-4

assimilated observations of temperature and water vapor using a one-dimensional variational approach (Bloom et al., 2005), where a retrieval was made using a six-hour forecast as a priori state; the retrieved variables were assimilated.

9.3 Comparison of TES Water Vapor with Radiosondes

For purposes of evaluating the quality of TES water vapor retrievals, the most readily available correlative data are provided by radiosondes. In this study, TES water vapor retrievals are compared with nearly coincident radiosonde measurements. Radiosonde data come from a global database from the National Oceanic and Atmospheric Administration (NOAA) Earth System Research Laboratory (ESRL) Global Systems Division [M. Govett, pers. comm.]. The NOAA ESRL database combines the IGRA global data with North American Global Telecommunications Service (GTS) radiosonde observations. This database features the exact radiosonde launch time, which improves the temporal coincidence between TES and radiosonde significantly. The disadvantage of radiosondes is the spatial mismatch between the satellite retrieval footprint (8 km by 5 km for TES) and the radiosonde data (a vertical profile of in-situ measurement with no horizontal information).

For radiosondes, water vapor measurements (i.e. dewpoint temperatures) have smaller systematic biases at nighttime [L. Miloshevich, pers. comm.], so most of the comparisons shown here are for night matches. The coincidence constraints are TES-radiosonde matches within 100 km and -0.5 hours to +1.5 hours. The tightly constrained time match is possible because the exact launch time of the radiosonde is known. Times are offset so that, on average, the radiosonde has ascended to the middle troposphere b the time of the Aura overpass and TES retrieval. The TES averaging kernel has been applied to the radiosonde profiles, and standard water data quality flags applied to the TES retrieval (Osterman et al., TES Data User's Guide D-38042, 2009). Outliers have been removed by using an iterative three-sigma rejection algorithm. In each plot, differences between TES and radiosonde are shown as H_2O(TES) minus H_2O(radiosonde with averaging kernel applied). The comparisons below include TES retrievals from the years 2004 through 2008 (TES run ids 2147-10105).

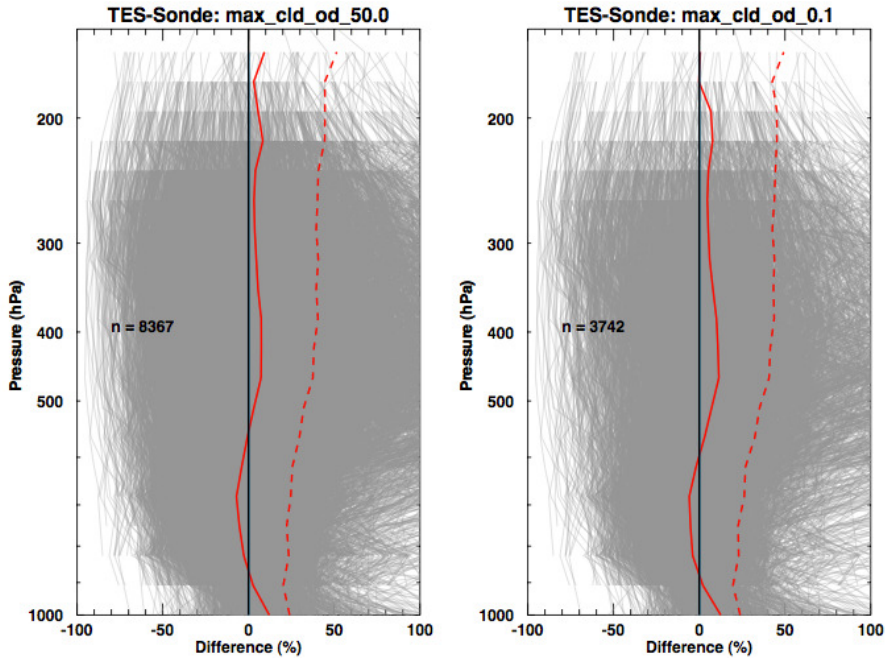

Figure 9-2 Water vapor percent differences between TES V004 and radiosondes in the NOAA ESRL database within 100 km and -0.5 to +1.5 hours. In each panel, n individual matches are shown (thin grey lines) with rms (dashed red lines) and bias (solid red lines). The TES operator has been applied to the radiosonde profiles, and differences are calculated as (TES-radiosonde)/TES. Figure prepared using software from K. Cady-Pereira from output of the TES sonde comparison tool.

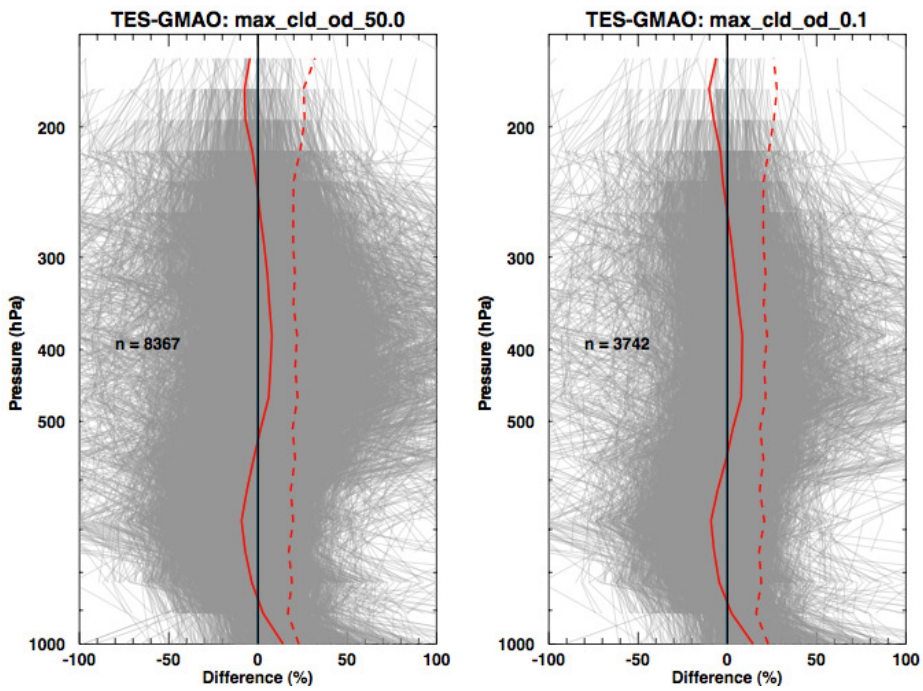

Figure 9-3 Water vapor percent differences between TES V004 and GMAO GEOS-5 analyses interpolated to the location of the TES retrievals. Similar legend as in Figure 9-2.

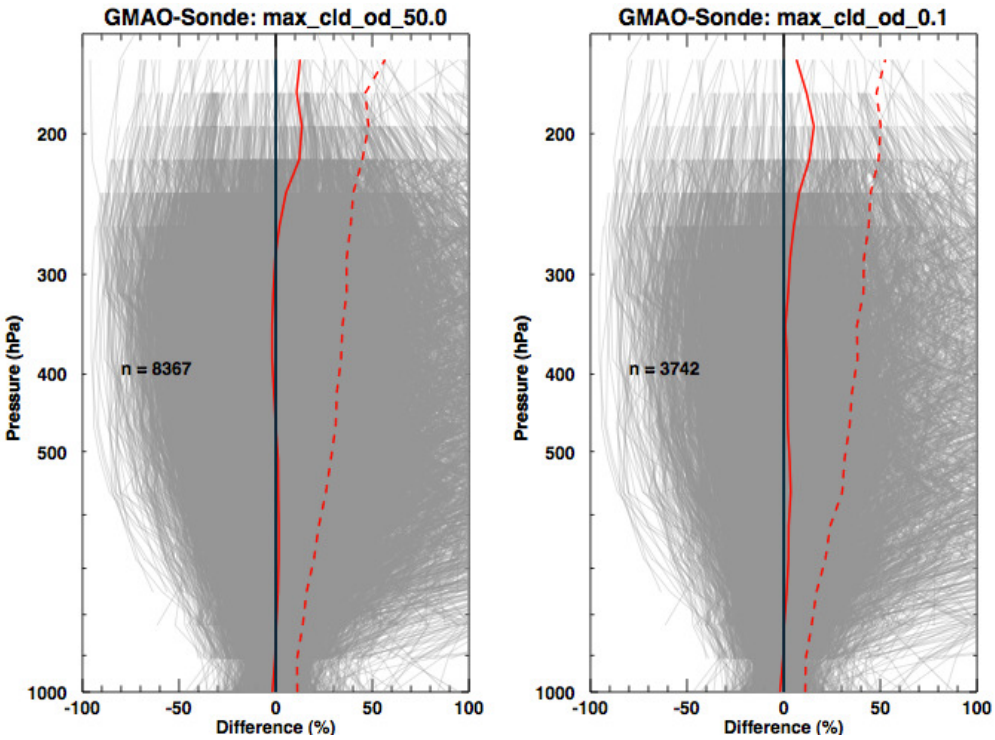

Figure 9-4 Water vapor percent differences between GMAO GEOS-5 analyses and NOAA ESRL radiosonde profiles within 100 km and -0.5 to +1.5 hours. The rms differences are dominated by spatial variability of water vapor on the scale of tens of km. Similar legend as in Figure 9-2.

Figure 9-2 shows differences between TES and radiosonde water vapor for two ranges of average effective cloud optical depth: 0 to 50 (i.e. all retrievals), and 0 to 0.1 (clear sky to optically thin clouds). On average, there is very little difference: both plots show similar rms differences (dashed red line) and bias (solid red line). There is a wet bias in the lower troposphere (1000-900 hPa), a small dry bias < 10 % at 900-600 hPa, and a 10% wet bias in the middle and upper troposphere (600-200 hPa). The bias is slightly smaller for the 0 to 50 cloud optical depth due to the contribution of very cloudy scenes with low information content (i.e. the TES profile mostly reverts back to the a priori value). Figure 9-3 shows differences between TES and GMAO GEOS-5 for the same ranges of average effective cloud optical depth. Bias is very similar in Figure 9-2 and Figure 9-3, indicating that on average GEOS-5 is a good representation of the state of the atmosphere. Figure 9-4 compares GEOS-5 with the NOAA ESRL radiosondes to demonstrate the small bias and residual rms. This rms is due to the spatial variability of atmospheric water vapor on small scales (tens of km).

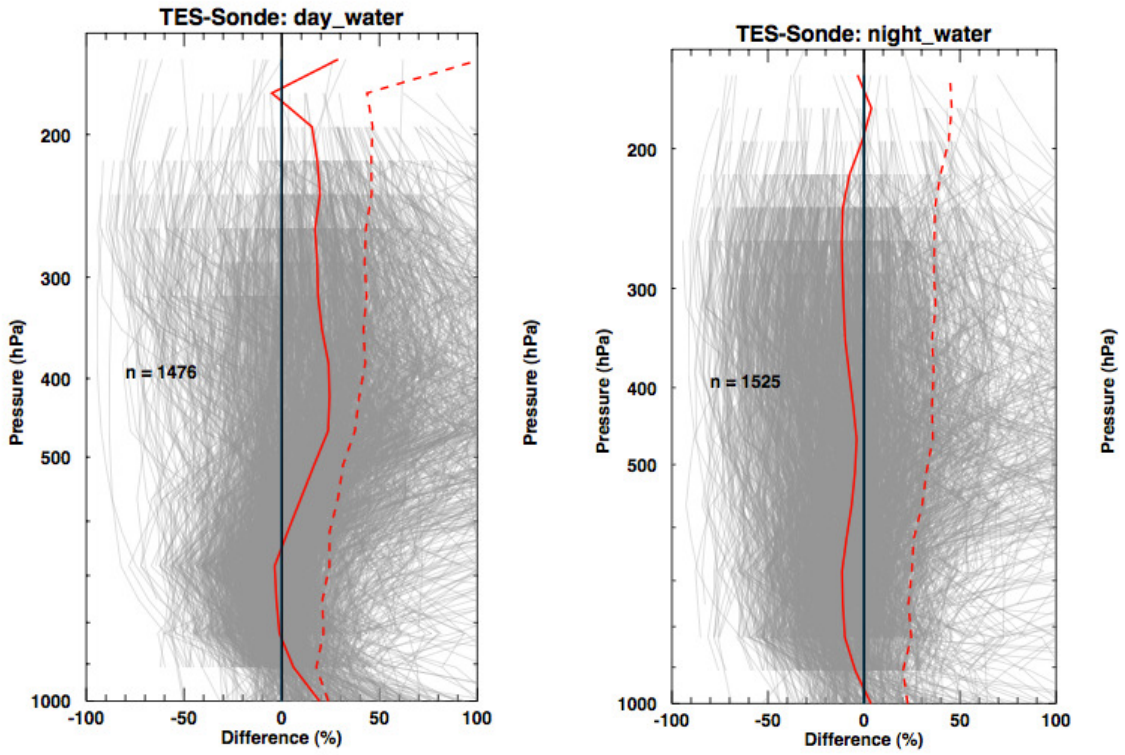

Figure 9-5 Water vapor percent differences between TES V004 and radiosondes in the NOAA ESRL database within 100 km and -0.5 to +1.5 hours. Left: Oceanic comparisons during local daytime shows a bias between TES and radiosondes. Right: Oceanic comparisons during local nighttime have significantly smaller bias. Similar legend to Figure 9-2.

Significant differences are seen between day and night, and retrievals over land and day. Figure 9-5 contrasts TES-radiosonde oceanic differences for day (left) and night (right). The large daytime bias is a well-known systematic bias in radiosonde retrievals [L. Miloshevich, pers. comm.]. When TES is compared to GMAO GEOS-5, it is seen that the daytime bias is smaller (Figure 9-6). For retrievals over land (Figure 9-7), TES versus radiosonde is similar to Figure 9-5. The nighttime land bias is approximately 15%, TES drier than radiosonde.

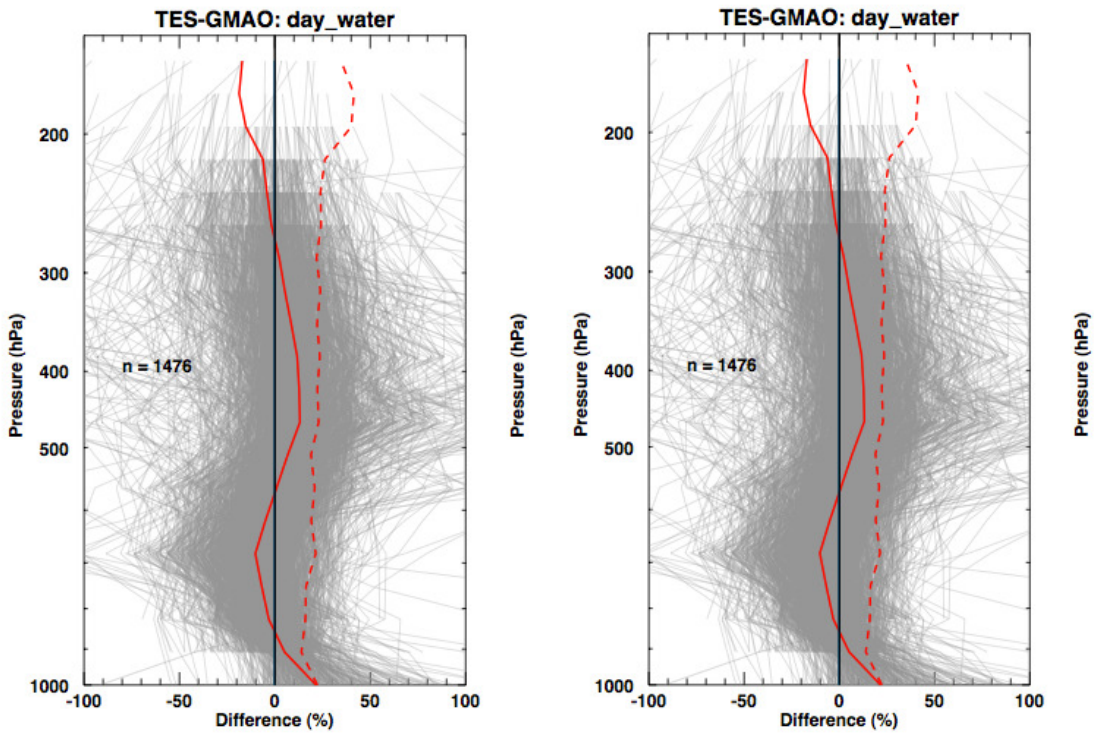

Figure 9-6 Water vapor percent differences between GMAO GEOS-5 and radiosondes in the NOAA ESRL database. Left: Oceanic comparisons during local daytime have a smaller bias than Figure 9-5. Right: Oceanic comparisons during local nighttime.

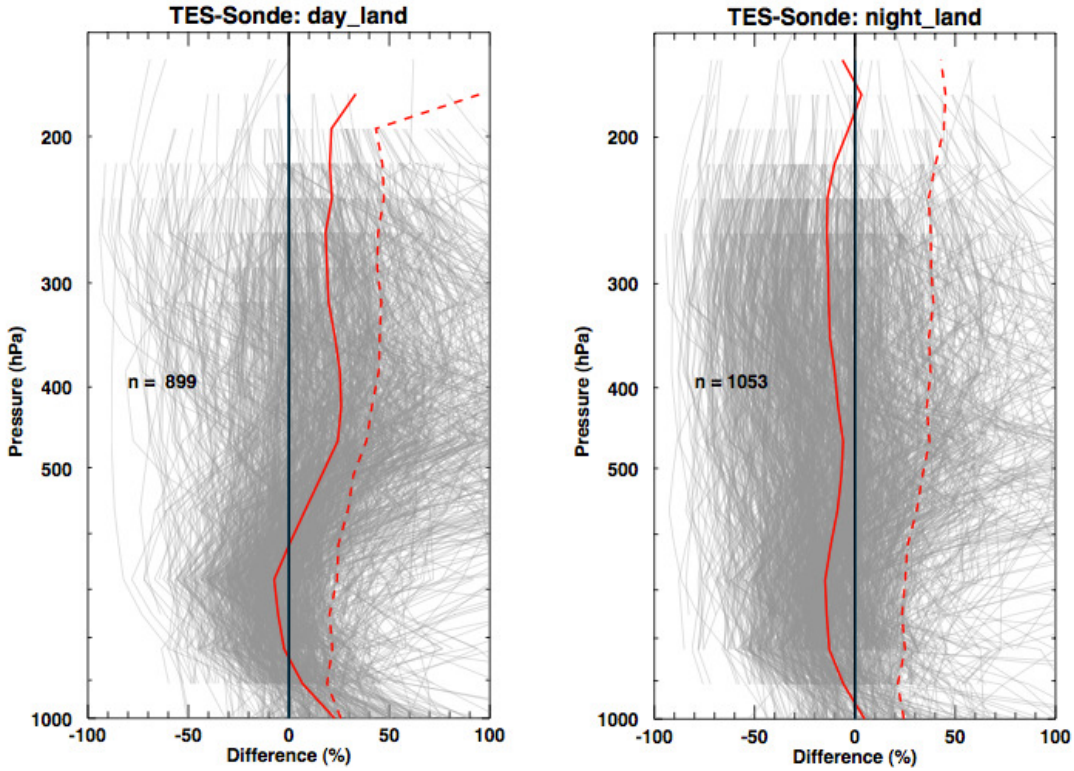

Figure 9-7 Water vapor percent differences between TES V004 and radiosondes in the NOAA ESRL database within 100 km and -0.5 to +1.5 hours. Left: Land comparisons during local

daytime shows a bias between TES and radiosondes. Right: Land comparisons during local nighttime have significantly smaller bias. Similar legend to Figure 9-2.

Next, we look at nighttime comparisons as a function of latitude. Figure 9-8 divides the nighttime comparisons into six latitude bands: Antarctic (90 S to 60 S), Southern (60 S to 15 S), Tropics (15 S to 15 N), Northern Subtropics (15 N to 35 N), Northern Midlatitudes (35 N to 56 N), and Arctic (56 N to 90 N). TES has a small dry bias (0 to 15%) in Northern Midlatitudes and High Latitudes. In the tropics and subtropics, TES appears to have a wet bias, but this may be an artifact of a small number of comparisons. To further examine the different latitudes, we compare TES with GMAO GEOS-5 (Figure 9-9).

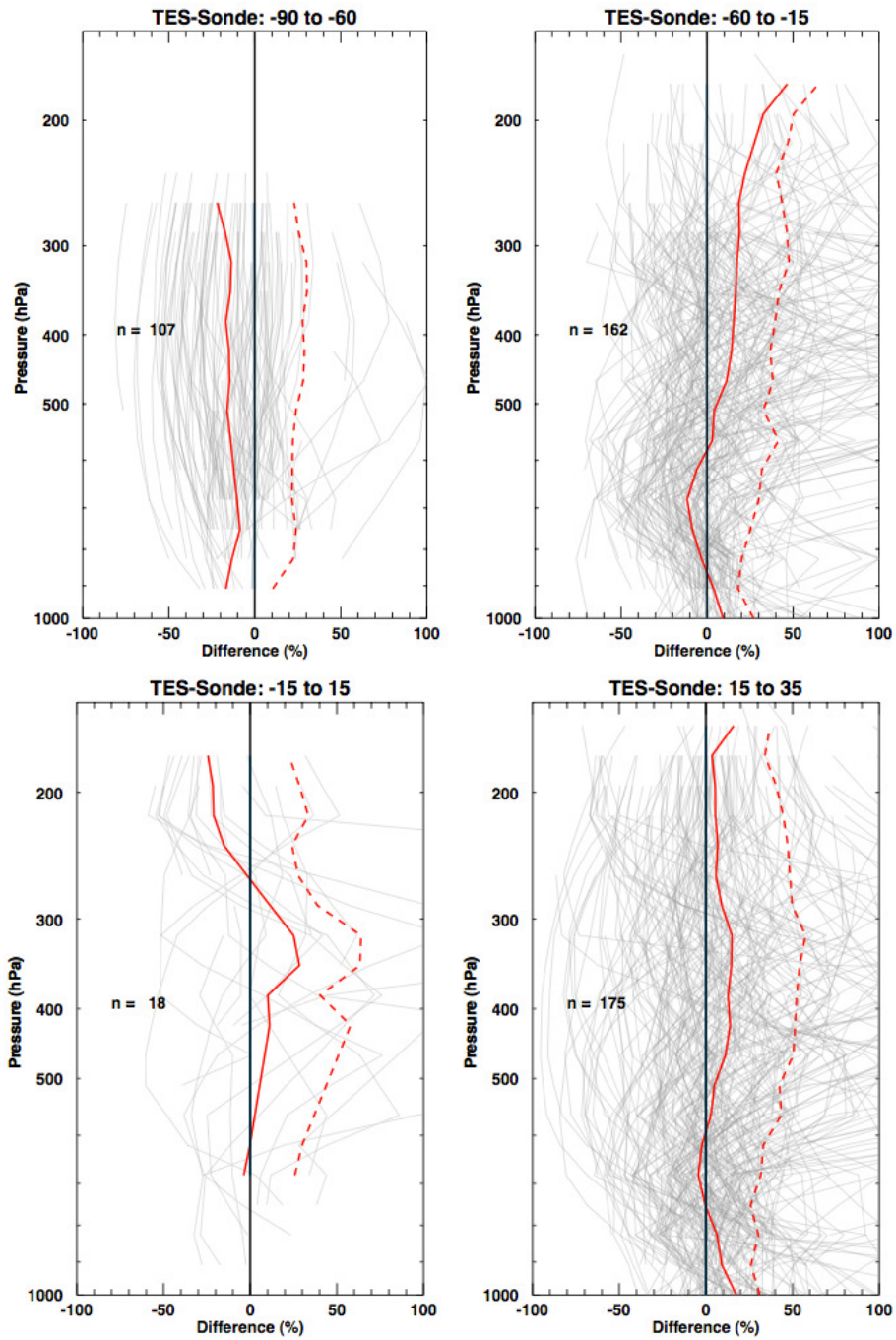

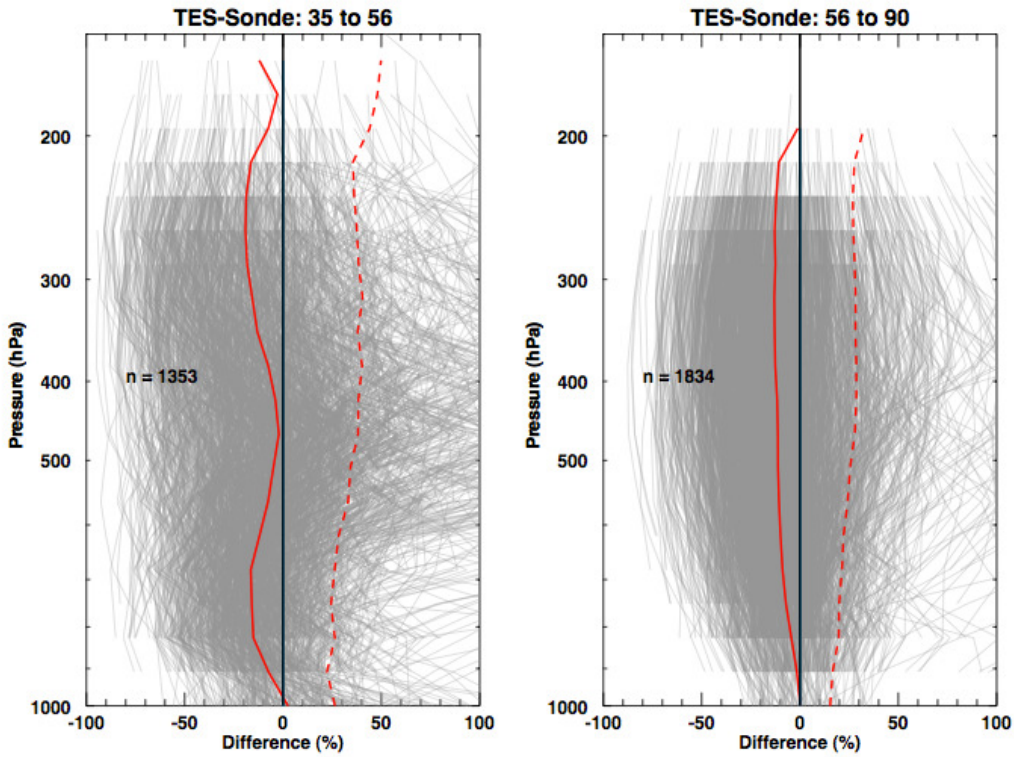

Figure 9-8 Nighttime water vapor percent differences between TES V004 and radiosondes in the NOAA ESRL database by latitude zone.

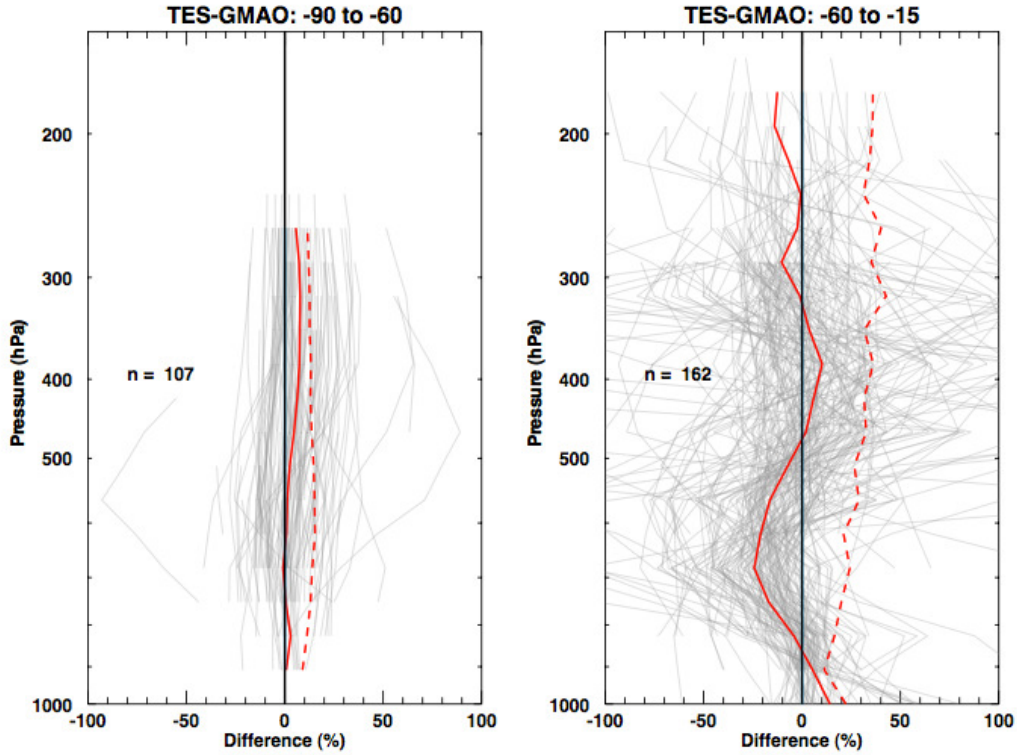

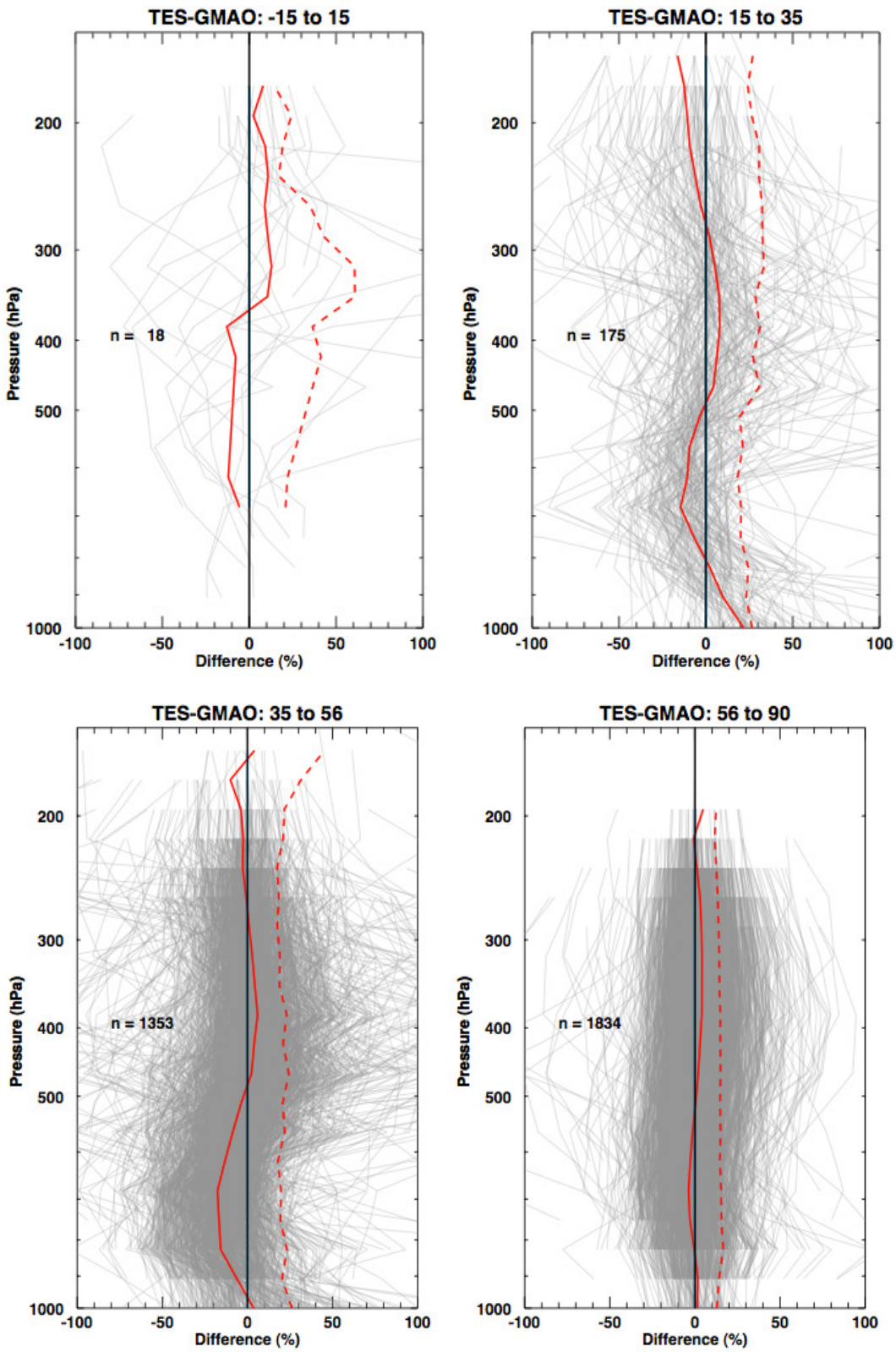

Figure 9-9 Nighttime water vapor percent differences between GMAO GEOS-5 and radiosondes in the NOAA ESRL database by latitude zone.

9.4 Executive Summary

Comparisons have been made between TES V004 water vapor profiles and radiosonde profiles for five years of data (2004-2008). At nighttime, TES has a slight dry bias of 0 to 15% compared to radiosondes, especially in the lower troposphere at 700-800 hPa. The rms differences tend to increase from 20% near the surface to 40% in the upper troposphere.

9.5 References

9.5.1 TES References

[1] Bowman K. W., C. D. Rodgers, S. S. Kulawik, J. Worden, E. Sarkissian, G. Osterman, T. Steck, M. Lou, A. Eldering, M. Shephard, H. Worden, M. Lampel, S. A. Clough, P. D. Brown, C. P. Rinsland, M. Gunson, and R. Beer (2006), Tropospheric emission spectrometer: Retrieval method and error analysis, *IEEE Transactions on Geoscience and Remote Sensing, 44(5)*, 1297-1307, May 2006.

[2] Clough, S. A., M. W. Shephard, E. J. Mlawer, J. S. Delamere, M. J. Iacono, K. Cady-Pereira, S. Boukabara, and P. D. Brown (2005), Atmospheric radiative transfer modeling: a summary of the AER codes, Short Communication, *J. Quant. Spectrosc. Radiat. Transfer, 91, Issue 2,* 233-244, (doi:10.1016/j.jqsrt.2004.05.058) March 1, 2005.

[3] Clough, S. A., M. W. Shephard, J. Worden, P. D. Brown, H. M. Worden, M. Lou, C. D. Rodgers, C. P. Rinsland, A. Goldman, L. Brown, S. S. Kulawik, A. Eldering, M. Lampel, G. Osterman, R. Beer, K. Bowman, K. E. Cady-Pereira, and E. J. Mlawer (2006), Forward Model and Jacobians for Tropospheric Emission Spectrometer Retrievals, *IEEE Transactions on Geoscience and Remote Sensing, 44 (No.5),* Special Issue on Aura, 1308–1323, May 2006.

[4] Eldering, A., S. S. Kulawik, J. Worden, K. Bowman, G. Osterman (2008), Implementation of cloud retrievals for TES Atmospheric retrievals: 2. Characterization of cloud top pressure and effective optical depth retrievals, *Journal of Geophysical Research, Vol. 113,* D16S37, (doi:10.1029/2007JD008858) June 10, 2008.

[5] Gordon, I.E., L. S. Rothman, R. R. Gamache, D. Jacquemart, C. Boone, P. F. Bernath, M. W. Shephard, J. S. Delamere, S. A. Clough (2007), Current updates of water vapor line list in HITRAN: A new "Diet" for air-broadened half-widths, *Journal of Quantitative Spectroscopy & Radiative Transfer, 108,* 389-402, (doi:10.1016/j.jqsrt.2007.06.009), 2007.

[6] Herman, R.L., M. W. Shephard, K. E. Cady-Pereira, V. H. Payne, B. M. Fisher, S. S. Kulawik, G. B. Osterman, A. Eldering, S. Pawson, and D. N. Whiteman, New Comparisons of Tropospheric Emission Spectrometer Version 4 Temperature Retrievals with Radiosonde Measurements, in preparation.

[7] Kulawik S. S., G. Osterman, D. B. A. Jones, and K. W. Bowman (2006a), Calculation of altitude-dependent Tikhonov constraints for TES nadir retrievals, *IEEE Transactions on Geoscience and Remote Sensing, 44 (No.5),* Special Issue on Aura, 1334–1342, May 2006.

[8] Kulawik, S. S., J. Worden, A. Eldering, K. Bowman, M. Gunson, G. B. Osterman, L. Zhang, S. A. Clough, M. W. Shephard, R. Beer (2006b), Implementation of cloud retrievals for Tropospheric Emission Spectrometer (TES) atmospheric retrievals: part 1. Description and characterization of errors on trace gas retrievals, *J. Geophys. Res., 111*, D24204, (doi:10.1029/2005JD006733) December 22, 2006.

[9] Leblanc, T., T. D. Walsh, I. S. McDermid, G. C. Toon, J.-F. Blavier, B. Haines, W. G. Read, B. Herman, E. Fetzer, S. Sander, T. Pongetti, D. N. Whiteman, T. G. McGee, L. Twigg, G. Sumnicht, D. Venable, M. Calhoun, A. Dirisu, D. Hurst, A. Jordan, E. Hall, L. Miloshevich, H. Vömel, C. Straub, N. Kampfer, G. E. Nedoluha, R. M. Gomez, K. Holub, S. Gutman, J. Braun, T. Vanhove, G. Stiller, and A. Hauchecorne (2011), Measurements of Humidity in the Atmosphere and Validation Experiments (MOHAVE)-2009: overview of campaign operations and results, *Atmos. Meas. Tech. Discuss., 4,* 3277–3336, 2011 www.atmos-meas-tech-discuss.net/4/3277/2011/ doi:10.5194/amtd-4-3277-2011.

[10] Osterman, G., (editor), K. Bowman, A. Eldering, B. Fisher, R. Herman, D. Jacob, L. Jourdain, S. Kulawik, M. Luo, R. Monarrez, G. Osterman, S. Paradise, V. Payne, S. Poosti, N. Richards, D. Rider, D. Shepard, M. Shephard, F. Vilnrotter, H. Worden, J. Worden, H. Yun and L. Zhang, Earth Observing System (EOS) Tropospheric Emission Spectrometer (TES) Level 2 (L2) Data User's Guide (Up to & including Version 4 data), Version 4.0, JPL Internal Report D-38042, May 20, 2009.

[11] Shephard, M. W., R.L. Herman, B.M. Fisher, K.E. Cady-Pereira, S. A. Clough, V. H. Payne, D.N. Whiteman, J. P. Comer, H. Vömel, L.M. Miloshevich, Ricardo Forno, M. Adam, G. B. Osterman, A. Eldering, J. R. Worden, L. R. Brown, H. M. Worden, S. S. Kulawik, D. M. Rider, A. Goldman, R. Beer, K. W. Bowman, C. D. Rodgers, M. Luo, C. P. Rinsland, M. Lampel, M. R. Gunson (2008a), Comparison of Tropospheric Emission Spectrometer nadir water vapor retrievals with in situ measurements, *J. Geophys. Res., 113*, D15S24, (doi:10.1029/2007JD008822) May 16, 2008a.

[12] Shephard, M. W., H. M. Worden, K. E. Cady-Pereira, M. Lampel, M. Luo, K. W. Bowman, E. Sarkissian, R. Beer, D. M. Rider, D. C. Tobin, H. E. Revercomb, B. M. Fisher, D. Tremblay, S. A. Clough, G. B. Osterman, and M. Gunson (2008b), Tropospheric Emission Spectrometer Nadir Spectral Radiance Comparisons, *J. Geophys. Res., 113*, D15S05, (doi:10.1029/2007JD008856) April 22, 2008b.

[13] Shephard, M. W., S. A. Clough, V. H. Payne, W. L. Smith, S. Kireev, K. E. Cady-Pereira (2009) Performance of line-by-line radiative transfer model (LBLRTM) for temperature and species retrievals: IASI case studies from JAIVEx, *Atmospheric Chemistry and Physics*, 2009**.**

9.5.2 General References

[14] Bloom, S., A. da Silva, D. Dee, M. Bosilovich, J.-D. Chern, S. Pawson, S. Schubert, M. Sienkiewicz, I. Stajner, W.-W. Tan, M.-L. Wu (2005). Documentation and Validation of the Goddard Earth Observing System (GEOS) Data Assimilation System - Version 4. *Technical Report Series on Global Modeling and Data Assimilation 104606, Vol. 26,* 187 pages, April 2005. Available from (paste entire link including pdf into browser):

http://ntrs.nasa.gov/archive/nasa/casi.ntrs.nasa.gov/20050175690_2005173043.pdf

[15] Divakarla, M. G., C. D. Barnet, M. D. Goldberg, L. M. McMillin, E. Maddy, W. Wolf, L. Zhou and X. Liu (2006), Validation of Atmospheric Infrared Sounder temperature and water vapor retrievals with matched radiosonde measurements and forecasts, J. Geophys. Res., 111, D09S15, (doi:10.1029/2005JD006116) April 6, 2006.

[16] Miloshevich, L. M., A. Paukkunen, H. Vömel, and S. J. Oltmans (2004), Development and Validation of a Time-Lag Correction for Vaisala Radiosonde Humidity Measurements, *Journal of Atmospheric and Oceanic Technolology, 21,* 1305-1327, September 2004.

[17] Miloshevich, L. M., H. Vömel, D. N. Whiteman, B. M. Lesht, F. J. Schmidlin, and F. Russo (2006), Absolute accuracy of water vapor measurements from six operational radiosonde types launched during AWEX-G and implications for AIRS validation, *J. Geophys. Res., 111*, (D09S10, doi:10.1029/2005JD006083) 2006.

[18] Miloshevich, L. M., H. Vömel, D. N. Whiteman, and T. Leblanc (2009), Accuracy assessment and correction of Vaisala RS92 radiosonde water vapor measurements, *J. Geophys. Res., 114,* D11305, doi:10.1029/2008JD011565.

[19] Rienecker, M. M., M. J. Suarez (editor), R. Todling, J. Bacmeister, L. Takacs, H.-C. Liu, W. Gu, M. Sienkiewicz, R. D. Koster, R. Gelaro, I. Stajner and J.E. Nielson (2008), The GEOS-5 Data Assimilation System- Documentation of Versions 5.0.1, 5.1.0, and 5.2.0 *NASA Technical Report Series on Global Modeling and Data Assimilation 104606, Vol.27.*, December 2008.

[20] Rothman, L. S, A. Barbe, D. C. Benner, L. R. Brown, C. Camy-Peyret, M. R. Carleer, K. Chance, C. Clerbaux, V. Dana, V. M. Devi, A. Fayt, J.-M. Flaud, R. R. Gamache, A. Goldman, D. Jacquemart, K.W. Jucks, W.J. Lafferty, J.-Y. Mandin, S. T. Massie, V. Nemtchinov, D. A. Newnham, A. Perrin, C. P. Rinsland, J. Schroeder, K. M. Smith, M. A. H. Smith, K. Tang, R. A. Toth, J. Auwera Vander, P. Varanasi, and K. Yoshino (2003), The HITRAN molecular spectroscopic database: edition of 2000 including updates through 2001*, Journal of Quantitative Spectroscopy and Radiative Transfer, Vol. 82, Number 1*, 5-44, November 2003.

[21] Smith, W. L. (1991), Atmospheric soundings from satellites - false expectation or the key to improved weather prediction?, *Quarterly Journal of the Royal Meteorological Society, Vol 117, Issue 498*, 267-297, (DOI: 10.1256/smsqj.49801) 1991.

[22] Tobin, D. C., H. E. Revercomb, R. O. Knuteson, B. M. Lesht, L. L. Strow, S. E. Hannon, W. F. Feltz, L. A. Moy, E. J. Fetzer, and T. S. Cress (2006), Atmospheric Radiation Measurement site atmospheric state best estimates for Atmospheric Infrared Sounder temperature and water vapor retrieval validations, *J. Geophys. Res., 111,* D09S14, (doi:10.1029/2005JD006103) March 16, 2006.

[23] Vömel, H., D. E. David, and K. Smith (2007), Accuracy of tropospheric and stratospheric water vapor measurements by the cryogenic frost point hygrometer : Instrumental details and observations, *J. Geophys. Res., 112*, D08305, (doi:10.1029/2006JD007224) April 20 2007.

[24] Whiteman, D. N., F. Russo, B. Demoz, L. M. Miloshevich, I. Veselovskii, S. Hannon, Z. Wang, H. Vömel, F. Schmidlin, B. Lesht, P. J. Moore, A. S. Beebe, A. Gambacorta, C. Barnet (2006), Analysis of Raman lidar and radiosonde measurements from the AWEX-G field campaign and its relation to Aqua validation*, J. Geophys. Res., 111,* D09S09, (doi:10.1029/2005JD006429) April 12, 2006.

[25] Zhu, Y., and R. Gelaro (2008), Observation Sensitivity Calculations Using the Adjoint of the Gridpoint Statistical Interpolation (GSI) Analysis System, *Monthly Weather Review, Volume 136, Issue 1*, pp. 335-351, (DOI:10.1175/MWR3525.1) January 2008 - available from http://gmao.gsfc.nasa.gov/pubs/ref/archive/ref_2008.php.

10. HDO/H_2O

10.1 Executive Summary for HDO/H_2O ratio validation

TES is capable of measuring the HDO/H_2O ratio in the troposphere using thermal infrared radiances between 1200 and 1350 cm^{-1}. Information on the simultaneous retrieval of HDO and H_2O is provided in Worden et al., (2006), including a description of error characterization and vertical sensitivities. The TES measurement of HDO is made in the nadir mode and is most sensitive in the region between 450 and 825 hPa.

From October 11 through November 5 2008, we undertook a validation campaign of the TES water isotope measurements. This Validation of V003 of the TES HDO/H_2O ratio is performed using direct and indirect comparisons of TES measurements over and near the Hawaii Mauna Loa observatory in conjunction with flask measurements at Mauna Loa taken by University of New Mexico and high speed data using cavity ring laser measurements from JPL (Lance Christenson PI, ref: Webster and Heymsfield (2003)) and from Los Gatos Research and Picarro that was lent to the University of Colorado and University of New Mexico (David Noone and Joe Galewsky PI). The objective is to better characterize the bias expected in TES HDO/H_2O estimates (Worden et al., 2006).

These comparisons, as discussed in the next sections indicate that the TES HDO/H_2O profiles for V003 need to be adjusted by approximately 6%, accounting for the TES sensitivity of the measurement. As discussed in the next section and in (Worden et al., 2011) the form for the correction should be:

$$\ln(\mathbf{q}^{HDO}_{corrected}) = \ln(\mathbf{q}^{HDO}_{original}) - \mathbf{A}(\vec{\delta}_{bias}) \qquad \textbf{(10-1)}$$

where $\mathbf{q}^{HDO}_{original}$ is the volume mixing ratio of the HDO profile as provided in the product files, A is the averaging kernel matrix (also provided in the product files), and $\vec{\delta}_{bias}$ is a column vector of the same length as $\mathbf{q}^{HDO}_{original}$ that contains the values 0.06. Note that this correction is only applied to HDO and not to H_2O. For this release, this correction should be applied by the user of the data. For Release 2, we recommend that the user apply a value of 0.045. The difference between the two releases is due to a change in how temperature is estimated in the TES retrievals.

10.2 In Situ Data Sets

Figure 10-1 shows a comparison of in situ measurements of flask measurements, e.g., Galewsky et al., (2007) as well as high speed in situ measurements form the JPL ALIAS instrument, e.g., Webster and Heymsfeld, (2003), and the Picarro instrument. At this time, we do not have the calibrated Los Gatos Research data; this data will be shown when it is made available. The flask measurements at Mauna Loa, where water concentrations are low, were contaminated during the measurement as evidence by the discrepancy between the flask measurements, JPL, and Picarro. However, the flask data agree well with the higher concentration, less depleted water vapor samples. The JPL data are only available for the first 5 days of the validation campaign and only overlapped one overpass of the Aura satellite. However, the good agreement between the JPL

data and Picarro data, especially at very low isotope values, give us confidence that we can utitlize the Picarro data over the whole time series extending from October 11 through November 5 2008.

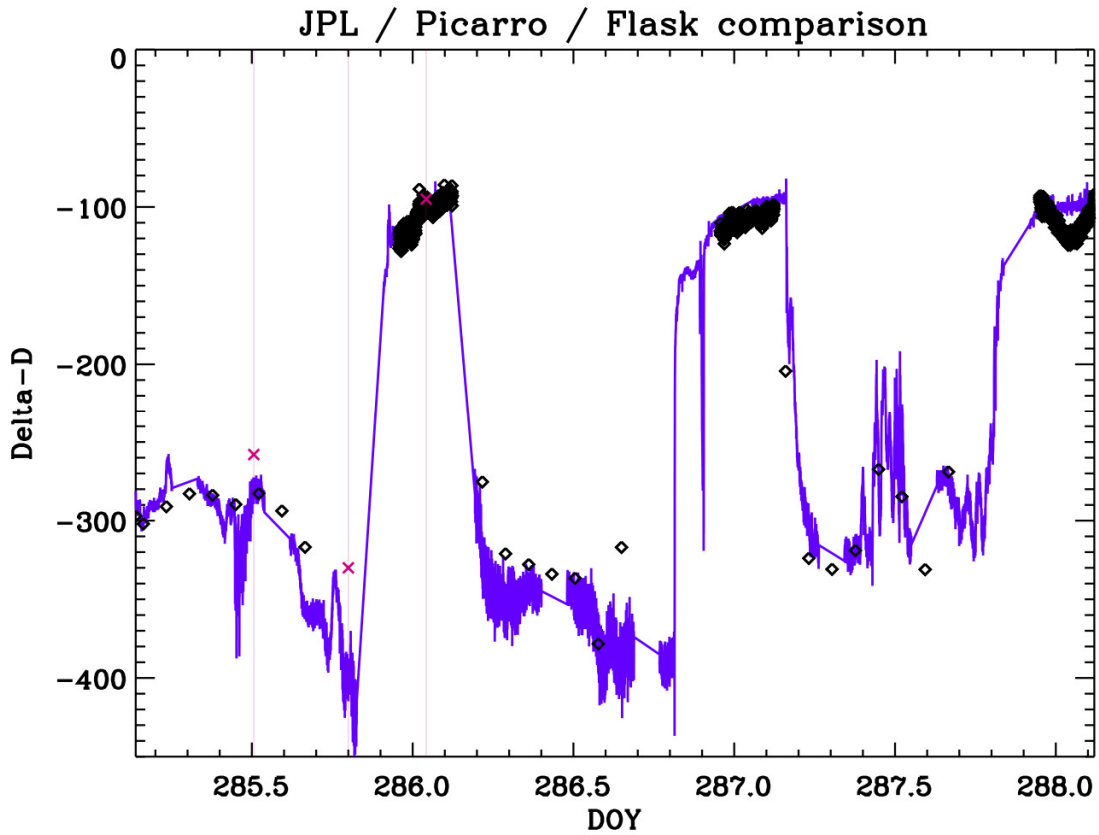

Figure 10-1 Comparison of Flask (red x with vertical lines), JPL ALIAS instrument (black diamonds), and Picarro (purple line).

10.3 Direct Comparison of TES satellite profile data to in situ data

In this section we compare a TES profile measurement of the HDO/H_2O ratio to constructed profile of the HDO/H_2O ratio using the Mauna Loa data. This comparison must account for the sensitivity of the TES HDO/H_2O measurement to the true distribution of the HDO/H_2O ratio and to the a priori constraint used in the retrieval (e.g., Worden et al., 2006).

The comparison follows the approach described by H. Worden et al. (2007), for the TES ozone profiles except that we must account for the cross correlations in the joint HDO/H_2O profile retrieval used operationally by the TES algorithm, e.g.:

$$\hat{\mathbf{x}}_R = \mathbf{x}_a^R + (\mathbf{A}_{\mathbf{DD}} - \mathbf{A}_{\mathbf{HD}})(\mathbf{x}_D - \mathbf{x}_a^D) - (\mathbf{A}_{\mathbf{HH}} - \mathbf{A}_{\mathbf{DH}})(\mathbf{x}_H - \mathbf{x}_a^H) \quad (10\text{-}2)$$

Where, $\mathbf{A_{DD}}$ and $\mathbf{A_{HH}}$ are the averaging kernel matrices for HDO and H_2O separately (available in the individual product files for those species). The $\mathbf{A_{HD}}$ and $\mathbf{A_{DH}}$ are the cross averaging kernels between HDO and H_2O and the reverse, available in the Ancillary product files. Note that the averaging kernels are not symmetric so one cannot use one cross term for the other. The $\mathbf{x_D}$, $\mathbf{x_H}$, are the "true" distribution of HDO and H_2O respectively and are represented as the log of the concentration of each species (given in volume mixing ratio). The $\mathbf{x_a}$ is the a priori constraint vector for each species (available in the product files).

After passing the true HDO and H_2O and constraint vector profiles through the averaging kernels, the "true" HDO/H_2O ratio (or actually log[HDO/H_2O]), $\hat{\mathbf{x}}_R$, will have been adjusted to account for the sensitivity of the TES estimate to HDO and H_2O and also to the bias introduced into the retrieval via the constraint vector that is used to regularize the retrieval. As shown in H. Worden et al., (2007) for the TES ozone retrievals, and in Worden et al., (2006) for the HDO/H_2O retrievals, the difference between this modified "true" ratio and the measurement from TES is due to any un-quantified biases in the TES data as well as the measurement uncertainty due to noise and also due to other geophysical parameters that affect the TES HDO/H_2O retrieval such as temperature, emissivity, and clouds. As shown in Worden et al., (2006), these combined errors are described

$$\mathbf{S_{obs}} = \mathbf{S_{meas}} + \sum_{\mathbf{i}} \mathbf{S}_i^{\text{int}} \qquad \textbf{(10-3)}$$

where $\mathbf{S_{meas}}$ is the measurement error and the summation, $\sum_{\mathbf{i}} \mathbf{S}_i^{\text{int}}$, is the sum of all interfering parameters such as temperature and clouds affecting the retrieval. These covariance matrices are also present and the product files. The sum of these errors for the ratio is:

$$\mathbf{S_R} = \mathbf{S_{HDO}} + \mathbf{S_{H2O}} - 2\mathbf{S_{HDO_H2O}} \qquad \textbf{(10-4)}$$

where $\mathbf{S_{HDO}}$ is the covariance for HDO (measurement, total, or observation) and $\mathbf{S_{H2O}}$ is the covariance for water; these covariances are given for measurement, total, and observation errors in the individual product files. The cross term covariance, $\mathbf{S_{HDO_H2O}}$, is located in the ancillary products file and begins with the parameter name "HDO_H2ORatio". Unlike the averaging kernel matrix, the covariance matrices are all symmetric.

The next step is to construct a "true" HDO profile and a "true" H_2O profile as used in Equation (10-2). This HDO/H_2O profile is constructed using the high speed in situ measurements and the TES H_2O profile, corroborated by local rawinsonde data from Hawaii. We have used the U. of Wyoming resource to obtain sounding information (http://weather.uwyo.edu/upperair/sounding.html). We construct the "true" HDO/H_2O profile for November 5, 2008 in the following manner.

1) Obtain in situ HDO and H_2O data corresponding to satellite overpass. An example of these data from the Picarro instrument for November 5 is shown in Figure 10-1.
2) Map TES or rawinsonde H_2O data at each pressure level (Figure 10-2) to the in situ data (shown as dotted lines in Figure 10-2). Note that in this instance only the first 5 pressure

levels can be used because H_2O amounts at the lower pressures are not measured by the Picarro instrument. This makes the assumption that the observed air parcel observed over the day by the in situ device is representative of the observed air parcel measured at a single time by TES.

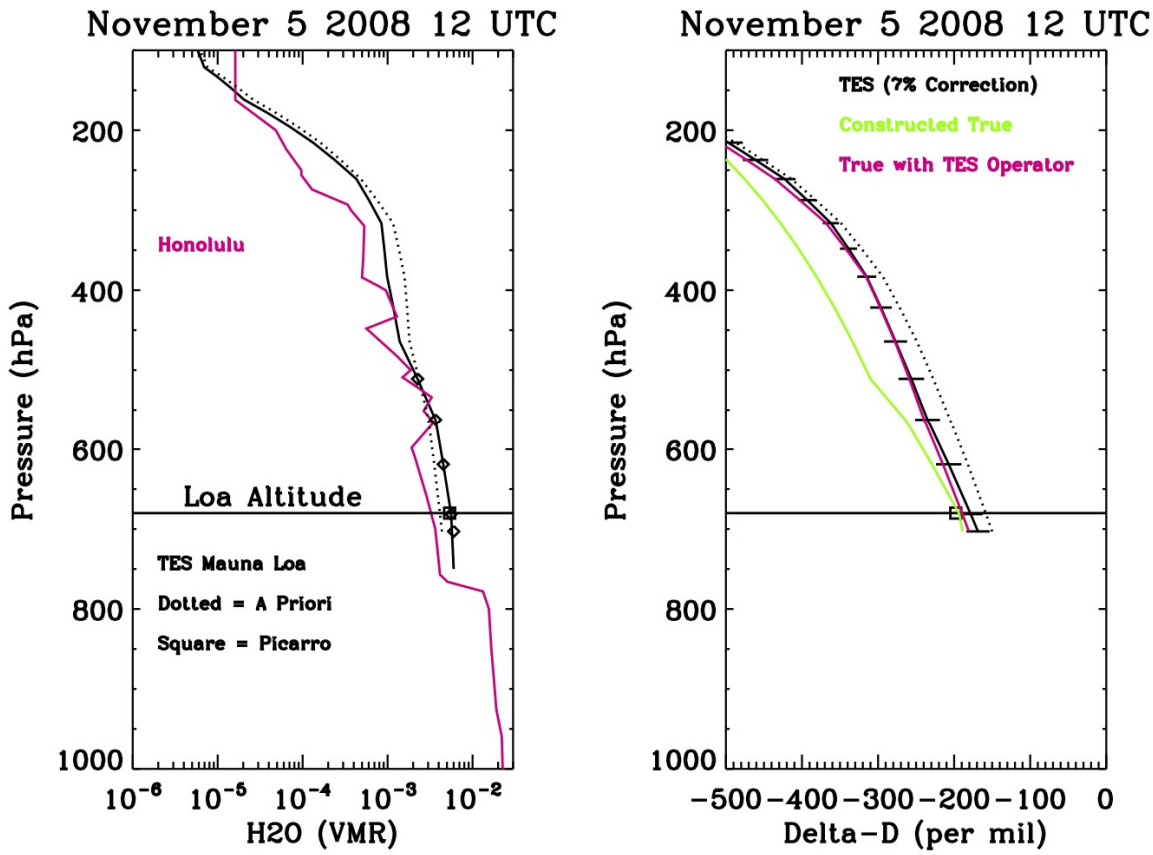

Figure 10-2 Left Panel TES and rawinsonde H_2O. The diamonds are the first 5 pressure levels in the TES H_2O profile used to construct the delta-D profile. Right Panel: The TES delta-D profile (corrected for bias), the a priori constraint and the constructed "true" delta-D profile. The error bars are due to measurement and interfering geophysical parameters.

3) Average all delta-D values where the TES and in situ H_2O values agree to within 5%; these delta-D values for the first five pressure levels correspond to the dotted lines in the bottom of Figure 10-3. As seen in Figure 10-4, the first 5 pressure levels span almost all the pressure levels where the HDO estimate is most sensitive as indicated by the HDO averaging kernel matrix.

4) Construct the delta-D profile using values from these pressure levels and interpolated to the value for the a priori constraint vector at 200 hPa.

5) Calculate the "true" HDO profile using the H_2O profile from Figure 10-2 and the true delta-D profile from Figure 10-2. It does not matter whether the H_2O profile comes from the rawinsonde or TES data due to the cross-correlations in the averaging kernels. It is only necessary to have an independent HDO/H_2O profile for the comparison.

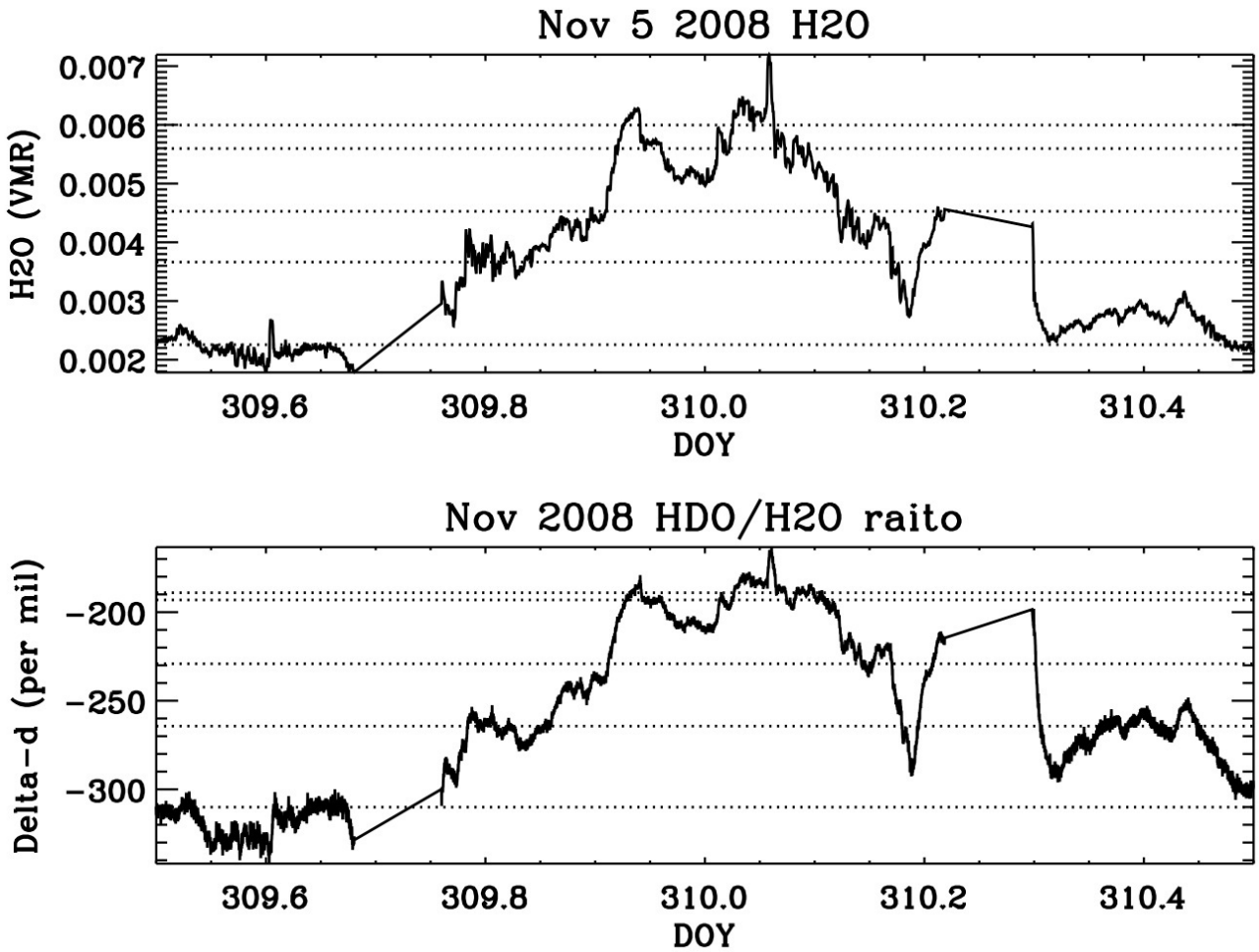

Figure 10-3 In Situ H_2O and Delta-D valus for Nov 5 2008. The dotted lines in the top panel correspond to the diamonds overlapping the TES H_2O profile in Figure 10-2 (left panel). The dotted lines in the bottom panel are the chosen delta-D values used to construct the "true" delta-D profile in the lower troposphere.

6) Pass the HDO and H_2O profiles through the combined HDO/H_2O averaging kernel matrix as shown in Equation (10-2). The modified estimate for HDO and H_2O can now be compared to the TES estimate as it accounts for the TES sensitivity and a priori bias; this is shown as the red line in the right panel of Figure 10-2.

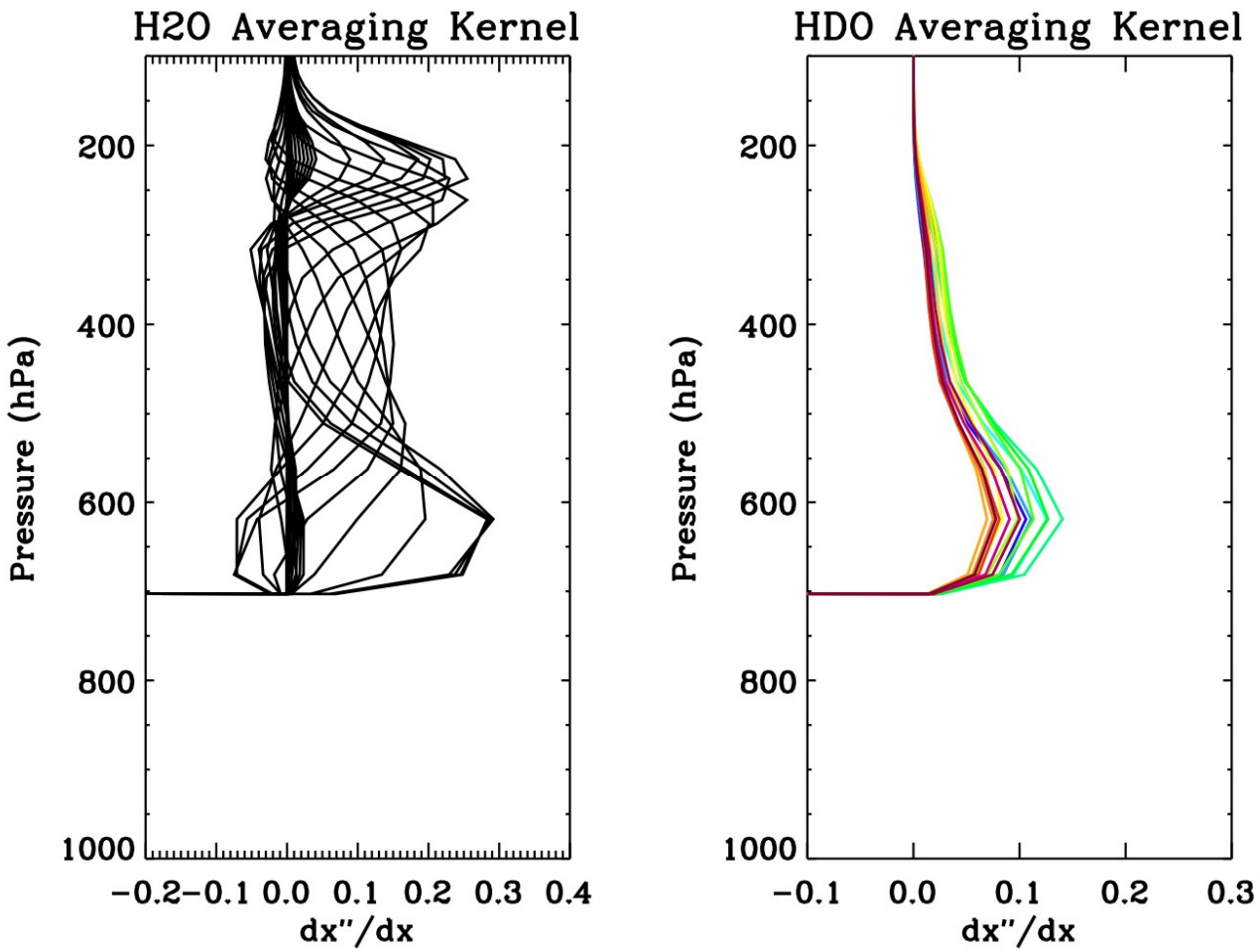

Figure 10-4 Rows of the individual averaging kernel matrices for H_2O (left panel) and HDO (right panel)

The November 5 2008 comparison is shown as it is the only overpass of the five during this validation campaign that was directly over Mauna Loa and the estimate had sufficient sensitivity to make the comparison meaningful. This comparison shows that a correction factor of 0.07 needs to be applied to the TES HDO profiles using Equation (10-1). The error bars indicate the observation error for this estimate. After the bias correction, the comparison between the modified "true" HDO/H_2O profile agrees within the error bars of the TES estimate.

Of the five overpasses only 4 were usable; these other comparisons needed corrections ranging from 0.03 to 0.06. However these other overpasses had to use averages of several TES observations around Hawaii as the observations directly over Mauna Loa could not be used due to low sensitivity resulting from cloud cover.

10.4 Indirect Comparison of TES data to In situ data

Another method for comparing the TES data to the in situ data is to compare delta-D versus H_2O for a large number of observations. This makes use of the expectation that the free tropospheric

water vapor observed by TES around Hawaii should, on average, have a similar moist process history as the water vapor observed during the night time by the in situ measurements because the night time in situ measurements are representative of the free troposphere. Figure 10-5 shows distributions of delta-D versus H_2O using the in situ measurements from Picarro and all TES data taken during October 2008 that was within 1000 km of Hawaii. Only data where the degrees-of-freedom for signal for HDO is larger than 0.5 is used. Then, the TES HDO profiles are corrected for biases of 0.02, 0.04, 0.06, and 0.07. After this bias correction the HDO/H_2O profiles are constructed and a column average is calculated for each profile using the pressure range between 825 hPa and 464 hPa. These column averages, using the different bias corrections, are then compared to the delta-D versus H_2O distributions from Picarro. The best overall comparison between these different column averages and the night-time Picarro data as seen in Figure 10-5 is for a bias correction factor of 0.06. For this reason, we recommend using a bias correction of 0.06 applied to the TES data as represented in Equation (10-1) in the executive summary.

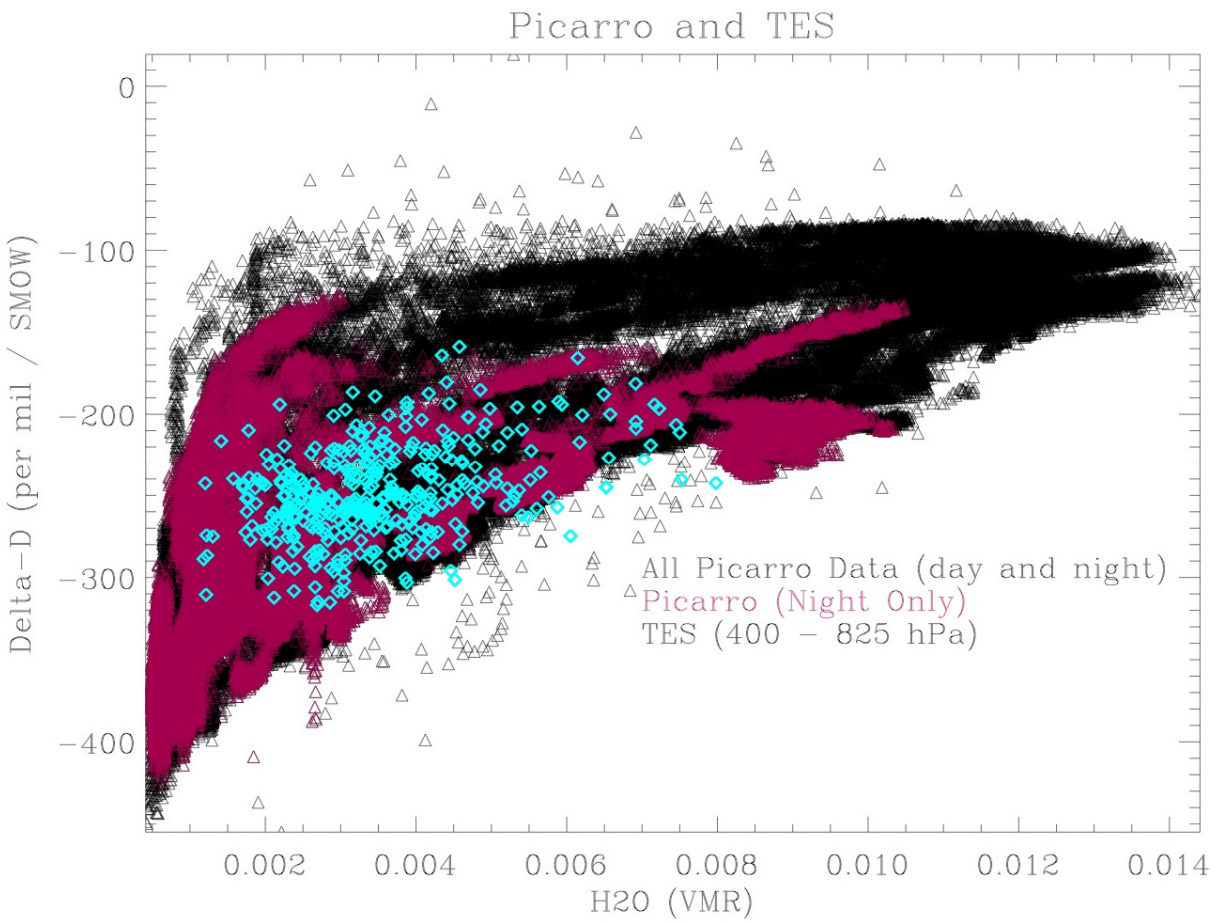

Figure 10-5 Comparison of In Situ data from the Picarro instrument during October 2008 with TES data within 1000 km of Hawaii for the same time period.

10.5 Comparison between V004 and V003

In this section we compare delta-D values between V004 and V003 of the TES isotope data. A significant difference between these versions is that the temperature retrieval strategy was changed in order to obtain improved atmospheric temperatures. Because the spectral absorption lines for both HDO and H_2O are temperature sensitive, this change will impact the HDO and H_2O estimates. Although these changes are likely due to temperature we can partially correct for them using the same approach as described in Equation (10-1). After correcting for a 1.5 percent bias between the versions, the mean difference between versions is reduced from 8.8 parts per mil to -2.2 parts per mil. Note that there is a residual latitudinal difference at higher latitudes because this correction cannot completely account for the differences in the two versions due to the differences in the temperature retrieval.

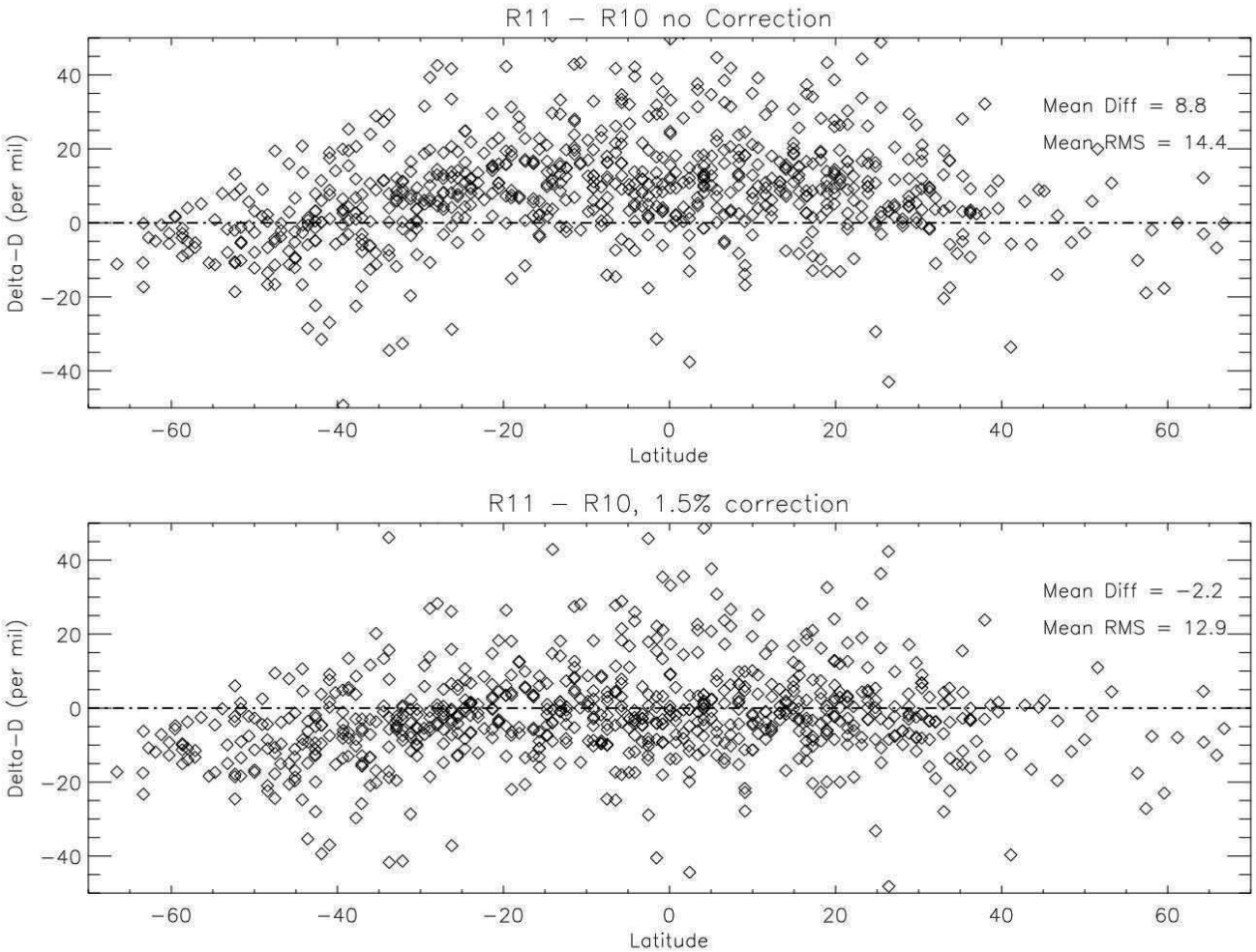

Figure 10-6 Comparison between V003 and V004 of the data before and after correction.

10.6 References

10.6.1 TES HDO/H_2O References

[1] Worden, J., K. Bowman, D. Noone, R. Beer, S. Clough, A. Eldering, B. Fisher, A. Goldman, M. Gunson, R. Herman, S. S. Kulawik, M. Lampel, M. Luo, G. Osterman, C. Rinsland, C. Rodgers, S. Sander, M. Shephard, and H. Worden (2006), Tropospheric Emission Spectrometer observations of the tropospheric HDO/H_2O ratio: Estimation approach and characterization, *Journal of Geophysical Research, 111*, D16309, (doi:10.1029/2005JD006606) August 25, 2006.

[2] Worden, J., D. Noone, K. Bowman & TES science team and data contributors (2007), Importance of rain evaporation and continental convection in the tropical water cycle, *Nature, 445,* 528-532, (doi:10.1038/nature05508) February 1, 2007.

[3] Worden, J., D. Noone, J. Galewsky, A. Bailey, K. Bowman, D. Brown, J. Hurley, S. Kulawik, J. Lee, and M. Strong, Estimate of bias in Aura TES HDO/H2O profiles from comparison of TES and in situ HDO/H2O measurements at the Mauna Loa observatory, *Atmospheric Chemistry and Physics, 11,* 4491–4503, 2011, doi:10.5194/acp-11-4491-2011, May 12, 2011.

10.6.2 TES References

[4] Worden, H. M., J. Logan, J. R. Worden, R. Beer, K. Bowman, S. A. Clough, A. Eldering, B. M. Fisher, M. R. Gunson, R. L. Herman, S. S. Kulawik, M. C. Lampel, M. Luo, I. A. Megretskaia, G. B. Osterman, and M. W. Shephard (2007), Comparisons of Tropospheric Emission Spectrometer (TES) ozone profiles to ozonesondes: Methods and initial results, *J. Geophys. Res., 112*, D03309, (doi:10.1029/2006JD007258), February 15, 2007.

10.6.3 General References

[5] Galewsky, J., M. Strong, and Z. Sharp (2007), Measurements of water vapor D/H ratios from Mauna Kea, Hawaii, and implications for subtropical humidity dynamics, *Geophysical Research Letters, 34,* L22808, (doi:10.1029/2007GL031330), November 21, 2007.

[6] Webster, C. R., and A. J. Heymsfield (2003), Water Isotope Ratios D/H, $^{18}O/^{16}O$, $^{17}O/^{16}O$ in and out of Clouds Map Dehydration Pathways, *Science, Vol. 302, no. 5651,* 1742-1745, (DOI: 10.1126/science.1089496), December 5, 2003.

11. Methane

11.1 Overview of current validation status of TES V004 methane

TES V004 methane has been compared with in-situ aircraft measurements from the Differential Absorption CO measurement (DACOM) instrument for flights during the INTEX-B campaign, with satellite measurements from AIRS (on the Aqua satellite) and with global monthly fields from GEOS-Chem, a global chemical model which has previously been shown to compare well with a range of ground-based and aircraft measurements. Preliminary comparisons have also been performed against data from ground-based FTIR (Fourier Transform Infrared Spectrometer) instruments maintained by the Network for the Detection of Atmospheric Composition Change (NDACC).

TES methane retrievals contain around 1.0 degree of freedom for signal (DOFS) - between ~0.5 in polar regions and 1.4-1.8 in the tropics, depending on season and location. With only one degree of freedom available, attempts to interpret TES methane (or differences between TES methane and some other data source such as model fields or in situ data) on any given one of the 67 Level 2 levels can be misleading. Since methane is relatively well-mixed in the troposphere, the TES methane may be represented by a "representative tropospheric volume mixing ratio" (RTVMR), associated with an effective pressure that describes the location in the atmosphere where most of the retrieval information originates. Further discussion of this quantity can be found in Payne et al. (2009) and in the TES Level 2 Data Users' Guide (Osterman et al., 2009).

11.2 TES/DACOM comparisons

DACOM aircraft measurements provide a reasonable estimate of the true atmospheric methane profile as observed by the TES instrument. Over the course of the INTEX-B campaign in Spring 2006, a number of targeted DC8 flights and TES special observations were made to provide DACOM profile measurements co-incident with TES overpasses, resulting in seventeen matches spanning the latitude range 20N to 60N. The maximum altitude of the DACOM measurements was, in general, between 300 and 200 hPa. TES measurements are generally most sensitive to methane between 400 and 200 hPa. DACOM profiles were extrapolated above the maximum measurement altitude using the TES constraint vector, scaled to match the DACOM measurements at the uppermost measurement altitude. RTVMRs were calculated from the DACOM and TES measurements and the results compared. An example case is shown in Figure 11-1, while a scatter plot of TES and DACOM RTVMRs for all INTEX-B cases is shown in Figure 11-2. Overall, the mean bias of TES RTVMRs with respect to DACOM is +3.7 % and the r.m.s. difference is 4.4 %. It is clear from Figure 11-1 that the TES retrieved methane profiles do not show a realistic profile shape. Since the TES measurement is most sensitive to the mid-upper troposphere, this is the region where the retrieval has the freedom to move away from the a priori. Above and below this region, the values are constrained to the a priori. Figure 11-1 demonstrates the value of looking at RTVMRs rather than at TES methane values from one given pressure level. The TES RTVMR values do broadly capture the large-scale variations in atmospheric methane observed in the DACOM data.

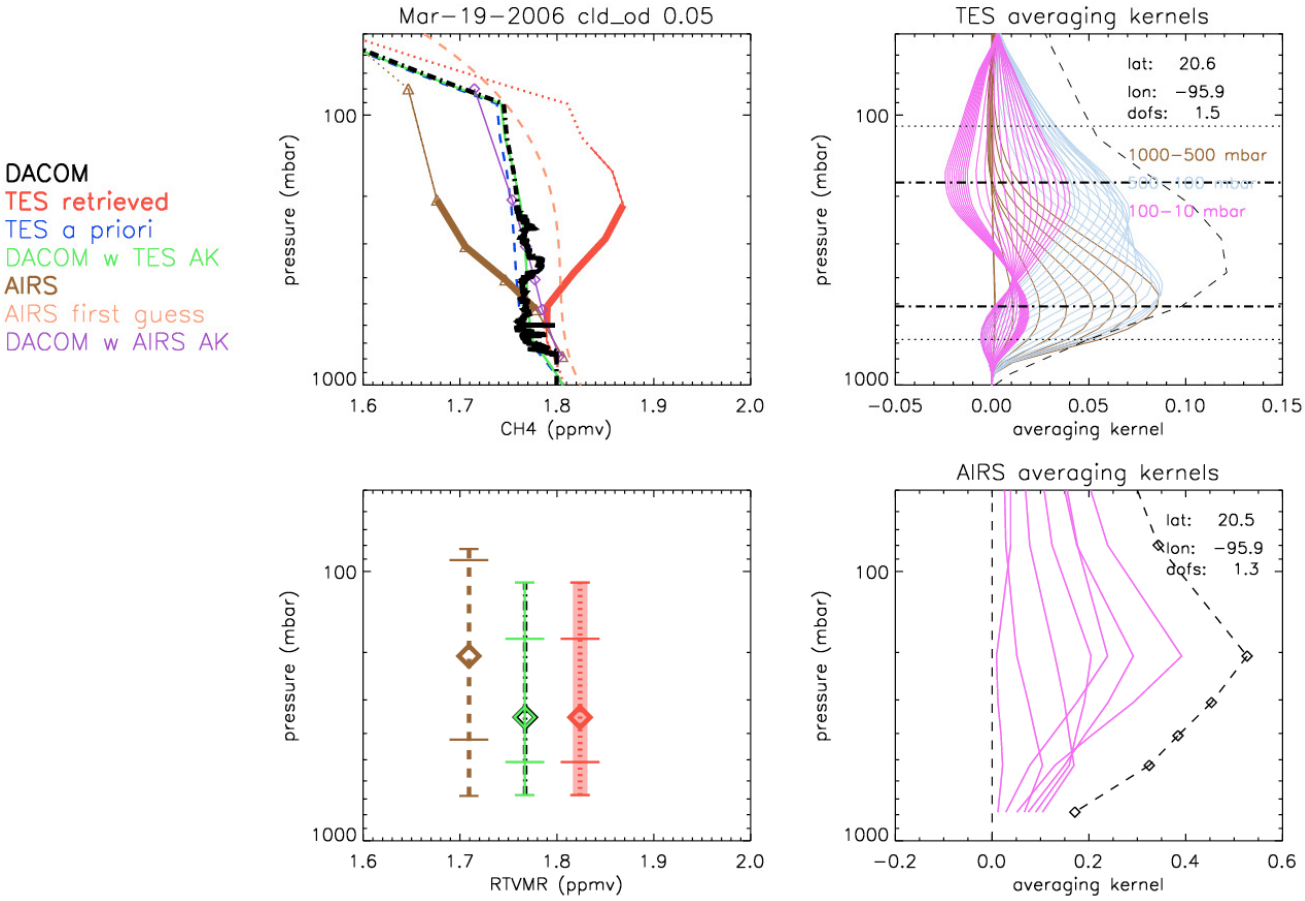

Figure 11-1 Example of TES/DACOM/AIRS comparison during INTEX-B. Top left: measured, retrieved and a priori/initial guess profiles. Thicker parts of TES and AIRS lines show the altitude region where retrievals have greatest sensitivity. Solid part of the DACOM line shows DACOM measurements, while dot-dashed parts of the DACOM line show the region that was extrapolated using the TES a priori constraint vector. Top right: Averaging kernels from the TES methane retrieval. Colored lines show averaging kernels for individual pressure levels while the dashed line shows the profile of the sum of the row of the averaging kernel (scaled by a factor of 0.1). Bottom right: Averaging kernels from the AIRS retrieval. Bottom left: TES, DACOM and AIRS RTVMR values, showing the regions over which the TES and AIRS retrievals have their greatest sensitivity.

The DACOM instrument was also flown on the DC8 aircraft for the ARCTAS campaign during March/April and June/July 2008. Analysis of the ARCTAS data is underway.

11.3 TES/AIRS comparisons

TES V004 RTVMRs have also been compared with AIRS v5.0 retrieved methane values for INTEX-B cases. AIRS and TES are both infrared instruments, and have similar vertical sensitivity for methane, but there are a number of reasons why the retrieved results could differ.

AIRS has lower spectral resolution than TES (~1.0 cm-1 for AIRS in the methane region compared to 0.06 cm-1 for TES). The algorithms for the AIRS and TES use different forward models (Clough et al., 2006; Strow et al., 2006) (absorption coefficients in the AIRS forward model were tuned using tropical aircraft profiles (Xiong et al., 2008)) as well as different retrieval methods (Bowman et al., 2006; Susskind et al.,2003) and different initial guess fields for the retrievals. Since the number of DOFS is slightly lower for AIRS than for TES methane, neither instrument truly yields information about profile shape. AIRS methane values are ~2 % lower than DACOM values (5-6 % lower than TES values). It is likely that a large part of the TES/AIRS difference is due to tuning in the AIRS forward model. Future validation work will involve global scale comparisons of TES and AIRS methane values to determine whether consistent large-scale features are observed in the two methane datasets, and comparisons between TES and SCIAMACHY (Scanning Imaging Absorption Spectrometer for Atmospheric Cartography), which has sensitivity down closer to the surface.

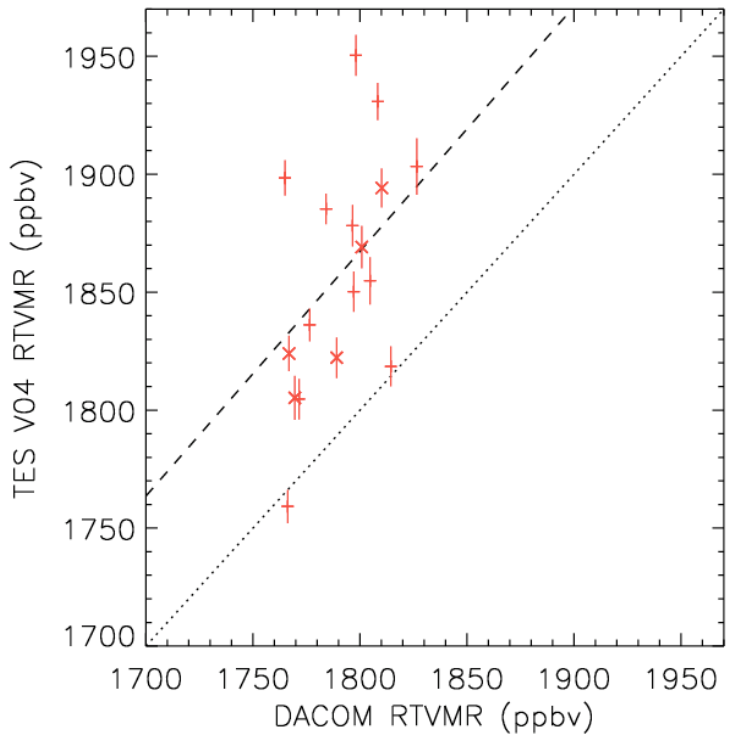

Figure 11-2 Scatter plot of DACOM versus TES RTVMRs for INTEX-B measurements. The dotted line shows the 1:1 relationship, while the dashed line shows the mean high bias in the TES RTVMRs (+3.7 %).

11.4 TES/GEOS-Chem comparisons

GEOS-Chem methane fields for 2001 have been shown to compare well to surface and aircraft data from a wide range of locations (Wang et al., 2004; Xiao et al., 2004). Long-term methane measurements at NOAA surface sites (Dlugokencky et al., 2007) indicate that values for 2005/2006 were very similar to those for 2001. The 2001 GEOS-Chem fields therefore

constitute a valuable additional dataset for evaluation of the TES methane retrievals. Comparisons indicate that the TES measurements are biased high by around 5% with respect to GEOS-Chem monthly mean fields. Differences are largest during the northern hemisphere summer months. Figure 11-3 shows comparisons of TES and GEOS-Chem RTVMR zonal means for July 2005. The GEOS-Chem comparisons provide some confidence that the TES retrievals provide a reasonable representation of the global spatial distribution of methane in the mid-to-upper troposphere. (Further details of TES V003 comparisons with GEOS-Chem may be found in Payne et al., (2009).

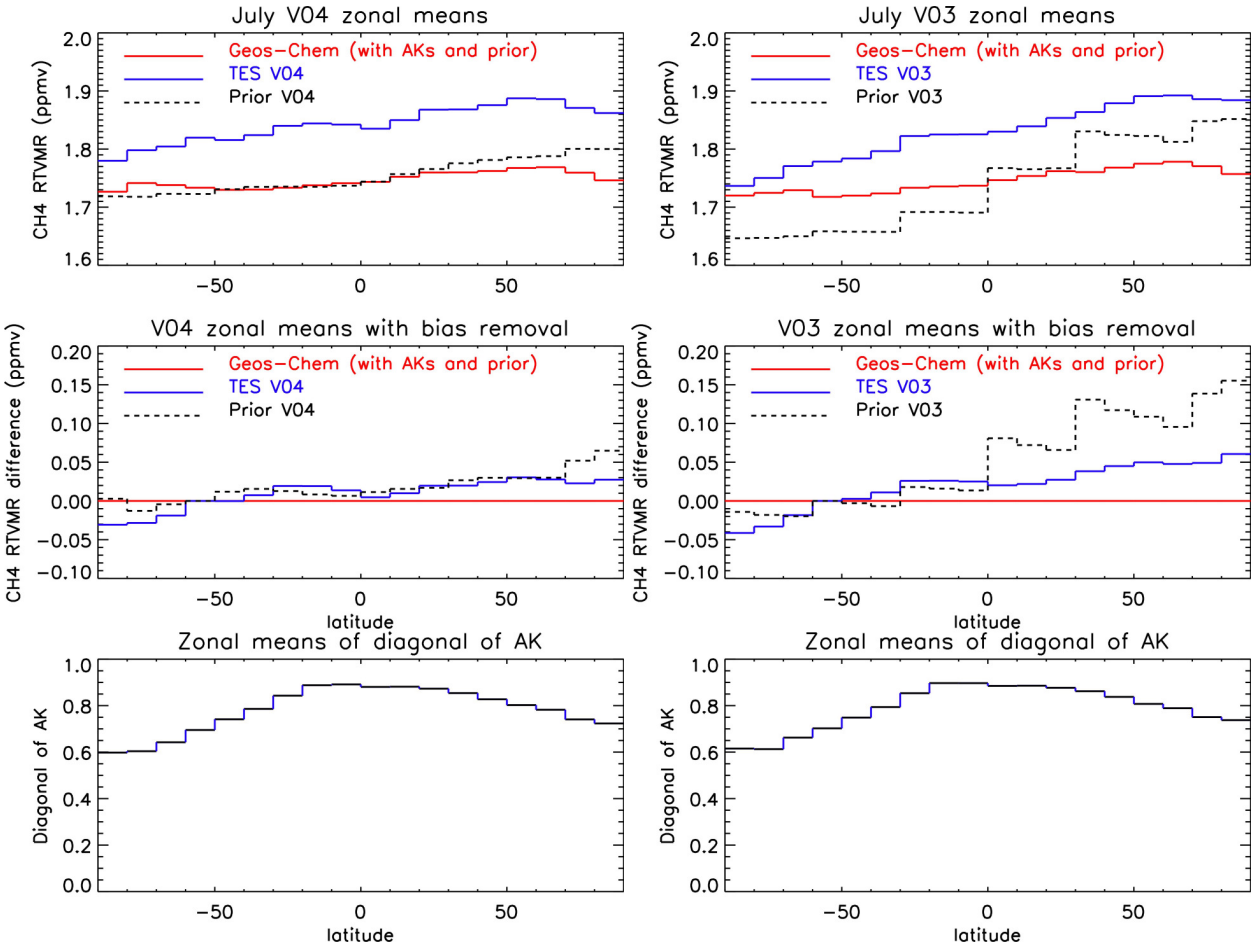

Figure 11-3 Top row: Zonal means of RTVMR for July 2005 calculated using 10 degree latitude bins from TES, GEOS-Chem with TES averaging kernels and a priori applied, GEOS-Chem without the TES a priori applied, and the TES prior. Middle row: Differences of zonal means from GEOS-Chem, with bias removal based on the zonal means at 50-60S. Bottom row: zonal means of the diagonal element of the transformed averaging kernel in RTVMR space, showing sensitivity of the RTVMR to the measurement (as opposed to the a priori.) Left panels show results for the TES V004 data, while right panels show results for the TES V003 data.

11.5 TES/FTIR comparisons

Preliminary comparisons have also been performed against data from a global network of ground-based FTIR instruments maintained by the Network for the Detection of Atmospheric Composition Change (NDACC). Work to date has involved comparisons between column amounts from TES and the FTIRs. However, the column values from TES are not the best representation of the instrument's capabilities, since TES has only limited sensitivity to methane close to the surface. Future work will involve validation against FTIR profile measurements through collaboration with FTIR instrument teams.

11.6 Comparison of V004 with V003 retrievals

In general, V004 methane RTVMRs are higher than V003 RTVMRs by around 1 to 1.5 %, Spatial distribution of the differences between GEOS-Chem and TES V003 and V004 is broadly similar on a global scale, but differences do vary somewhat with location and season. Possible reasons for differences include updates to the temperature and water vapor retrievals (see Sections 7 and 9 of this report) and an update in the V004 a priori constraint vector. V003 a priori profiles consisted of only five latitude bands, resulting in sharp transitions in tropospheric values at the boundaries and an unrealistic representation of the tropopause height (in terms of methane profile) over large regions of the globe. The V004 methane a priori has more gradual changes with latitude. Figure 11-3 shows zonal mean RTVMRs for V004 and V003 for one month of TES data alongside those for GEOS-Chem, showing the change in the a priori, the change in absolute RTVMR values and the similarity in the inferred latitudinal gradients between the two TES data versions. The interplay between the effect of the a priori update and the changes to the temperature and water vapor retrievals has not yet been investigated in detail.

11.7 Comments or limits on utility of the data

Since TES methane retrievals contain less than two DOFS, they do not contain meaningful information on the profile shape. Therefore, it is not recommended to view the data in terms of profiles or individual pressure levels. The RTVMR representation has been shown to be valuable in the analysis of the TES methane dataset. Further details on calculating RTVMRs may be found in the TES Level 2 Data Users Guide (Osterman et al., 2009) and in Payne et al. (2009).

The information content of TES methane measurements is limited over extremely cold regions, especially in the Southern Polar winter. Caution should be exercised in the interpretation of data from such regions. One possible additional quality check would be to consider as suspect any methane measurements where the sum of the row of the averaging kernel remains below 0.7 for all reported pressure levels.

11.8 Executive Summary

Validation of the TES methane product is ongoing. Work so far indicates that the TES methane product does contain useful information, when viewed in an appropriate representation. The use of "representative tropospheric volume mixing ratios" (RTVMRs) has been shown to be

valuable. TES V004 methane shows a 3.7 % mean high bias (4.4 % rms difference) with respect to DACOM in-situ aircraft measurements and a 6 % high bias with respect to AIRS v5.0 for comparisons of INTEX-B campaign measurements. TES V004 methane shows a 5 % high bias with respect to GEOS-Chem global monthly mean fields. Latitudinal gradients in TES methane are similar to those in GEOS-Chem, although TES latitudinal gradients are slightly stronger during northern hemisphere summer months.

11.9 References

11.9.1 TES Methane References

[1] Payne, V. H., S. A. Clough, M. W. Shephard, R. Nassar and J. A. Logan (2009), Information-centered representation of retrievals with limited degrees of freedom for signal: Application to methane from the Tropospheric Emission Spectrometer, *J. Geophys. Res., 114*, (doi:10:1029/2008JD010155) May 27, 2009.

11.9.2 TES References

[2] Bowman K. W., C. D. Rodgers, S. S. Kulawik, J. Worden, E. Sarkissian, G. Osterman, T. Steck, M. Lou, A. Eldering, M. Shephard, H. Worden, M. Lampel, S. A. Clough, P. D. Brown, C. P. Rinsland, M. Gunson, and R. Beer (2006), Tropospheric emission spectrometer: Retrieval method and error analysis, *IEEE Transactions on Geoscience and Remote Sensing, 44(5)*, 1297-1307, May 2006.

[3] Clough, S. A., M. W. Shephard, J. Worden, P. D. Brown, H. M. Worden, M. Lou, C. D. Rodgers, C. P. Rinsland, A. Goldman, L. Brown, S. S. Kulawik, A. Eldering, M. Lampel, G. Osterman, R. Beer, K. Bowman, K. E. Cady-Pereira, and E. J. Mlawer (2006), Forward Model and Jacobians for Tropospheric Emission Spectrometer Retrievals, *IEEE Transactions on Geoscience and Remote Sensing, 44 (No.5),* Special Issue on Aura, 1308–1323, May 2006.

[4] Osterman, G., (editor), K. Bowman, A. Eldering, B. Fisher, R. Herman, D. Jacob, L. Jourdain, S. Kulawik, M. Luo, R. Monarrez, G. Osterman, S. Paradise, V. Payne, S. Poosti, N. Richards, D. Rider, D. Shepard, M. Shephard, F. Vilnrotter, H. Worden, J. Worden, H. Yun and L. Zhang (2009), Earth Observing System (EOS) Tropospheric Emission Spectrometer (TES) Level 2 (L2) Data User's Guide (Up to & including Version 4 data), Version 4.0, JPL Internal Report D-38042, May 20, 2009.

11.9.3 General References

[5] Dlugokencky, E.J., P.M. Lang, and K.A. Masarie (2007), Atmospheric Methane Dry Air Mole Fractions from the NOAA ESRL Carbon Cycle Cooperative Global Air Sampling Network, 1983-2006, Version: 2007-09-19, Path: ftp://ftp.cmdl.noaa.gov/ccg/ch4/flask/event/

[6] Strow L. L., S. E. Hannon, S. De-Souza Machado, H. E. Motteler, D. C. Tobin (2006), Validation of the Atmospheric Infrared Sounder radiative transfer algorithm, *J. Geophys. Res. Atmospheres, 111*, D09S06, (doi:10.1029/2005JD006146) May 13, 2006.

[7] Susskind, J., C. D. Barnet and J. M. Blaisdell (2003), Retrieval of atmospheric and surface parameters from AIRS/AMSU/HSB data in the presence of clouds, *IEEE Transactions on Geoscience and Remote Sensing, 41 (2),* 390-409, February 2003.

[8] Wang, J. S., J. A. Logan, M. B. McElroy, B. N. Duncan, I.A. Megretskaia and R. M. Yantosca (2004), A 3-D model analysis of the slowdown and interannual variability in the methane growth rate from 1988 to 1997, *Global Biogeochem. Cycles, 18*, (doi10.1029/2003GB002180) August 21, 2004.

[9] Xiao, Y., D. J. Jacob, J. S. Wang, J. A. Logan, P. I. Palmer, P. Suntharalingam, R. M. Yantosca, G. W. Sachse, D. R. Blake and D. G. Streets (2004), Constraints on Asian and European sources of methane from CH_4-C_2H_6-CO correlations in Asian outflow, *J. Geophys. Res., 109,* D15S16, (doi:10.1029/2003JD004475) August 10, 2004.

[10] Xiong, X., C. Barnet, E. Maddy, C. Sweeney, X. Liu, L. Zhou and M. Goldberg (2008), Characterization and validation of methane products from the Atmospheric Infrared Sounder (AIRS), *J. Geopys. Res., 113*, G00A01, (doi:10.1029/2007JG000500) July 4, 2008.

12. Cloud Products

TES performs a retrieval of frequency dependent effective optical depth and cloud top pressure along with the trace gas retrievals. There are a number of fields the user might be interested in:

- CloudTopPressure,
- CloudTopPressureError,
- CloudEffectiveOpticalDepth (has frequency dependence),
- CloudEffectiveOpticalDepthError (has frequency dependence), and
- AverageCloudEffOpticalDepth.

12.1 Background

TES retrieves a cloud top pressure and cloud effective optical depth for each measurement. These data have error estimates, and based on those estimates and physics principles, we can make some statements about when TES has sensitivity to cloud parameters and when we do not. Figure 12-1 contains 2-D histograms of the cloud top pressure and effective cloud optical depth at 975 cm^{-1} for V003 and V004 of TES data. Figure 12-2 is a scatter plot of the cloud top pressure and effective cloud optical depth at 975 cm^{-1} from the V004 data. The error estimates are plotted over the data. These show that there is small uncertainty for moderate optical depths (1-10) and higher level clouds (pressures from 200-800 hPa). Error estimates on both effective optical depth and cloud top pressure tend to be large for clouds with optical depths less than a few tenths. For high effective optical depth clouds (greater than 10) at pressures between 800 and 1000 hPa), error estimates for cloud top pressure grow a bit larger again.

These error estimates are consistent with our expectations for TES – due to low thermal contrast, clouds near the surface are harder to characterize than clouds at high altitudes. Also, small effective optical depth clouds impart a small radiance change, and are harder to characterize than moderate optical depths. By time the effective cloud optical depth becomes larger than a few, the radiance change with change in optical depth is small, and characterization becomes more difficult.

12.2 Changes from TES V003 to V004

There was one significant change to the TES retrieval algorithm in V004. This was the separation of the retrievals of water, ozone and temperature into separate steps in software. This results in spreading out the occurrence of retrievals at lower optical depths. There is also greater spread in altitude in the V004 retrievals. These changes are seen in the two panels of Figure 12-1.

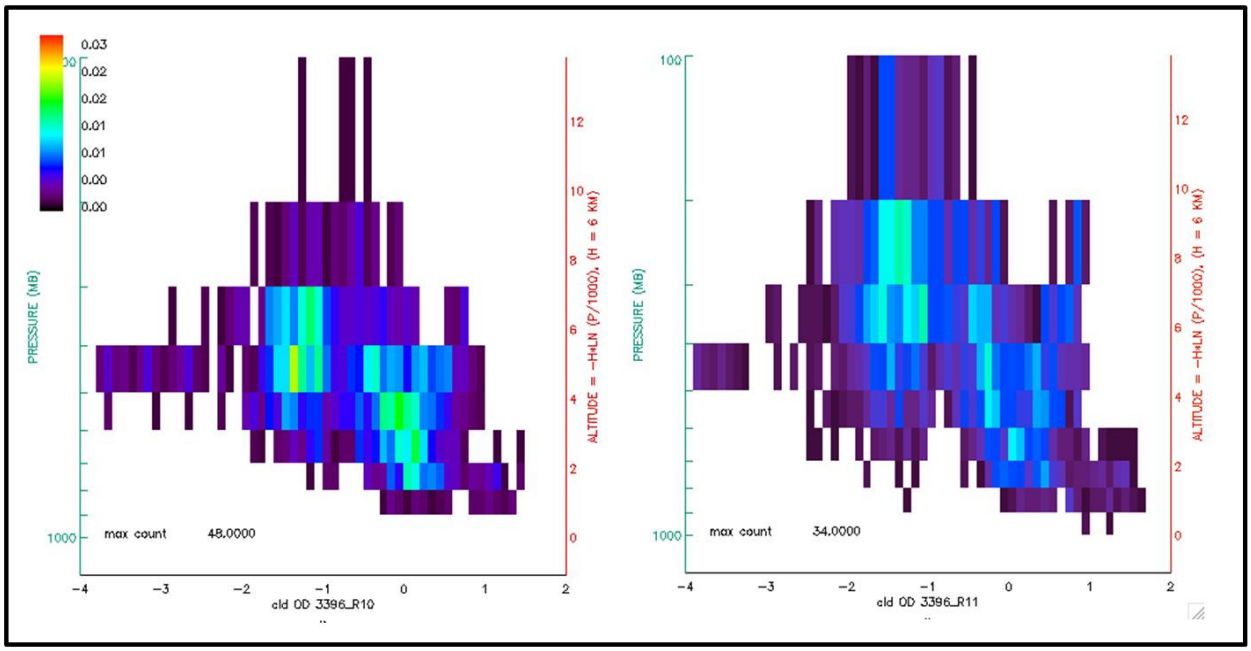

Figure 12-1 2-D histogram of TES retrieved cloud top pressure and cloud effective optical depth at 975 cm^{-1} for Global Survey run ID 3396. The left panel shows the results for V003 and the right panel for V004. The color bar indicates the frequency of occurrence in fraction.

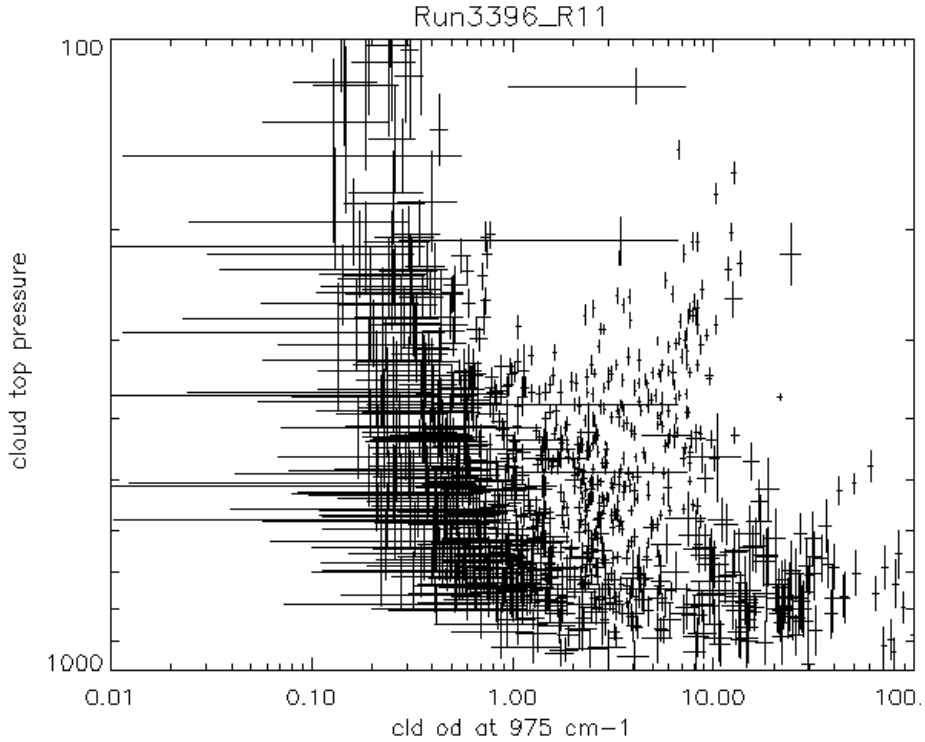

Figure 12-2 TES retrieved cloud top pressure and cloud effective optical depth at 975 cm^{-1} with error estimates for runid 3396.

12.3 Cloud Top Pressure

The cloud top pressure has been compared to MODIS and AIRS cloud top pressures. Only MODIS comparisons are presented in this version of the validation document. For this comparison we use the MODIS cloud top pressure that is determined from the infrared retrieval technique from the MYD06 products. TES data are paired with the nearest neighbor of the MODIS 5km by 5km data products. There is always significant overlap of the TES and MODIS footprints. We select only the MODIS data that is confidently cloudy (cloud mask value 0). Figure 12-3 shows a histogram of the TES – MODIS cloud top pressure differences in hPa for the complete set of clouds. The mean was reduced to 0.0 hPa in V003, from 48 hPa in V002, but we still see that there are outliers with differences of greater than 300 hPa. In V004, there are now more retrievals with a difference between 100 and 200 hPa, with a large increase near 150 hPa. The data shown in Figure 12-3 are from a TES Global Survey, similar statistics are seen in analyses of special observations.

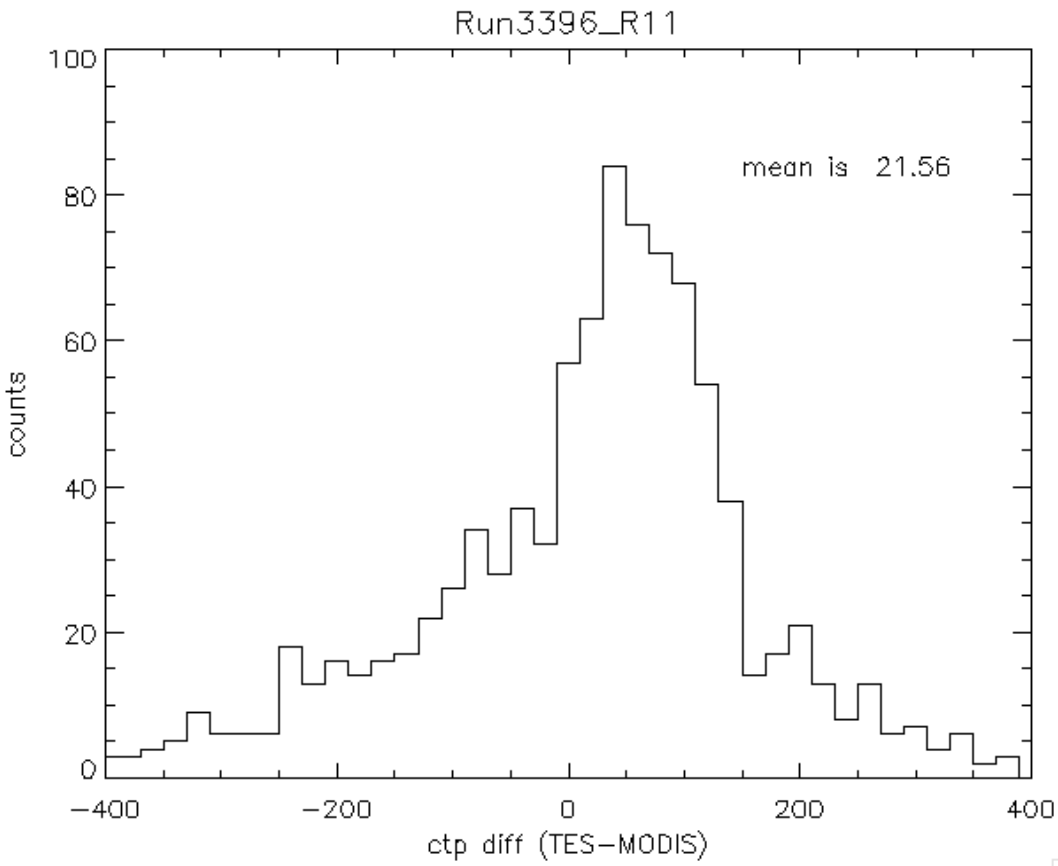

Figure 12-3 Histogram of Cloud Top Pressure Differences between MODIS and TES in hPa.

To look into the cloud top pressure differences in a little more detail, statistics were developed after grouping data by cloud top pressure and cloud optical depth. The left hand column of Figure 12-4 shows data with effective optical depths less than 3, while the right hand column is all effective optical depths greater than OD 3.The lower panels are cloud top pressures greater than 700 hPa, while the upper panels are cloud top pressure less than 350 hPa. We see that the histograms of cloud top pressure differences for clouds above 350 hPa are narrower. The lower optical depth clouds below 350 hPa have broad histograms although the mean differences are

small. Further analysis shows that the large differences are related to the fact that TES's default initial guess for cloud top pressure is 500 hPa, while the MODIS first guess is closer to the surface pressure. The histograms in Figure 12-4 also illustrate that the increase in retrievals of cloud top pressure with differences from MODIS between 100 and 200 hPa are seen across a wide variety of cloud top pressures and optical depths.

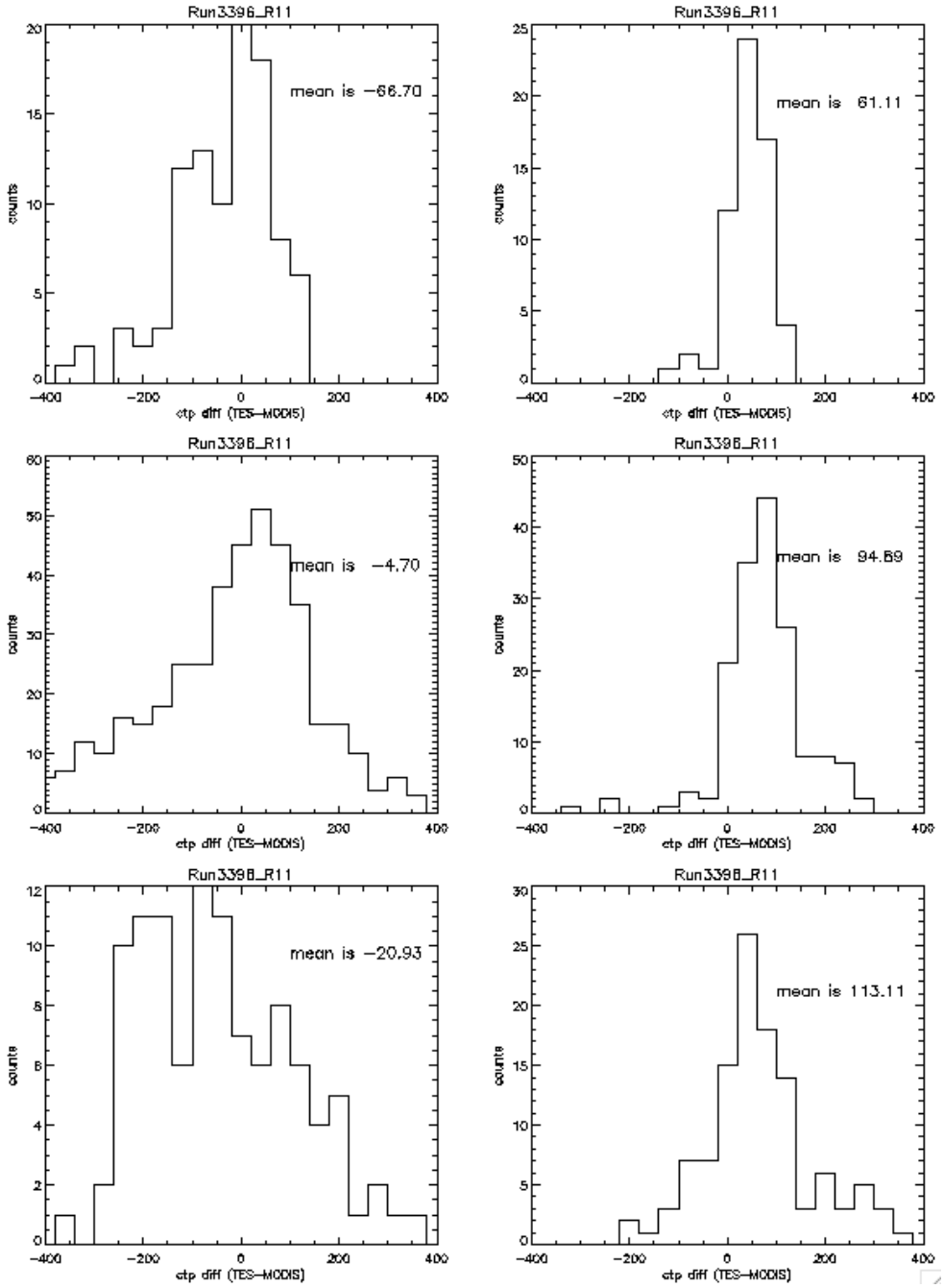

Figure 12-4 Histogram of TES-MODIS cloud top pressure differences for V004 TES data. Left column is data with an effective optical depth less than 3, right hand column is for optical depths greater than 3. Upper row is cloud top pressure less than 350 hPa, bottom row is cloud top pressure greater than 700 hPa.

Figure 12-5 illustrates the changes between V003 and V004 for the high and thinner clouds. The histogram of cloud top pressure is not as sharply peaked for V004. We believe the separation of the water vapor and temperature retrieval steps has impacted the cloud characterization.

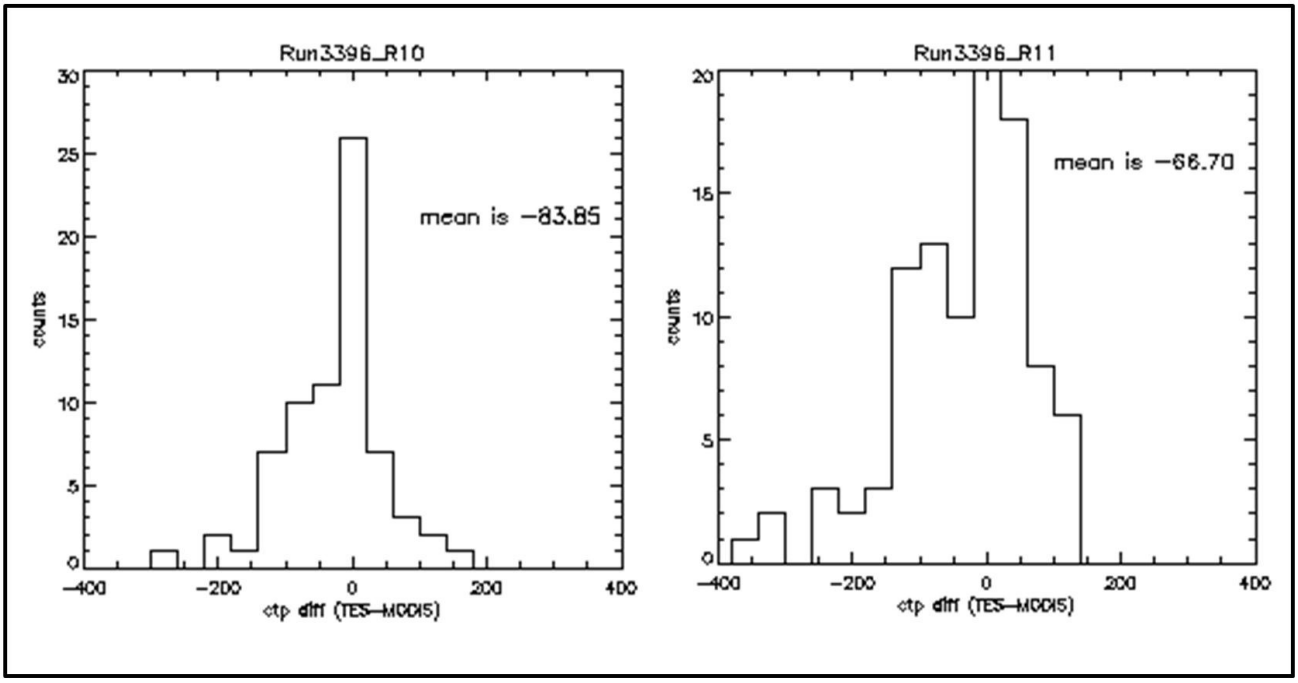

Figure 12-5 Comparison of histograms of cloud top pressure differences (TES-MODIS) for clouds with effective optical depth less than 3 and cloud top pressure less than 350 hPa for V002 (left panel) and V003 (right panel). The histogram for V003 is much more sharply peaked.

12.4 Cloud Effective Optical Depth

At present, we have limited correlative datasets for the validation of the effective cloud optical depth product from TES. For characterization purposes, we have compared MODIS visible optical depths to the TES effective cloud optical depths retrieved at 975 cm^{-1}. The average effective cloud optical depth is very well correlated to the effective cloud optical depth at 975 cm^{-1}, except at small effective optical depth, as shown in previous validation reports.

A scatter plot of TES effective cloud optical depth at 975 cm^{-1} and MODIS cloud optical depth is presented in Figure 12-6. The expected ratio of visible to infrared optical depth is dependent on the cloud particle sizes and shapes, and is thought to be on the order of 2. Figure 12-6 shows clearly that MODIS optical depths are larger than those from TES, but the scaling ranges from a factor of 10 to 1.

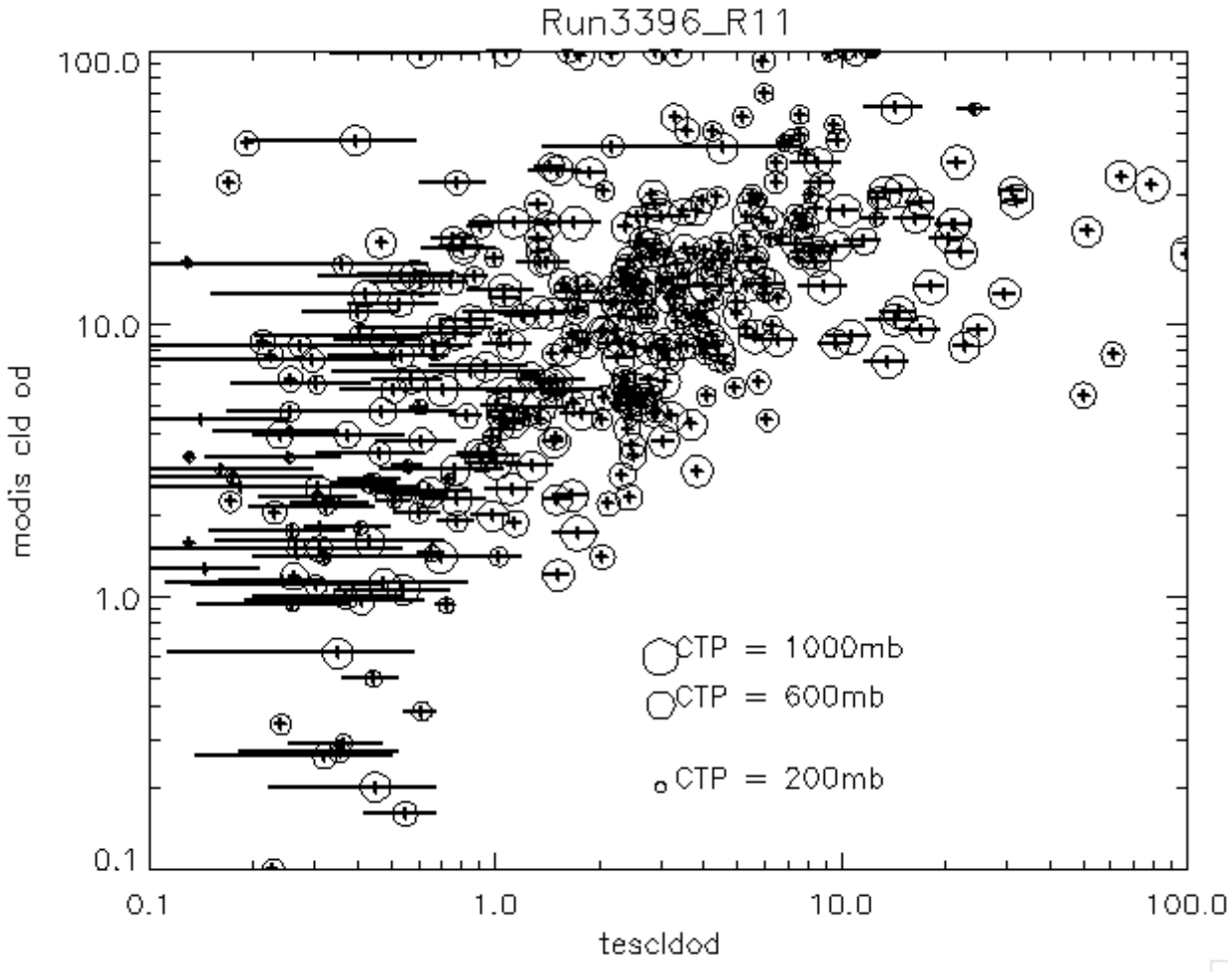

Figure 12-6 Scatterplot of MODIS visible cloud optical depth and TES effective cloud optical depth at 975 cm^{-1}.

Appendices

A. Acronyms

ACE	Atmospheric Chemistry Experiment
AIRS	Atmospheric Infrared Sounder
ALIAS	Aircraft Laser Infrared Absorption Spectrometer
AMSU	Advanced Microwave Sounding Unit
ASDC	Atmospheric Science Data Center
ARCIONS	Arctic Intensive Ozonesonde Network Study
ARCTAS	Arctic Research on the Composition of the Troposphere from Aircraft and Satellites
ARM	Atmospheric Radiation Measurement
ARM-SGP	Atmospheric Radiation Measurement – Southern Great Plains
AVE	Aura Validation Experiment
CFH	Cryogenic Frostpoint Hygrometer
CH_4	Methane, Natural Gas
CO	Carbon Monoxide
CO_2	Carbon Dioxide
CR-AVE	Costa Rica Aura Validation Experiment
CTM	Chemical Transport Model
DACOM	Differential-Absorption Carbon Monoxide Monitor
DOE	Department of Energy
DOF	Degrees of Freedom
DOFS	Degrees of Freedom for Signal
DPS	Data Products Specification
EOS	Earth Observing System
ESDT	Earth Science Data Type
ESRL	Earth System Research Laboratory
FTIR	Fourier Transform Infrared Spectrometer
FTP	File Transfer Protocol
FTS	Fourier Transform Spectrometer
GMD-ESRL	Global Monitoring Division of the Earth System Research Laboratory

GEOS	Global Earth Observing System
GEOS	Goddard Earth Observing System
GMAO	Global Modeling Assimilation Office
GSFC	Goddard Space Flight Center
GTS	Global Telecommunications Service
H_2O	Dihydrogen Monoxide (Water)
HDF	Hierarchical Data Format
HDO	Hydrogen Deuterium Monoxide ("Heavy Water")
HIRDLS	High Resolution Dynamics Limb Sounder
HIRS	High Resolution Infrared Sounders
HIS	High-Resolution Interferometer Sounder
HITRAN	HIgh-resolution TRANsmission molecular absorption database
hPa	Hectopascal, a unit used for air pressure
HYSPLIT	Hybrid Single-Particle Lagrangian Integrated Trajectory
IDL	Interactive Data Language
IEEE	Institute of Electrical and Electronics Engineers
IGRA	Integrated Global Radiosonde Archive
INTEX	International Chemical Transport Experiment
IONS	INTEX Ozonesonde Network Study
ISM	Integrated Spectral Magnitude
JPL	Jet Propulsion Laboratory
K	Kelvin
L1B	Level 1B
L2	Level 2
LBLRTM	Line-by-Line Radiative Transfer Model
LT	Lower Troposphere
MATCH	Model of Atmospheric Transport and Chemistry
MISR	Multi-angle Imaging SpectroRadiometer
MLS	Microwave Limb Sounder
MODIS	Moderate Resolution Imaging Spectroradiometer
MOHAVE	Measurements of Humidity in the Atmosphere Validation Experiments
MOPITT	Measurement Of Pollution In The Troposphere

MOZAIC	Measurement of OZONE on Airbus In-service Aircraft
MOZART	Model for OZone And Related chemical Tracers
NASA	National Aeronautics and Space Administration
NCEP	National Centers for Environmental Prediction
NDACC	Network for the Detection of Atmospheric Composition Change
NH	New Hampshire
NOAA	National Oceanic & Atmospheric Administration
O_3	Ozone
OD	Optical Depth
OMI	Ozone Monitoring Instrument
PAVE	Polar Aura Validation Experiment
PI	Principal Investigator
rms	Root-Mean-Square
ROI	Reynolds Optimally Interpolated
RTVMR	Representative Tropospheric Volume Mixing Ratio
Run ID	TES run identification number
SCIAMACHY	Scanning Imaging Absorption Spectrometer for Atmospheric Cartography
SHADOZ	Southern Hemisphere Additional Ozonesondes
SST	Sea Surface Temperature
TATM	Temperature
TES	Tropospheric Emission Spectrometer
TOPP	Tropospheric Ozone Pollution Project
TSUR	Surface Temperature
UT	Upper Troposphere
UTC	Universal Time Coordinated
VMR	Volume Mixing Ratio
WAVES	Water Vapor Validation Experiments
WOUDC	World Ozone and Ultraviolet Radiation Data Centre